Stanford Photonics Research Center

2008 Annual Symposium: Global Impact of Photonics
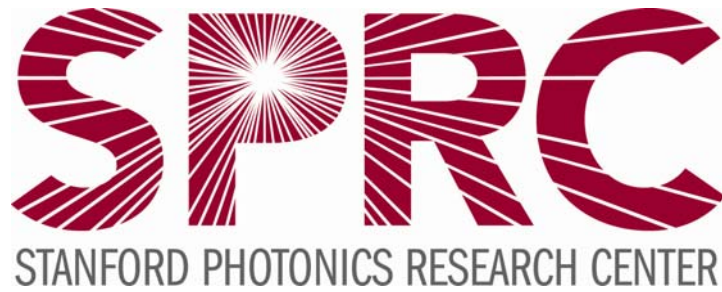
2008 Proceedings & Annual Report

SPRC

STANFORD PHOTONICS RESEARCH CENTER

http://photonics.stanford.edu

STANFORD
UNIVERSITY

Stanford Photonics Research Center

2008 Proceedings and Annual Report

September 15th-17th, 2008
Hewlett Auditorium
Stanford University
Stanford, CA

STANFORD UNIVERSITY

http://photonics.stanford.edu

Executive Summary

The eighth Annual Symposium of the Stanford Photonics Research Center (SPRC) will be held September 15 to September 17 in the Hewlett Teaching Center on the Stanford University campus. The SPRC Symposium will feature invited talks on a wide range of photonics research topics presented by leading researchers from around the world. In addition, several SPRC faculty and student members will present the latest results from their research efforts. The Symposium will begin with opening remarks by the Executive Director of SPRC Dr. Thomas M. Baer at 8:00 AM on Monday, September 15.

The symposium will consist of 10 sessions:

1. Quantum and Science Technology
2. Optics in the Automotive Industry
3. The Global Impact of Photonics
4. Nanomaterials for Solar Energy
5. Optical Imaging and Control in Biology
6. High Capacity Optical Communication Networks
7. Optical Interconnects
8. Advanced Laser and Nonlinear Devices
9. Ultrafast Physics and X-Ray Science
10. Nanophotonics

In addition, poster sessions are scheduled for each day of the conference. On Monday afternoon industry thought leaders and scientists will present a series of overviews of a wide variety of industries where the latest photonics technologies are having a major impact on the way we live. These areas include: solar energy, LED lighting, automotive photonics, biophotonics, and integrated photonics. The speakers will describe current commercial markets, the potential impact as these technologies mature and improve, and the technical challenges hindering further penetration. In addition, a special plenary talk will be given on Wednesday morning by Dr. Jun Ye from JILA, entitled "Optical Clocks and Applications".

On Monday evening, September 15, a conference reception will be held at the Stanford Faculty Club at 5:45pm followed by dinner for those who have made reservations. The featured after-dinner speaker is Dr. Jerry Nelson from the University of California, Lick Observatory, who will speak on TMT: Designing and Building the World's Largest Telescope.

The program will close with remarks by SPRC Executive Director Tom Baer at 5:30pm on Wednesday, September 17.

We are fortunate again this year to have industry sponsors lend their support to the Annual Symposium. SPRC wishes to thank Agilent Technologies, CVI/Melles Griot, Photonics Spectra, Newport / Spectra-Physics, and SPIE for their generous contributions. Please take time during the SPRC Symposium to meet with sponsor representatives and visit their tabletop displays.

We also want to thank our Affiliate Member companies for their ongoing and generous support of photonics research at Stanford: Agilent Technologies, Collinear Corp., Corning, Electro-Scientific Industries, Enablence, Hamamatsu, Innovation Core SEI, Lockheed Martin/Coherent, MegaOpto, Nitto Denko, Northrop Grumman, NTT Photonics, OptiMedica, PEAK Surgical, Raytheon, RICOH, Sony Corp., and Varian Semiconductors.

The Stanford Photonics Research Center

The Stanford Photonics Research Center is an Industrial Affiliates Program that builds strategic partnerships between the Stanford University photonics research community and industry companies and organizations in research areas including photonics, optics, fundamental science and related fields. SPRC is a critical element of the teaching and research programs at Stanford. SPRC promotes interaction between Stanford and the community, often leading to joint research and the development of new directions in photonics research. SPRC promotes such interaction and facilitated access by our affiliates to photonics research on campus, benefiting our partners as well as our advanced degree students. We encourage you to become a member of SPRC to support and benefit from research and teaching in all aspects of photonics at Stanford.

Thank you for joining us at the 2008 SPRC Annual Symposium.

Robert L. Byer
Martin M. Fejer
David A. B. Miller
SPRC Co-Directors

Dr. Tom Baer
SPRC Executive Director
Sara Charbonneau-Lefort
Assistant Director

Stanford Photonics Research Center
ph: 650-723-5627
fax: 650-725-1822
http://photonics.stanford.edu

About SPRC

The Stanford Photonics Research Center (SPRC) builds strategic partnerships between the Stanford University photonics research community and corporations and other organizations active in photonics or employing lasers and optical technologies in their research and product development activities, Member companies gain facilitated access to Stanford faculty, students and researchers by participating in SPRC events, supporting and collaborating on specific research projects, mentoring students, and visiting research labs. Member benefits also include priority alerting for Stanford photonics invention disclosures. SPRC promotes member company recruitment of Stanford students, and facilitates research interactions with Stanford PhD students, faculty, and other researchers. In turn, Stanford students establish connections with scientific experts and business leaders in the photonics industry that continue beyond their Stanford experience.

SPRC faculty and student members belong to one or more working groups which are best aligned with their research interests. These working groups cover a wide range of research areas and technologies, including:

Solar Cell Technologies	Quantum Information Science
Information Technology	Nanophotonics
Telecommunications	Photonic sensors
Neuroscience	Medical Diagnostics
Microscopy and Molecular Imaging	Aerospace
High power laser sources	Automotive
Ophthalmology	Entrepreneurship
Consumer Photonics and Electronics	

SPRC corporate members interact directly with faculty working groups conducting research in areas most directly related to company interests.

Membership

Membership in the Stanford Photonics Research Center is available to companies interested in establishing mutually-beneficial relationships with the Stanford photonics community. Membership fees directly support research and teaching in photonics at Stanford; in turn, members gain facilitated access to Stanford photonics students, faculty, and current and emerging areas of research at Stanford.

There are four levels of membership in SPRC:

Founding Membership
Founding Members help set the strategic direction of SPRC and may participate on the SPRC Advisory Board. Founding Membership involves a multi-year commitment to membership dues at the Senior Member level (see below) plus a capital donation of $2M. Founding Members receive all benefits of other membership levels.

Senior Membership
In addition to the benefits listed below for all membership levels, Senior Members may participate on the SPRC Advisory Board, may send a scholar/researcher to Stanford for up to six months per year to work with a collaborating Stanford faculty member and research group. Senior members may also support multiple Stanford photonics research groups in accordance with SPRC Advisory Board and University policy.
The annual fee for Senior Membership is $150,000.

Standard Membership
In addition to the benefits listed below for all membership levels, Standard Membership offers companies the opportunity to send a visiting scholar/researcher to Stanford for up to one month per year to work with a collaborating Stanford faculty member and research group. Regular members may also support a Stanford photonics Working roup in accordance with SPRC Advisory Board and University policy.
The annual fee for Standard Membership is $50,000.

Start-up Members
The Start-up Membership level is for companies and organizations that wish to join SPRC but do not wish to financially support a specific faculty or research group. The membership fee will go to support SPRC events and outreach activities.
The annual fee for Start-up Membership is $25,000.

Basic Benefits for all Members
In addition to the specific benefits stated above for each membership level, all member companies receive the following basic benefits:

- Facilitated access to Stanford photonics research activities and results
- Prompt alerting for Stanford invention disclosures in photonics
- Customized courses delivered via Web or in-person by Stanford photonics faculty
- Facilitated access to Stanford's photonics intellectual property portfolio
- Discounted Symposium registration fee and complimentary registration to workshops
- Priority notification of, and invitations to, all SPRC events
- Access to photonics students' resumes for recruitment
- Electronic and/or CD-ROM versions of all SPRC event publications and proceedings

SPRC Events

SPRC has developed a program of events to facilitate interaction between Member Companies and the Stanford photonics community:

Focused Workshops: faculty working groups organize one day workshops on topics related to current trends in photonics research and industry. Previous topics include Organic Photonics, Nanophotonics, Biophotonics, and Optical Interconnects. Workshops are usually held on the Stanford campus.

Company Focus Days: Member company representatives visit Stanford for customized meetings with faculty working groups and student researchers. These half-day or full-day meetings include research presentations and tours of photonics labs, and may also include a recruitment-focused lunch with photonics students.

Member Company Recruitment Mixer: Current research is presented by students in a poster session, followed by an informal reception. Member company representatives can meet one-on-one with students for recruiting purposes.

SPRC Symposium *(September)*: This 3-day symposium provides an overview of state-of-the-art in photonics research and business. Features invited speakers from Stanford, the international research community, and the photonics business world. Open to the public; SPRC members receive registration discount.

Monday, September 15

7:30 – 8:30	Check-in / On-site Registration / Continental Breakfast
8:30 – 8:45	Welcome Remarks

Session 1: Quantum Science and Technology I

8:45 – 9:15	**Modulation of Single Photons and Biphotons** Steve Harris, Stanford University
9:15 – 9:30	**Single Photon Nonlinear Optics with Quantum Dots in Photonic Crystal Resonators** Andrei Faraon, Stanford University
9:30 – 10:00	**Quantum Information Processing with Trapped Ions** Dietrich Leibfried, NIST Boulder

Coffee Break
10:00 – 10:30

Session 2: Quantum Science and Technology II

10:30 – 11:00	**Quantum Nonlinear Dynamics** Hideo Mabuchi, Stanford University
11:00 – 11:15	**Low Level Models for Quantum Error Correction** Joseph Kerckhoff, Stanford University
11:15 – 11:45	**Quantum Measurement with Superconducting Circuits** Irfan Siddiqi, UC Berkeley

Lunch and Poster Session
11:45 – 2:00

Session 3: Global Impact of Photonics

2:00 – 2:15	Waguih Ishak, Corning
2:15 – 2:30	Sven Strohband, MDV
2:30 – 2:45	Werner Götz, Philips LED
2:45 – 3:00	John Giddings, Clean Tech Integration
3:00 – 3:15	Steve Turner, Pacific Biosciences

Coffee Break
3:15 – 3:45

Global Impact of Photonics Panel Discussion

3:45 – 4:45	Panel Discussion
4:45 – 5:00	Closing Remarks

5:30	Reception @ Stanford Faculty Club, Courtyard
6:30	Dinner @ Stanford Faculty Club, Main Dining Hall
7:30	**TMT: Designing and Building the World's Largest Telescope** Jerry Nelson

2008 Annual Symposium: Global Impact of Photonics

<u>**Tuesday, September 16**</u>

8:00 – 9:00   Registration / Breakfast

Session 1: Optics in the Automobile Industry
9:00 – 9:30   **Road Modeling Using Photonics in Autonomous Driving**
Wende Zhang, GM
9:30 – 10:00   **Photonics Applications in Driver Assistance Systems**
Arne Stoschek, Volkswagon

Coffee Break
10:00 – 10:30

Session 2: Optical Imaging and Control in Biology
10:30 – 11:00   **Optical Control of Brain Function**
Karl Deisseroth, Stanford University
11:00 – 11:15   **Advanced Imaging Techniques for Biology**
Na Ji, Janelia Farm, HHMI
11:15 – 11:45   **Photoacoustic Tomography**
Sam Gambhir, Stanford University
11:45 – 12:00   **High-speed SHG Imaging of Muscle Contractility in Mice and Humans**
Mike Llewellyn, Stanford University

Lunch & Poster Session
12:00 – 2:00

Session 3: High Capacity Optical Communication Networks
2:00 – 2:10   **Overview**
Joseph M. Kahn, Stanford University
2:10 – 2:40   **Next-Generation WDM Transport Enabling Zettabyte IP Network Evolution**
Loukas Paraschis, Cisco Systems
2:40 – 3:10   **DSP Enabled 40 Gb/s and 100 Gb/s Transmission for Optical Mesh Networks**
Maurice O'Sullivan, Nortel Networks
3:10 – 3:30   **Compensating for Fiber Nonlinearity Using Digital Backpropagation**
Ezra Ip, Stanford University

Coffee Break
3:30 – 4:00

Session 4: Optical Interconnects
4:00 – 4:30   **Optical Interconnects in Supercomputers and High Performance Servers**
Jeff Kash, IBM Research
4:30 – 4:45   **Nanoscale Photodetectors Enhanced by Optical Antennas**
Salman Latif, Stanford University
4:45 – 5:15   **Applications of Nanophotonics to Classical and Quantum Information Technology**
Ray Beausoleil, HP

5:15 – 5:30   Closing Remarks

6:00   BBQ

2008 Annual Symposium: Global Impact of Photonics

SPRC — STANFORD PHOTONICS RESEARCH CENTER

Wednesday, September 17

8:00 – 8:30	Registration / Breakfast

8:30 – 9:15   **Optical Clocks and Applications**
Jun Ye, JILA/Univ of Colorado

Session 1: Advanced Laser and Nonlinear Devices

9:15 – 9:45   **Two Micron Fiber Laser**
Peter Moulton, Q Peak, Inc.
9:45 – 10:00   **Power Scaling of Phosphate Glass Fiber Laser**
Yin Wen Lee, Stanford University
10:00 – 10:15   **Slow Light for Sensitive Detectors**
Matt Terrel, Stanford University
10:15 – 10:30   **Advanced Laser Concepts**
Bill Krupke, WFK Lasers LLC

Coffee Break
10:30 – 11:00

Session 2: Ultrafast Physics & X-Ray Science

11:00 – 11:30   **Femtosecond X-ray Studies of Materials**
Aaron M. Lindenberg, Stanford University, SLAC
11:30 – 11:45   **Dielectric Undulator for Coherent X-ray Generation**
Tomas Plettner, Stanford University
11:45 – 12:15   **High Harmonic Generation from Multiple Orbitals**
Markus Guehr, Stanford University, SLAC

Lunch & Poster Session
12:15 – 2:00

Session 3: Nonlinear Optics and Applications

2:00 – 2:30   **Non-linear Optics Enabling Laser Display Applications**
Greg Niven, Arasor
2:30 – 3:00   **Real-Time Chemical Sensors Based on Novel NLO Laser Systems**
Jim Scherer, NovaWave
3:00 – 3:15   **Self-phase-locked Degenerate Synchronously Pumped Optical Parametric Oscillator**
Samuel Wong, Stanford University

Coffee Break
3:15 – 3:45

Session 4: Nanophotonics

3:45 – 4:15   **Nano-imaging with a Metallic Nanolens**
Satoshi Kawata, Osaka University
4:15 – 4:30   **Dielectric Optical Antenna Emitters**
Jon Schuller, Stanford University
4:30 – 5:00   **Metamaterials** *(tentative title)*
David Smith, Duke University
5:00 – 5:15   **One-Way Electromagetic Waveguides**
Zongfu Yu, Stanford University

5:15 – 5:30   Concluding Remarks
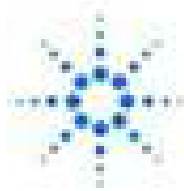
5:30   Afternoon Break, Ginzton Courtyard

SPRC
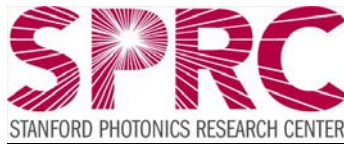
SPRC would like to thank our 2008 Symposium Sponsors

SPIE

Agilent Technologies

Worldwide Coverage: Optics, Lasers, Imaging, Fiber Optics, Electro-Optics, Photonic Component Manufacturing

PHOTONICS SPECTRA

CVI Melles Griot

Newport
Experience | Solutions

Spectra-Physics
A Division of Newport Corporation

SPRC
STANFORD PHOTONICS RESEARCH CENTER

Member Companies

SPRC THANKS OUR MEMBER COMPANIES FOR THEIR CONTINUED SUPPORT OF
PHOTONICS RESEARCH AT STANFORD UNIVERSITY

Agilent Technologies

COLLINEAR

CORNING

esi

Enablence Technologies Inc.

HAMAMATSU

INNOVATION CORE

MEGA OPTO

LOCKHEED MARTIN

NITTO DENKO

NORTHROP GRUMMAN

NTT

OptiMEDICA

PEAK surgical

Raytheon

RICOH

SONY

varian semiconductor equipment

SPRC Co-Directors

Thomas M. Baer
Executive Director
Biophotonics, medical diagnostic instrumentation, microscopy, laser source engineering, consumer applications of photonics, entrepreneurship

Robert L. Byer
Professor of Applied Physics
Solid state lasers, adaptive optics, nonlinear optics

Gary Bjorklund
Consulting Director
Telecommunications, information technology, solar energy, quantum information science

Martin M. Fejer
Professor of Applied Physics
Nonlinear and guided-wave optics, microstructured materials, optical signal processing, tunable and ultrafast sources

David A.B. Miller
Professor of Electrical Engineering, and, by courtesy, of Applied Physics
http://www.stanford.edu/people/dabm Optoelectronic and nanophotonic physics, devices and systems; optical switching and interconnects; optical sensing

Photonics Core Faculty/Senior Researchers
(http://stanfordphotonics.stanford.edu/research.faculty.php)

Zhenan Bao
Associate Professor of Chemical Engineering
Polymer and organic electronics and photonics

Stacey Bent
Professor of Chemical Engineering and, by courtesy, of Materials Science & Engineering and of Chemistry
Nanostructured materials, fuel cells, and inorganic solar cell fabrication

Steven Block
Professor of Applied Physics and Biological Sciences
Single-molecule biophysics, laser-based optical traps, biological motors

Mark L. Brongersma
Professor of Materials Science and Engineering
Photonic nanoparticles and nanostructures

Thomas Clandinin
Assistant Professor of Neurobiology
Medical genetics, biology

Chris Contag
Professor of Pediatrics
Pediatrics, neonatology, microscopy

Karl Deisseroth
Assistant Professor of Bioengineering and of Psychiatry and Behavioral Sciences
Neurobiology

Michel Digonnet
Senior Research Engineer, Ginzton Lab
Fiber optics

Abbas El Gamal
Professor of Electrical Engineering
Digital imaging and wireless networks

Shanhui Fan
Assistant Professor of Electrical Engineering
Photonic crystals, computational electromagnetics, optical communications

Michael Fayer
Professor of Chemistry
Dynamics and intermolecular interactions of molecules in liquids, and liquid crystals

Robert Feigelson
Professor of Materials Science and Engineering, Emeritus
Nonlinear optical materials

Ronald K. Hanson
Professor of Mechanical Engineering
Laser-based diagnostics and sensors, combustion and gas dynamics applications

James S. Harris
Professor of Engineering, Materials Science and, by courtesy, Applied Physics
Semiconductor optoelectronic materials, devices and applications, quantum information

Stephen Harris
Professor of Electrical Engineering & Applied Physics
Fundamentals of photonics and nonlinear optics

Lambertus Hesselink
Professor of Electrical Engineering and, by courtesy, of Applied Physics
Nanophotonics and ultra-high density optical data storage

Joseph M. Kahn
Professor of Electrical Engineering
Optical fiber communications, free-space optical communications, associated devices and subsystems

Mark Kasevich
Professor of Physics and Applied Physics
High accuracy navigation and gravimetric sensors based on de Broglie wave interferometry; Future atom optics sensors which exploit the novel coherence properties of Bose-Einstin condensates

Leonid Kazovsky
Professor of Electrical Engineering
Optical telecommunications and network systems

Thomas W. Kenny
Associate Professor of Mechanical Engineering
Microsensors based on silicon micromachining

B. (Pierre) T. Khuri-Yakub
Professor (Research) of Electrical Engineering
Acoustic sensors (temperature, film thickness, resist cure), acoustic materials and devices

Gordon Kino
Professor of Electrical Engineering, and, by courtesy, of Applied Physics, Emeritus
Optical fiber sensors

Marc Levoy
Professor of Computer Science and Electrical Engineering
Light field imaging and display, computational imaging and digital photography

Liqun Luo
Professor of Biological Sciences and, by courtesy, of Neurobiology
Biological science, molecular biology, and neurobiology

Michael McGehee
Assistant Professor of Materials Science and Engineering
Polymer optical materials and devices

W. E. Moerner
Professor of Chemistry
Single-molecule spectroscopy, biophysics, nanophotonics, single photon sources

Daniel Palanker
Assistant Professor (Research) of Ophthalmology
Biomedical optics and electronics

Peter Peumans
Assistant Professor of Electrical Engineering
Organic and molecular electronics

Calvin F. Quate
Professor (Research) of Electrical Engineering and, by courtesy, Professor (Research) of Applied Physics
Imaging and lithography applications of scanning probes.

Alberto Salleo
Assistant Professor of Materials Science and Engineering
Laser materials processing, materials and processes for large-area electronics

Krishna Saraswat
Professor of Electrical Engineering
Innovative materials, device structures, process technology of silicon devices and integrated circuits

Mark Schnitzer
Assistant Professor of Applied Physics and Biological Sciences
Biophotonics.

Anthony E. Siegman
Professor of Electrical Engineering, Emeritus
Research and consulting in lasers, optics and fiber optics, including technical and litigation consulting

Olav Solgaard
Associate Professor of Electrical Engineering
Optical micromechanical devices and applications

Jelena Vuckovic
Assistant Professor of Electrical Engineering
Photonic crystal-based optical and quantum optical devices and their integration; solid-state photonic quantum information systems

Brian A. Wandell
Professor of Psychology, and by courtesy, of Electrical Engineering
Image system engineering and visual neuroscience

Yoshihisa Yamamoto
Professor of Electrical Engineering and Applied Physics
Fundamental optoelectronic physics, structures, and devices, quantum computing, quantum information

SPRC Optical Materials Characterization Facility

With initial DARPA/URI support, the Optical Materials Characterization Facility was established in 1992 as part of Stanford's Center for Nonlinear Optical Materials. This facility contains a variety of coherent sources and characterization tools that make possible the rapid measurement of the properties of optical materials and devices. The Characterization Facility is currently operated with funds derived from the SPRC Affiliates' Program, members of which have access to its facilities for support of research on optical materials and devices.

The measurement capability of the SPRC Optical Materials Characterization Facility is summarized below. Contact Dr. Roger Route through the SPRC office/web page for detailed information about the characterization equipment and for access to the facility.

SPRC characterization capabilities:

1. spatially and temporally resolved spectroscopic absorption measurement,

2. photoconductivity and photovoltaic currents at high optical intensities

3. scatter loss at 633 nm and 1064 nm (TMA Inst.),

4. waveguide refractive index profiles (Metricon),

5. variable angle spectroscopic reflectivity and ellipsometric measurements of thin films, waveguides and multilayers (SOPRA GESP) in the 250 - 1750 nm waveband,

6. spectrophotometeric measurements with (Cary 500 and Hitachi U4001) UV-VIS-NIR grating spectrophotometers and (Bio Rad) mid-IR and far-IR Fourier transform spectrophotometers

7. photorefractive gain, diffraction efficiency, and response rates.

Coherent sources in the SPRC Characterization Facility include:

1. Spectra-Physics MOPO 730 Nd:YAG /BBO OPO system, ns pulses 1.84 – 0.21 µm

2. Coherent Mira femtosecond Ti:Sapphire laser system

3. Positive Light Spitfire Ti:S regenerative amplifier, with SHG and THG

4. Spectra-Physics Tsunami femto-second Ti-sapphire laser system,

5. Spectra-Physics OPAL femto-second OPO (1.3 - 2 µm),

6. Coherent Sabre tunable argon lasers

UV and Ultrafast Materials Characterization

The SPRC Optical Materials Characterization Facility has an ultra-fast and UV materials characterization capability with a tunable Coherent Mira/Sabre Ti:Sapphire laser pumping a Positive Light Spitfire/Merlin regenerative amplifier with a frequency doubler/tripler option. Single Guassian mode pulses, either <130 fs or ~1 ps in duration, at a 1 KHz rep. rate are available from 950 to 233 nm, and sum-frequency generation is possible to generate wavelengths shorter than 200 nm. Stretched, flat-top pulses are also available from the harmonic package through the use of a longer set of doubling and tripling crystals. The high spatial and temporal quality output beam was used recently to study UV degradation in nonlinear optical materials such as BBO.

Our ultra-fast capabilities also include a Spectra-Physics OPAL-Tsunami system. Tsunami is a femtosecond, actively mode-locked tunable Ti:sapphire laser producing <130 fs pulses at repetition rate of 80 MHz with average power > 1.5 W. OPAL is a synch-pumped OPO generating <130 fs pulses in a wavelength range covering 1.3 - 2 µm, with average power > 150 mW.

Spectroscopic Measurement of Absorption Loss

The spectroscopic absorption loss apparatus is known as a photothermal common-path interferometer (PCI). It uses the thermo-optic refractive index changes induced by absorbed optical power to monitor the thermalized optical absorption. In its simplest configuration, a pump beam at the wavelength at which the absorption is to be measured is focused coaxially with, but with a smaller waist than, a low-power probe beam. A phase shift is imposed on the central portion of the probe beam by the photothermal index change induced by the local temperature rise resulting from the absorbed pump power. The key feature of the device is a Fourier transforming lens that converts this localized phase shift into an intensity variation. This common path approach is much more robust than conventional methods based on Mach-Zehnder interferometry, and it makes possible near shot-noise limited measurements of the induced phase in a simple, tabletop system. Sensitivities to thermalized optical absorption in the range of 10-6 cm-1 have been demonstrated. A variety of pump lasers have been used, including 1.06 µm and 532 nm Nd:YAG based systems and various Ar-ion laser lines, though the method is applicable with almost any convenient pump laser.
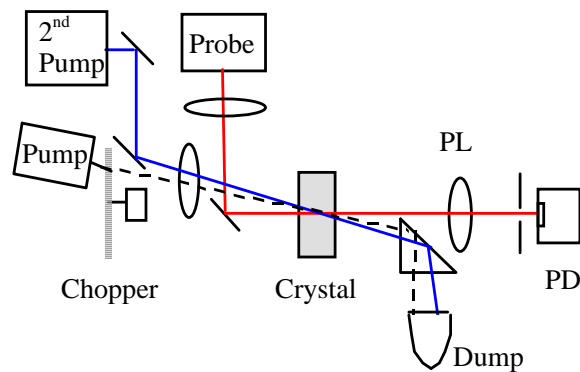
Fig. 1: Crossed-beam setup for low absorption spectroscopic loss measurements.

Modifications to the PCI apparatus in the SPRC facility make use of crossed pump and probe beams, illustrated in Fig. 1, which allows spatially localized measurements for studying inhomogeneous bulk absorption, as well as surface and coating absorption effects. Through the use of two simultaneous pump lasers, we have characterized induced absorption effects such as gray tracking in KTP and green-induced IR absorption (GRIIRA) in LiNbO3. The relatively rapid time response, faster than 100 ms, allows observation of transient absorption effects as well.

Direct measurement of photoconductivity and photovoltaic current

Characterization of photorefractive transport properties, including photoconductivity and photovoltaic currents, at the high intensities characteristic of nonlinear optical devices are difficult by conventional holographic methods. We have developed a transparent contact (liquid electrolyte) cell to measure photocurrents for the characterization of LiTaO3 and LiNbO3. The cell design allows unambiguous measurement with the light beam collinear with the induced current but without the complication of charge accumulation on the surfaces of the samples. Measurements with this apparatus have led to considerable insight into the behavior of stoichiometric lithium niobate and stoichiometric lithium tantalate.

Characterization of materials using spectroscopic ellipsometry

Spectroscopic and multiple angle of incidence ellipsometry is a valuable tool for the determination of the optical constants (n, k) of materials and the characterization of surface and interface morphologies. While

optical transmittance and reflectance measurements provide information on bulk sample properties, ellipsometry has great sensitivity to the properties of the reflecting surface and interfaces in the case of multiple layers. When the optical constants of the materials studied are known, the technique can be used to characterize surface and interface roughness. On the other hand, the measurements can also be used to yield the optical constants of materials. The sample morphology must then be characterized by other techniques, since an accurate reduction of ellipsometric data to the physical quantities of interest requires knowledge of the thicknesses of the constituent layers.

A schematic of the experimental set-up is shown above in Fig. 2. The measurement consists in analyzing the change of polarization resulting from reflection off the surface studied. Wavelengths from 0.25-1.7µm and angles of incidence from 6-90º are accessible using our SOPRA instrument model GESP, which is of rotating polarizer type. The spectra consist of the ellipsometric angles (ψ,Δ), measured typically at 200 points. Experimental data is fit using a linear regression with the purpose of minimizing an error function consisting of the difference between calculated and measured values of the quantities (ψ,Δ). The

$$\rho = r_p/r_s = tg\,\psi e^{i\Delta}$$

ellipsometric angles are defined in terms of the ratio, where r_p, r_s are the complex reflection coefficients for light polarized parallel and perpendicular to the plane of incidence. The reflection coefficients are related to the refractive index n and extinction coefficient k through Fresnel's equations. The optical constants are related to the microscopic properties of the material studied through the dielectric function which is a direct function of the material band structure. Anticipated imperfections, such as rough interfaces and surfaces are described as layers constituted of mixed materials.
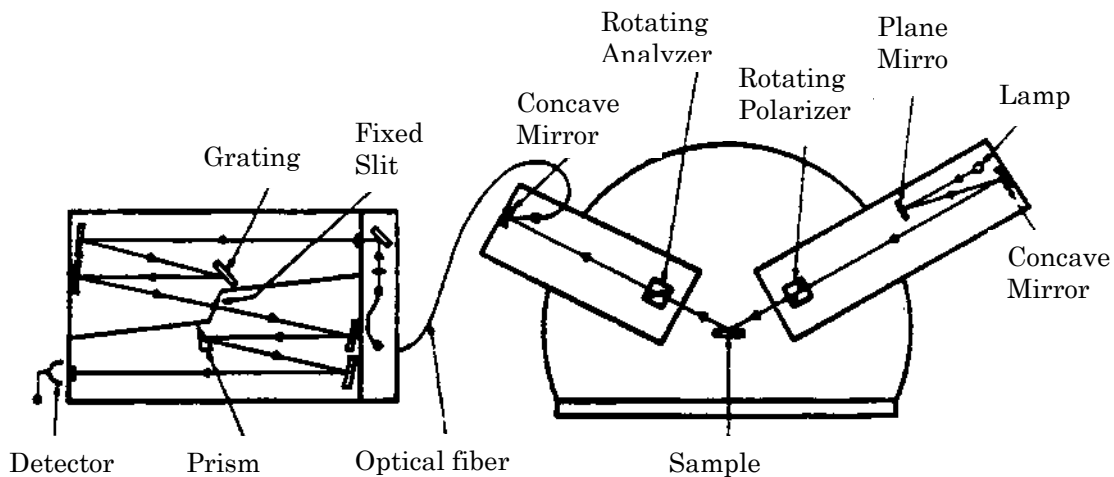

Fig. 2 Schematic layout of spectroscopic ellipsometer..

SPRC Optical MEMS fabrication

The Stanford research community in photonics has access to the Stanford Nanofabrication Facility (SNF) which is a state-of-the-art, shared-equipment, open-use resource in the heart of Stanford campus (http://snf.stanford.edu/). Most wafers are silicon or silicon-on-insulator (SOI) wafers but processing is also possible using quartz or glass wafers. The standard size is 4" but new machines for 6" wafers are being installed.

The optical MEMS fabrication capabilities of SNF are summarized below. Contact Olav Solgaard through the SPRC office/web page for detailed information about the fabrication equipment and for access to the facility.

SPRC optical MEMS fabrication capabilities:
1. optical lithography
2. thin film deposition by chemical vapor deposition (CVD)
3. oxidation and annealing
4. metallization and sputtering
5. dry etching
6. wet etching

Optical lithography
In addition to automatic and manual coating resist spinners (Headway, Laurell and SVG), the SNF has contact exposure machines (Karlsuss, EV aligner) as well as steppers (Nikon, Ultratech).

Thin film deposition by chemical vapor deposition (CVD)
Low pressure chemical vapor tubes allow deposition of polysilicon, silicon nitride, silicon germanium, low temperature oxide (LTO) either undoped or doped with phosphorus (BPSG).

Oxidation and annealing
Atmospheric horizontal tubes (Tylan) are used for oxidation, doping, and annealing heat treatment.

Metallization and sputtering
Several sputtering machines or evaporators (Gryphon, Innotec, Metallica, SCT) can be used to deposit gold, aluminum or other standard microelectronics metals.

Dry etching
Dry etchers is mostly used to perform anisotropic etching. Many machines (AMT, Drytek, Plasma Quest,…)with an extended library of process recipes gives a wide choice that can be tailored to the specific fabrication process in development.
Two Deep Reactive Ion Etchers (DRIE) are available in SNF. They allow researchers to etch vertically deep into the wafers, which is common when fabricating optical microsystems.

Wet etching
Anistropic etchants such as KOH or TMAH can be used at a wetbench to define optical quality mirror surfaces with anisotropic etching.
Cleaning processes before going into a furnace or a lithography step can be performed at these wet benches too.

Characterization tools
The material properties can be tested inside SNF using, among other measurement tools, an ellipsometer, non-contact spectrophotometers or surface profilometers.

Faculty Co-Directors

Prof. Bob Byer
byer@stanford.edu
(650) 723-0226

Prof. Marty Fejer
fejer@stanford.edu
(650) 725-2160

Prof. David Miller
dabm@stanford.edu
(650) 723-0111

For Membership information, please contact:

Dr. Tom Baer
Executive Director
tmbaer@stanford.edu
(650) 723-4406
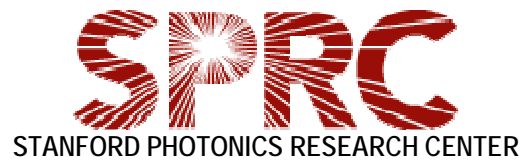
For General information, please contact:

Sara Charbonneau-Lefort
Assistant Director
saracl@stanford.edu
(650) 723-5627

Mailing Address:

Stanford Photonics Research Center
Ginzton Lab- AP 212
450 Via Palou
Stanford, CA 94305-4088

Website:

http:// photonics.stanford.edu

STANFORD PHOTONICS RESEARCH CENTER

2008 Speaker
Abstracts and Biographies

Applications of Nanophotonics to Classical and Quantum Information Technology

Ray Beausoleil

HP

Moore's Law has set great expectations that the performance of information technology will improve exponentially until the end of the next decade. Although the physics of silicon transistors alone might allow these expectations to be met, the physics of the metal wires that connect these transistors almost certainly will not. We will describe a Si-compatible global interconnect architecture that could precipitate an "optical Moore's Law" and allow exponential performance gains until the transistors themselves become the bottleneck. Based on similar fabrication techniques and technologies, we will also present an approach to an optically-coupled quantum information processor for computation beyond Moore's Law, encouraging the development of practical applications of quantum information technology for commercial utilization.

Ray Beausoleil is a Distinguished Scientist in the Information and Quantum Systems Laboratory at HP Laboratories in Palo Alto, California. He received a B.S. in physics from Caltech in 1980 and the Ph.D. degree in physics from Stanford in 1986. At HP Labs, he performs basic research in microscale and nanoscale quantum optics for classical and quantum information processing.

Single Photon Nonlinear Optics with Quantum Dots in Photonic Crystal Resonators
Andrei Faraon
Stanford University

A photonic crystal cavity with a strongly coupled quantum dot is coherently driven using short laser pulses. Depending on the driving frequency, photon blockade or photon induced tunneling is observed. In the case of photon blockade, a single photon trapped inside the cavity can block the transmission of subsequent photons. For photon-induced tunneling the reverse happens, a single trapped photon enhancing the probability of subsequent photons to tunnel into the resonator. These phenomena enable a new class of logic devices based on optical non-linearities at the single photon level. Future photonic crystal devices of this kind will integrate nano-resonators with strongly coupled emitters, interconnected in a photonic network via photonic crystal waveguides. We took the first steps towards this goal and built integrated devices composed of waveguide-coupled cavities with local tuning and out-coupling capabilities. A single quantum dot was used to control the transmission function of the device via dipole induced transparency. Future improvements of the device design will enable logic devices based on photon blockade and photon induced tunneling.

Andrei Faraon received his B.S. in Physics with honors from California Institute of Technology in 2004. Now he is a PhD student in the Applied Physics department at Stanford University where he works with Prof. Jelena Vuckovic on integrated photonic crystal devices for quantum and classical information processes. During his graduate years he published several high impact research articles in peer reviewed scientific journals including Nature and Science. Andrei Faraon is the recipient of the IEEE Ross N. Tucker Award for significant advancements in materials used for semiconductor electronics. Andrei is also interested in applying his research insights to industry, and won an award at the 2007 Stanford Business Plan Competition proposing ultra-fast, low cost photonic crystal lasers for optical communications. He is also a student member of IEEE/LEOS and the Optical Society of America (OSA).

Photoacoustic Tomography
Sam Gambhir
Stanford University

Photoacoustic imaging is an emerging technology that overcomes, to a great extent, the spatial resolution and depth limitations of whole-body optical imaging. Utilizing the photoacoustic effect (discovered by Alexander Graham Bell in 1881), a photoacoustic imaging instrument illuminates a living subject with short laser pulses. The photons, which undergo scattering and absorption as they propagate into the tissue, will reach areas that are up to 5 cm deep. Objects that will absorb the light, such as blood vessels due to hemoglobin light absorption, will convert it into ultrasound waves according to the photoacoustic effect. These ultrasound waves are then detected by a highly sensitive ultrasound transducer (microphone) placed outside the subject.

To date, photoacoustic imaging has only been applied for diseases that exhibit a natural photoacoustic contrast, including: imaging of tumor blood vessels, oxygenation levels of blood vessels and melanoma tumors. However, most diseases will not exhibit a natural photoacoustic contrast, especially in their early stages. Therefore, in order to fully utilize the potential of photoacoustic imaging, it is essential to inject the subject under study an exogenous contrast agent (also referred to as a molecular imaging agent). This imaging agent will travel trough the blood vessels and bind selectively to the diseased sites, introducing a photoacoustic contrast in those sites. Thus far, such photoacoustic imaging agent has not been developed yet and the use of photoacoustic imaging is still limited to endogenous signals only. I will present our progress towards realizing molecular imaging with photoacoustics. This opens up the possibility of new strategies for disease detection in both animals and humans and further adds to the arsenal of growing tools for the field of molecular imaging of living subjects.

Sanjiv Sam Gambhir M.D. Ph.D. is a Professor of Radiology and Bioengineering at Stanford, Chief of the Nuclear Medicine Division, Director of the Molecular Imaging Program at Stanford (MIPS), PI for the National Cancer Institute (NCI) Center for Cancer Nanotechnology Excellence, PI for the NCI In Vivo Cellular & Molecular Imaging Center (ICMIC) (P50) and Program Director for a post-doctoral fellowship molecular imaging training grant (R25T). He currently has a lab of over 25 post-doctoral fellows and graduate students. He also leads a team of over 125 scientists in the molecular imaging program.

Dr. Gambhir has expertise with numerous multimodality molecular imaging modalities. His lab developed reporter gene technologies for use in living subjects including strategies for imaging gene therapy and cell trafficking in humans. His lab has also developed imaging strategies for monitoring protein-protein interactions and is now extending these into strategies for imaging signal transduction. Dr. Gambhir's lab is also developing novel imaging probes for positron emission tomography (PET) and other imaging modalities for use in clinical cancer applications. A key focus is on translation of molecular imaging strategies for improved patient care. Dr. Gambhir serves on numerous corporate scientific advisory boards, has recently founded several companies, and is also a member of the National Cancer Institute scientific advisory board at the NIH.

Dr. Gambhir's recent honors include the Taplin Award (2002), Holst Medal (2003), the Academy of Molecular Imaging Basic Scientist Award (2004), the Society of Molecular Imaging Achievement Award (2004), the Distinguished Clinical Scientist Award from the Doris Duke Charitable Foundation (2004), and the Hounsfield Medal from Imperial College London (2005). In 2006, Dr. Gambhir received the Paul C. Aebersold Award from the Society of Nuclear Medicine, which is given for outstanding achievement in basic nuclear medicine science. In 2006 he was elected as a fellow of the American Institute for Medical and Biological Engineering (AIMBE) and in 2008 he was elected as a fellow of the American Society for Clinical Investigation (ASCI). Dr. Gambhir also co-hosted a Nobel Symposium in Stockholm in 2007 for the Nobel Committee on Molecular Imaging. In 2008, Dr. Gambhir received the Tesla Medal from the United Kingdom Royal College of Radiologists in England for his work on Multimodality Imaging of Living Subjects.

Global Impact of Photonics
John Giddings
Clean Tech Integration

Abstract unavailable

A 17 year veteran of the semiconductor industry, **John Giddings** is the founder of Clean Tech Integration consulting. He is an expert moderator and producer of events evangelizing the New Solar industry. He has produced events and guest lectured for Harvard Business School (HBSTech), ASME, and Santa Clara University. Mr. Giddings is available for business plan consulting and investment opportunity analysis as well as lectures and events promoting the solar century.

High-power LED technology - Enabling solid state lighting

Werner Götz

Philips LED

High power light emitting diodes based on III-nitride materials continue to increase in light output and performance with the best white devices today emitting over 140 lm/W from a 1x1 mm2 chip when driven at 350mA. The high flux and increasing power conversion efficiency of these devices is enabling many new applications for LEDs and spurring significant growth in the general illumination space sooner than generally anticipated. Examples of these applications are retail spot lighting, street lighting, and automotive forward lighting.

Werner Goetz received his Ph.D in Physics from the University of Erlangen, Germany. He has been with Hewlett-Packard Company/Agilent Technologies/LumiLeds Lighting/Philips Lumileds Lighting Company since October 1996 where he is currently the Director of Epitaxy Technology. Prior to his employment with HP, he was a post-doctoral fellow at Stanford University and the Xerox Palo Alto Research Center. Dr. Goetz has over 15 years experience working with III-V nitride semiconductors for application in light emitting diodes.

High Harmonic Generation from Multiple Orbitals

Markus Guehr

Stanford PULSE Institute

We use high harmonic generation (HHG) for probing electrons on atoms and molecules on ultrafast timescales. HHG proceeds in three steps: (1) a part the electron wave function corresponding to the highest occupied molecular orbital (HOMO) tunnels into the continuum; (2) it is accelerated in a strong oscillating optical field; (3) it recollides with the HOMO thereby transferring its kinetic energy into extreme ultraviolet photons.

We have observed simultaneous HHG from two molecular electronic orbitals, the HOMO and the next lower bound HOMO-1 in molecular nitrogen. The HOMO-1 is revealed through enhancements in the HHG signal at characteristic alignment angles of the molecular axis to the polarization of the harmonic driving pulse.

Furthermore we show phase measurements for the harmonics generated on N_2 and argon. We observe the Cooper minimum, a phenomenon known from photoionization, as an amplitude dip and a phase jump for argon.

Markus Guehr studied Physics at the Freie Universitaet Berlin (Germany) and Cambridge University (England). During his time as a grad student in the group of Prof. Schwentner in Berlin, he investigated the coherent ultrafast dynamics of small molecules in rare gas crystal hosts. He applied coherent control to understand the decoherence mechanisms of vibrational and electronic wave packets. Furthermore, he found that coherent phonons are excited and probed by molecular dopands. He finishing his PhD in 2005 and received the Ernst- Reuter Prize for it. After one more year as a PostDoc in Berlin, he extended his interest to strong field molecular physics. He set up a high harmonic lab with the grad students Brian McFarland and Joe Farrell in Phil Bucksbaums group at Stanford University. Therefore he received a fellowship from the Humboldt Foundation. He is now an Associate Staff Scientist and leads the High Harmonic Generation project in the Stanford PULSE Institute.

Modulation of Single Photons and Biphotons
Steve Harris
Stanford University

The talk will describe techniques for modulating the amplitude and phase of single photons and biphotons. We also describe a quantum process termed as nonlocal nonlocal modulation. Here, phase modulation of one photon of an entangled pair, as measured by correlation in the frequency domain, may be negated or enhanced by modulation of the second photon.

Professor Stephen E. Harris received his B.S. in Electrical Engineering from Rensselaer Polytechnic Institute in 1959. In 1963 he became a member of the Stanford faculty where he is now the Kenneth and Barbara Oshman Professor of Engineering with appointments in Electrical Engineering and Applied Physics. Professor Harris has advised about 60 Ph.D. students and is known for contributions to quantum optics, nonlinear optics, and laser science.

Global Impact of Photonics
Waguih Ishak
Corning

Waguih Ishak received his B.Sc.E.E., B.Sc.Math., M.Sc.E.E., and Ph.D.E.E. Degrees in 1971, 1973, 1975, and 1978, respectively. In 1999, Waguih completed the Stanford Executive Program at Stanford University.

He joined Hewlett-Packard Laboratories in 1978 and worked on magnetic bubble propagation and detection circuits and surface acoustic wave (SAW) low-loss filters. In 1981, he became a project leader and in 1983 he was the project manager of the Sources and Signal Processing Group, responsible for transferring SAW and nonlinear gallium arsenide technologies to HP's Spectrum Analyzer and Oscilloscope divisions.

In 1987, Waguih became the manager of the Photonics Technology Department of the Instruments & Photonics Laboratory which is responsible for R&D programs in fiber optics, integrated optics, optoelectronics, micro-optics, and optical interconnects for applications in measurements, communications (datacom and telecom), and computer interconnects. The department was responsible for generating a new business for HP in lightwave test and measurement such as lightwave component and spectrum analyzers, tunable laser sources, frequency and time-domain reflectometers, and polarization analyzers. The department was also responsible for starting new R&D programs in the areas of vertical cavity surface emitting lasers (VCSEL), high-speed parallel optical interconnects (POLO), optical measurements for process monitoring and control, and electronic digital films for photography and memory applications.

In 1995, Waguih was promoted to Director of the Communications & Optics Research Laboratory (CORL). Waguih led his R&D team in the areas of photonics (fiber optics, integrated optics, optoelectronics, and micro-optics) and integrated electronics. The emphasis was on fiber-optic communications, wireless communications and the use of optics and electronics in novel applications in communications, computations and measurements. Many products came out from the research work such as the optical mouse, the photonic switch and the parallel optical interconnects modules.

In 2005, Waguih became the Vice President and Chief Technology Officer at Avago Technologies. Waguih managed the company's U.S. Advanced R&D Center and was responsible for creating technologies for its Electronic Components Business Unit (ECBU).

In 2007, Waguih joined Corning, Inc., as a VP and Director, to start the West Coast Research Group in Santa Clara, California. Waguih has authored about 80 journal and conference papers, and four chapters in the "Handbook of Electronic Instruments." He is a Fellow of the IEEE and was named an inventor on seven US patents.

Advanced Imaging Techniques for Biology
Na Ji
HHMI

Biological processes occur on spatiotemporal scales spanning many orders of magnitude. Greater understanding of these processes therefore demands improvements in the tools used in their study. I will first describe our recently developed pulse splitter, which permits faster two photon imaging with reduced photobleaching and photodamage. I will then describe our ongoing efforts to apply adaptive optics to increase the spatial resolution and depth of penetration during in vivo imaging of the mouse neocortex.

Na Ji studied chemical physics as an undergraduate student in the University of Science and Technology of China, where she won the Guo Moruo Fellowship. She received her Ph.D. degree in chemistry, specializing in sum frequency generation in the lab of Prof. Yuen-Ron Shen at the University of California, Berkeley. Since 2006, she has been working with Dr. Eric Betzig at the Janelia Farm Research Campus of Howard Hughes Medical Institute, where her research focuses on improving the speed and resolution of in vivo brain imaging, and applying the resulting techniques to outstanding problems in neurobiology.

Optical Interconnects in Supercomputers and High Performance Servers

Jeffrey A. Kash

IBM Research

Optical interconnects offer significant advantages for future high performance computers. Uses for and progress towards new technologies for optical interconnects are reviewed. Today, fiber-based parallel optical modules are replacing electrical cables. In the next few years, on-card optical interconnects using multimode polymer waveguides will come into use. Eventually, optical interconnects will move onto microprocessor chips using silicon photonics.

Dr. Jeffrey Kash joined IBM Research in 1981, initially studying femtosecond electron and exciton dynamics in semiconductors. In 1995, Dr. Kash co-invented Picosecond Imaging Circuit Analysis, an optical technique which is used today to debug advanced CMOS ICs. Since 2000, Dr. Kash has focused on the use of optical interconnects in computers. He directs DARPA-sponsored IBM programs for chip-to-chip optical interconnects and nanophotonic optical switches. He also has responsibility for optical interconnects in next and future generations of supercomputers. Dr. Kash has published over 140 papers in major technical journals and holds 22 patents, and is a fellow of both the APS and IEEE.

Nano-imaging with a Metallic Nanolens
Satoshi Kawata
Osaka University

Abstract unavailable

Satoshi Kawata is the Director of the Photonics Advanced Research Center at Osaka University. He is also a Professor of Department of Applied Physics since 1993. He is jointly at RIKEN as a Chief Scientist (the head) of Nanophotonics Laboratory since 2002. He received his BSc, MSc and PhD all in Applied Physics from Osaka University in 1974, 1976 and 1979 respectively.

He has been serving as the President of Spectroscopical Society of Japan (2004-2007), the Editor for Optics Communications (2000-present), Honorary Professor at Technical Institute of Physics and Chemistry, Chinese Academy of Science, Program Officer at Japan Society for the Promotion of Science and a joint professor at the Department of Physics at Gakushuin University. He is a fellow of the Optical Society of America (OSA), Institute of Physics (IOP), the International Society for Optical Engineering (SPIE) and the Japan Society of Applied Physics (JSAP).

He received the Medal with Purple Ribbon awarded by the Emperor of Japan (2007), the Minister's Award on Science and Technology by the Ministry of Education, Culture, Sports, Science and Technology Japan (2005), Shimadzu Award (2003), Ichimura Award (1998), DaVinci Excellence, Moet Hennessy Louis Vuitton (1997) and the Japan IBM Science Award (1996).

Nanoscale Photodetectors Enhanced by Optical Antennas
Salman Latif
Stanford University

The use of optics to make connections within and between electronic chips has been the subject of research for over 20 years because it could solve many of the problems experienced in electrical systems. A critical challenge for the convergence of optics and electronics is that the micrometer scale of optics is significantly larger than the nanometer scale of modern electronic devices. In the conversion from photons to electrons by photodetectors, this size incompatibility often leads to substantial penalties in power dissipation, area, latency and noise. A photodetector can be made smaller by using a subwavelength active region which, however, could result in very low responsivity because of the diffraction limit of the light.

In our first approach to tackle this problem, we use a C-shaped nano-aperture antenna in a thin metal layer to enhance the photocurrent response of a subwavelength photodetector. The work is the first demonstration of a plasmonic-enhanced semiconductor photodetector at near-infrared wavelengths. In our second approach, we exploit the idea of a dipole antenna from radio waves, but at near infrared wavelengths (~ 1.3 µm), to concentrate radiation into a nanometer-scale Ge photodetector. Despite the small antenna size (~ 380 nm long) and the different properties of metals at such high frequencies (~ 230 THz), the antenna has qualitatively similar behavior to the common radio-frequency half-wave Hertz dipole. It gives a relative enhancement of 20 times in the resulting photocurrent in the subwavelength Ge detector element, which has an active volume of 0.00072 _m3, two orders of magnitude smaller than previously demonstrated detectors at such wavelengths. Finally, we integrate an antenna-enhanced photodetector on a commercial CMOS chip, which is the first demonstration of any plasmonic effect in Si CMOS. Photodetectors are one of the most critical components in optoelectronic integration, and decreasing their size may enable novel chip architectures and ultra-low electrical and optical power operation.

Salman Latif received the B.Eng (Honors) degree in Electrical Engineering from McGill University, Montreal, Canada, in 2002, and the M.S degree in Electrical Engineering from Stanford University, Stanford, CA in 2004. He is currently a Ph.D student in Electrical Engineering at Stanford University. He is interested in the integration of optoelectronic devices with Silicon electronics for interconnect and clocking applications, and is currently involved in the design and characterization of low capacitance CMOS compatible photodetectors.

Quantum Information Processing with Trapped Ions*

D. Leibfried

National Institute of Standards and Technology, Boulder, Colorado 80305, USA

Atomic ions confined in an array of interconnected traps represent a potentially scalable approach to quantum information processing. All basic requirements have been experimentally demonstrated in one and two qubit experiments and simple quantum algorithms have been demonstrated with up to 8 qubits. The remaining task is to scale the system to hundreds and later thousands of qubits and minimize errors in the system. While this requires extremely challenging technological improvements, no fundamental roadblocks are currently foreseen. The talk will introduce the basic ideas behind this particular approach, give a survey of recent progress in implementing simple quantum algorithms and describe the efforts in scaling up towards a large scale computing device.

Dietrich Leibfried received his diploma (1991) and doctorate degree (1995) in physics while working on precision laser spectroscopy of hydrogen with Theodor W. Hänsch at the Max-Planck Institute for Quantum Optics in Garching, Germany. He has been working in the field of quantum information since his post-doctoral appointment in David Wineland's group at NIST in 1995. From 1998 to 2001 he collaborated with Rainer Blatt holding an assistant professor position at the University of Innsbruck. In spring 2001 he joined NIST in a staff position as co-leader of the group working on quantum information with trapped ions there. Leibfried's honors include the 1993 Helmholtz-prize of the German national institute for physics (PTB), the 2000 START-prize for young researchers of the Austrian Science Foundation (FWF) and the 2004 Rudolf-Kaiser prize of the Stifterverband der Wissenschaften in Germany. He is a fellow of the American Physical Society and has published more than 80 peer-reviewed articles.

Femtosecond X-ray Studies of Materials
Aaron Lindenberg
Stanford University

I will describe recent experiments and new opportunities in which ultrafast laser techniques are coupled with atomic-scale resolution x-ray techniques to probe the dynamical properties of materials at the level of atoms and electrons.

Aaron Lindenberg is an Assistant Professor with a joint appointment in the Materials Science and Engineering Department and the Photon Science Department at Stanford University and the Stanford Linear Accelerator Center.

Two Micron Fiber Laser
Peter Moulton
Q Peak, Inc.

The Tm:fiber laser, operating in a broadly tunable region around 2000 nm, can be operated efficiently when the fiber core is heavily doped. In that case, one pump photon at 790 nm can generate two laser photons, due to a cross relaxation process between pairs of Tm ions. We will discuss scaling efforts with Tm:silica fibers, where we have generated cw powers as his as 885 W. Applications of the laser system include eyesafer directed energy, high-power mid-IR sources and laser-driven electron accelerators for high-energy physics investigations.

Peter Moulton was born in Springfield, Massachusetts in 1946. He received an A.B. in Physics from Harvard College in 1968 and M.S. and Ph.D. degrees in Electrical Engineering from M.I.T. in 1972 and 1975 respectively. After finishing graduate school he was employed in the Quantum Electronics Group at M.I.T. Lincoln Laboratory, Lexington, Massachusetts. In 1985 he joined a start-up company, Schwartz Electro-Optics, as Vice-President and managed the founding of the company's Research Division in Concord, Massachusetts. He became Senior Vice-President of SEO in 1997 and was involved in spinning out the Research Division as a separate company, Q-Peak, in 1998, and in the sale of Q-Peak to its current parent company, Physical Sciences Inc. in 2001. At present he is the Vice-President and Chief Technology Officer of Q-Peak.

Moulton's technical work began in the field of bulk solid state lasers, and in recent years has extended to include nonlinear optics and fiber lasers. Some of his work has been motivated by defense applications, including infrared countermeasures, detection of chemical and biological weapons, advanced ladar and targeting systems, laser communications and directed-energy systems. He has also been involved in scientific applications, including global monitoring of atmospheric water vapor, ozone aerosols and wind, in commercial applications in the semiconductor industry, in laser systems for medical treatment and diagnostics, and in the development of lasers for large-screen color displays.

Dr. Moulton is a Fellow of the Optical Society of America (OSA.) He was awarded the R.W. Wood Prize from the OSA and the William Streifer Scientific Achievement Award from IEEE/LEOS, both in 1997, and in 2000 he was elected to the National Academy of Engineering.

DSP Enabled 10Gb/s, 40 Gb/s and 100 Gb/s Transmission for Optical Mesh Networks

Maurice O'Sullivan

Optical network solutions arise from a dynamic equilibrium of past practice, growing demand, fixed geography, and scarcity of resources (including time). I will describe physical layer aspects of commercial solutions which make use electric field transmission and electronic DSP to meet present and future requirements of optical networks.

Maurice O'Sullivan has worked for Nortel for a score of years, at first in the optical cable business, developing factory-tailored metrology for optical fiber, but, in the main, in the optical transmission business developing, modeling and verifying physical layer designs & performance of Nortel's line and highest rate transmission product including OC-192, MOR, MOR+, LH1600G, eDCO and eDC40G. He holds a Ph.D. in physics (high resolution spectroscopy) from the University of Toronto and is a Nortel Fellow.

Next-Generation WDM Transport Enabling Zettabyte IP Network Evolution

Loukas Paraschis
Cisco Systems

Abstract unavailable

Loukas Paraschis is business development manager at Cisco, responsible for next generation core networks in the emerging markets, service provider, solution architectures and scaling group. At Cisco, he has worked also on optical transport technologies, WDM systems, multi-service metro and IP-over-WDM architectures, and the associated business models and market development efforts. Prior to his current role, Loukas worked as an R&D engineer, product manager, and technical leader in optical networks and core routing, and completed graduate studies at Stanford University (PhD Applied Physics 1999, MS EE 1998). He has (co)authored more than 50 peer-reviewed publications, invited, and tutorial presentations, a book chapter, multiple technical reports, and three patent applications, and has been associate editor for optical networks of the Journal of Communication Networks, guest editor of the IEEE Journal of Lightwave Technology, and member of the IEEE (SM '06), the OSA, and multiple conference organizing committees. Loukas was born in Athens, Greece, where he completed his undergraduate studies.

Real-Time Chemical Sensors Based on Novel NLO Laser Systems

James J. Scherer, Ph.D.
NovaWave Technologies, Inc.

Advancements in chemical sensor systems that employ novel difference and sum frequency generation laser sources are presented. NovaWaves commercial laser sources that are based on NLO conversion in various poled media are discussed, and the integration of these unique laser products with absorption and emission spectroscopies to comprise ultrasensitive, real-time chemical sensor systems is presented. Examples of dedicated sensor systems designed to measure greenhouse gases, pollutants, and other species are presented. The ability to combine tunable fiber laser and diode laser technology with NLO media to access molecular "fingerprint" spectral regions is highlighted.

Dr. James Scherer received his Bachelors degree in Physics and Art at Berkeley, followed by a graduate degree in Chemistry also from Berkeley in 1994 under Professor Richard J. Saykally. From there, he spent several years at Sandia Livermore, and was subsequently a Partner and Director of R&D at Los Gatos Research, Inc. Dr. Scherer co-founded NovaWave with Dr. Joshua Paul in 2002. Dr. Scherer has been intimately involved with the development of cavity-enhanced (e.g. cavity ringdown) spectroscopies, and is inventor of Ringdown Spectral Photography (RSP) and co-inventor of Integrated Cavity Output Spectroscopy (ICOS).

Dielectric Optical Antenna Emitters
Jon Schuller
Stanford University

Optical antennas are rapidly becoming a critical component in nanophotonics research due to their unparalleled ability to concentrate electromagnetic energy into nanoscale volumes [1]. Optical antennas have been used to drastically enhance nonlinear [2] and Raman [3] cross-sections, to make nanoscale optical probes [4], and to modify the emission direction of individual molecules [5]. For operation at near-IR to terahertz frequencies, researchers typically construct such optical antennas from wavelength-size metallic structures. However, recent research has begun to exploit the scattering resonances of high-permittivity particles to realize all-dielctric optical antennas, emitters, and metamaterials [6,7]. In this talk, the resonant modes of subwavelength rod-shaped dielectric particles will be characterized experimentally and theoretically and their use in novel infrared light emitters will be demonstrated.

At mid-infrared frequencies, Silicon Carbide (SiC) exhibits a rich variety of optical phenomena; near the TO phonon frequency, the dielectric function exhibits a sharp resonance. At frequencies above this resonance SiC has a negative permittivity and the optical response is similar to metals. At low frequencies, the permittivity reaches large positive values and the material behaves like a dielectric. Using infrared spectroscopy we study individual rod-shaped SiC particles and examine polarization and size effects that are normally obscured in ensemble measurements. By comparing results with analytical Mie calculations for infinite cylinders, we show that rod-shaped SiC particles exhibit four distinct resonant modes spanning both frequency regimes of interest (metallic and dielectric).

Detailed investigations of these SiC optical antennas reveal a wealth of new physics and applications. We discuss the distinct electromagnetic field profile for each mode, and demonstrate that two of the dielectric-type Mie resonances can be combined in a particle array to form a negative index metamaterial [8]. These experiments and calculations illustrate how such particles may serve as "receiving" antennas which resonate in response to external illumination. Most recently, however, we have shown that these particles can also serve as "broadcasting" antennas. Using a custom-built thermal emission microscope we have collected emissivity spectra from single SiC particles at elevated temperatures and compared them to our previous measurements. Emission spectra highlight the use of these optical antennas as subwavelength resonant light emitters, and reveal interesting coupling effects between resonant particles and an underlying substrate. These antennas may find applications in novel types of sources with an engineered spectral emissivity that greatly differs from a traditional black body.

Jon Schuller graduated with high honors from UC Santa Barbara in 2003, earning a Bachelor of Science degree in physics. He has been an applied physics student at Stanford since 2003, working for the group of Professor Mark Brongersma. Jon's thesis focuses on the physics of infrared optical antennas and their application to metamaterials and novel light emitters. He plans to graduate by the fall of 2009.

Quantum Measurement with Superconducting Circuits

Irfan Siddiqi
UC Berkeley

The Josephson tunnel junction is a unique electronic circuit element which is both non-linear and non-dissipative. This combination makes it well suited to measure the state of a quantum mechanical system with high fidelity and minimum back-action. I will describe the operation of a new type of Josephson amplifier, based on a dynamical bifurcation, and demonstrate how it can be used to measure a quantum spin ½ system.

Irfan Siddiqi received his AB (1997) in chemistry & physics from Harvard University. He then went on to receive a PhD (2002) in applied physics from Yale University, where he stayed as a postdoctoral researcher until 2005. Irfan joined the physics department at the University of California, Berkeley in the summer of 2006. His research group, the Quantum Nanoelectronics Laboratory, investigates the quantum coherence of various condensed matter systems ranging from microscopic nanomagnets such as single molecule magnets to complex macroscopic electrical circuits. In 2006, Irfan was awarded the George E. Valley, Jr. prize by the American Physical Society for the development of the Josephson bifurcation amplifier. He has also been awarded the Office of Naval Research Young Investigator Award, the Air Force Office of Scientific Research Young Investigator Award, the Hellman Family Faculty Fund, and the UC Berkeley Chancellor's Partnership Faculty Fund.

Photonics Applications in Driver Assistance Systems
Arne Stoschek
Volkswagon

The talk will discuss photonics applications in automotive driver assistance systems, with particular focus on LED and laser technologies.

Arne Stoschek has held several positions at Volkswagen Group of America, Electronics Research Laboratory in Palo Alto, CA. Most recent "Head of Driver Information and Assistance". Lead activities on in-vehicle instrumentation, sensors, intelligent vehicles, and novel electronic systems in cars. Build partnerships between Volkswagen Group and technology companies in the US. Experienced automotive product cycles from early technology idea to production in a car. Board of Directors position at Volkswagen Autovision Ventures portfolio company in the US.

- Manager, Emerging Technologies at Infineon Technologies North America Corp., San Jose, CA in Corporate Research Division and Venture Capital Division. Responsible for US office of Corporate Research Division. Focus on wireless systems, bioelectronics, polymer electronics.

- Research Fellow at Stanford University, CA, Departments of Neurobiology and of Statistics. Research on algorithms for exploration and visualization of multidimensional biomolecular data. Publications in Nature and IEEE Transactions.

- Research Associate at Max-Planck-Institute for Biochemistry, Germany, Department of Structural Biology. Research on computer vision and statistical data processing algorithms for imaging of proteins at molecular resolution.

- Ph.D. in Electrical Engineering with minor in Biophysics at Technical University of Munich and Max-Planck-Institute for Biochemistry, Germany - Studied Electrical Engineering at University of California at Berkeley, CA and Dresden University of Technology, Germany

Global Impact of Photonics
Steve Turner
Pacific Biosciences

Dr. **Steve Turner** founded Pacific Biosciences (formerly Nanofluidics) and secured its series A funding in 2004. Dr. Turner was a member of the original project team that published the foundations of Pacific Biosciences' technology. Dr. Turner performed his Ph.D studies at Cornell University with Professor Harold Craighead studying the behavior of biomolecules in nano-fabricated fluidic structures. His work contributed to the establishment of the Nanobiotechnology Center at Cornell. He has a triple major BS in Physics, Applied Mathematics and Electrical Engineering from the University of Wisconsin, Madison. Dr. Turner is author of over 30 scientific papers in fields ranging from nanofluidics and DNA, cell attachment to chemically and topographically modified surfaces, and x-ray lithography and process modeling. Dr. Turner is inventor on 9 issued U.S. patents and over 20 published applications. Dr. Turner was awarded the MIT Technology Review TR 100 award in 2003 and the University of Wisconsin Madison Distinguished Young Alumnus Award in 2008. Currently, Dr. Turner is a member of the NIH ISD Study Section and sits on the Board of Directors for Pacific Biosciences. He oversees the scientific and technical direction of the company.

Self-phase-locked Degenerate Synchronously Pumped Optical Parametric Oscillator

Samuel Wong
Stanford University

We demonstrated a stable femtosecond synchronously pumped optical parametric oscillator (SPOPO) that self-phase-locked when operating at degeneracy without any need for active stabilization. The nonlinear gain element was a 1-mm-long type-I periodically poled MgO:LiNbO_3 crystal phase-matched for 1550 nm. A mode-locked Ti:sapphire laser generating 180-fs pulses at 80 MHz was employed as the pump at 775 nm. The spectral bandwidth of the degenerate signal/idler was 50 nm around 1550 nm or 200 cm^-1 and thus exhibited an output comb broadening of about 3. The corresponding pulse duration was 70 fs, which was transform-limited for Gaussian pulses. Phase-coherence between the degenerate SPOPO output and the pump was confirmed using separated beat note measurement techniques with respect to the pump laser and with respect to an independent CW laser serving as an external phase reference. The frequency locking range of the degenerate state was measured to vary as a square root of the number of times above pump threshold (i.e., parametric gain) and as a linear function of the output coupling (i.e., inverse cavity Q). The data appeared consistent with steady-state injection locking. The self-phase-locked SPOPO operated stably for up to 1 hour provided that there was minimal environmental noise. As a divide-by-2 sub-harmonic generator, the degenerate SPOPO is a novel source for extending phase-stable frequency combs to longer wavelengths. Cascading these broadband phase-locked systems and implementing phase-preserving optical parametric amplifiers (OPA) can produce high-peak-power combs at mid-IR wavelengths unavailable to solid-state lasers and useful for high-precision metrology and high-resolution spectroscopy.

Sam Wong received both his B.S. and M.Eng. degrees in Electrical Engineering and Computer Science in 2001 at the Massachusetts Institute of Technology, where he worked on fiber optics and dispersion-managed solitons with the late Prof. Hermann Haus. He is currently a Ph.D. candidate in the Electrical Engineering department at Stanford University, where he works with Prof. Robert Byer on ultrafast lasers and nonlinear optics as well as novel laser material.

Optical Clocks and Applications

Jun Ye

JILA, National Institute of Standards and Technology and University of Colorado

Quantum state engineering of ultracold matter and precise control of optical fields have allowed accurate measurement of light-matter interactions for applications in precision tests of fundamental physics. State-of-the-art lasers now maintain optical phase coherence over one second. Optical frequency combs distribute this optical phase coherence across the entire visible and infrared parts of the electromagnetic spectrum, leading to direct visualization and measurement of light ripples. An the same time, ultracold atoms confined in a carefully engineered optical lattice allow us to minimize quantum decoherence while strengthen the clock signal. For ^{87}Sr, we achieve a resonance quality factor $>2 \times 10^{14}$ on the $^{1}S_0 - {}^{3}P_0$ doubly forbidden clock transition at 698 nm. The uncertainty of this new clock has reached 1×10^{-16} and its instability approaches 1×10^{-15} at 1 s. These developments represent a remarkable convergence of ultracold atoms, laser stabilization, and ultrafast science. Further improvements are still tantalizing, with quantum measurement and precision metrology combining forces to explore the next frontier.

Jun Ye received his Ph.D. degree from the University of Colorado, Boulder, in 1997. He was a R.A. Millikan Postdoctoral Fellow at the California Institute of Technology from 1997-1999. He has been a Fellow of JILA, the National Institute of Standards and Technology and the University of Colorado, since 2001. He is a Fellow of NIST, a Fellow of the American Physical Society, and a Fellow of the Optical Society of America. His research interests include precision measurement, ultracold atoms and molecules, optical frequency metrology, and ultrafast science and quantum control. He has co-authored over 200 technical papers and has delivered over 200 invited talks. Awards and honors include I. I. Rabi Prize from the American Physical Society, Carl Zeiss Research Award, William F. Meggers Award and Adolph Lomb Medal from the Optical Society of America, Arthur S. Flemming Award, Presidential Early Career Award for Scientists and Engineers, U.S. Commerce Department group Gold Medal, Friedrich Wilhem Bessel Award from Alexander von Humboldt Foundation, and Samuel Wesley Stratton Award from NIST. The research group web page is http://jilawww.colorado.edu/YeLabs/.

Road Modeling using Photonics in Autonomous Driving
Wende Zhang
GM

This talk will introduce the SPRC audience of the General Motor's research efforts on computer perception to improve driving safety. We will describe the DARPA Urban Challenge, which is a 60-mile race through an urban environment where vehicles had to follow the traffic rules, and GM-CMU's entry Boss, the autonomous vehicle that won the challenge. We will overview Boss's system architecture and highlight its road modeling technologies using photonic sensors. We will also discuss a clear path detection method which is the next step to further improve the road modeling for autonomous driving.

Wende Zhang has been with General Motors R&D and Planning, Warren, Michigan, since July 2005, where he is currently a senior researcher. He led the efforts on using computer vision to improve driving safety. Wende was also the technical lead on computer vision in the GM-CMU team that won the DARPA Urban Challenge. His work includes seven patents filed and 19 publications. He received the M.S. and Ph.D. degrees in electrical and computer engineering from the Carnegie Mellon University, Pittsburgh, Pennsylvania, in 2002 and 2006, respectively. He received the B.S. degree in electronics engineering from the Shanghai Jiao-Tong University in 2001. Wende served as program committee of Sigma Xi at GM R&D chapter since 2007.

STANFORD PHOTONICS RESEARCH CENTER
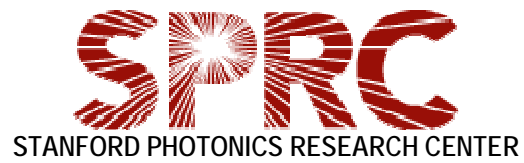
2008 Poster Abstracts

A. INFORMATION TECHNOLOGY

Megabits Secures Key Rate Quantum Key Distribution
Qiang Zhang

Quantum cryptography can provide unconditionally secure communication between two authorized parties based on the basic principles of quantum mechanics. However, imperfect practical conditions limit its transmission distance and communication speed. Here we implement differential phase shift quantum key distribution with up-conversion assisted hybrid photon detector to achieve 1.3 M bits per second secure key rate over a 10-km fiber. This is the first megahertz bit rate QKD tolerant against the photon number splitting attack, general collective attacks on individual photons, and any other known sequential unambiguous state discrimination attacks.

B. INTEGRATED PHOTONICS

SiGe/Ge Quantum Well Modulators Employing the Quantum-Confined Stark Effect
Stephanie A. Claussen, Ross Audet, Elisabeth Edwards, Onur Fidaner, David A. B. Miller, Shen Ren, Jonathan E. Roth, Rebecca K. Schaevitz, Lilian Tran

Germanium is increasingly important for integrating photonics into silicon IC technology. Recent demonstrations of the quantum-confined Stark effect (QCSE) in SiGe/Ge quantum wells (QWs) open many new device possibilities, including high-performance, group IV optical modulators and detectors. These QW designs show a strong electroabsorption affect, which led to the first QCSE-based electroabsorption modulators in SiGe. Here, we begin by investigating some of the key materials properties that affect our QW device design. These include the quantum mechanical transitions that occur in the QWs and the femtosecond dynamics of the photoinduced carrier populations. We then go on to present the results from a number of different device structures, including a waveguide modulator and detector and a novel side-entry modulator on silicon and silicon-on-insulator (SOI) wafers.

MEMS Optical Filter with Tunable Center Wavelength and Passband
Jae-Woong Jeong, Il Woong Jung, Olav Solgaard

A tunable optical bandpass filter is a key technology for dynamic wavelength provisioning in reconfigurable optical networks and communication systems. Among several methods implementing tunable optical filters, MEMS technology has strong potential for high-performance filters. Based on MEMS platform technology, we introduce a tunable MEMS optical bandpass filter with large vertical mirrors (450um tall) assembled on MEMS actuators. The fabrication process requires only one mask, and the platform technology allows a compact chip size with high optical quality vertical mirrors. In addition, electrostatic combdrive actuators enable independent and continuous control of center wavelength and optical passband. The

fabricated electrostatic combdrive actuator has the maximum stable displacement of ~45um to the left and ~50um to the right, therefore achieving the maximum tuning range of ~95um.

Spectral Analysis of Scattering in Metal-Insulator-Metal Waveguides and Related Equivalent Circuit Models

Sukru Ekin Kocabas, Shanhui Fan, David A.B. Miller, Georgios Veronis,

We show that the two dimensional MIM plasmonic waveguide has a discrete and a continuous spectrum, similar to the dielectric slab waveguide. Using this complete spectrum, we calculate the equivalent circuit model for waveguide junctions.

Plasmonic Photodetectors In Si CMOS

Salman Latif, David. A. B. Miller, Liang Tang

We present a plasmonic photodetector integrated in a commercial CMOS chip. This is the first demonstrated plasmonic effect in Si CMOS. We demonstrate the polarization dependence of the photocurrent obtained from a C-aperture detector, which is direct evidence of an antenna effect. We also show find that the photocurrent density of a CMOS detector is enhanced three times with a C-shaped nanoaperture.

Tunable and Coherent Thermal Conductance of Multilayer Photonic Crystals

Wah Tung Lau, Shanhui Fan, Jung-Tsung Shen, Georgios Veronis

We consider coherent radiative thermal conductance of a multilayer photonic crystal. The crystal consists of alternating layers of lossless dielectric slabs and vacuum, where heat is conducted only through photons. We show that such a structure can have thermal conductance below vacuum over the entire high temperature range due to the presence of partial band gap in most of the frequency range, as well as the suppression of evanescent tunneling between slabs at higher frequencies. The thermal conductance of this structure is highly tunable by varying the thickness of the vacuum layers.

Integrated Photodetectors in Metal Slot Plasmonic Waveguides

Dany-Sebastien Ly-Gagnon, Sukru Ekin Kocabas, David A.B. Miller

We developed a characteristic impedance model to investigate the transmission properties of plasmonic metal slot waveguides. We used this model to design photodetectors integrated in metal slot plasmonic waveguides.

Fabrication of Monolithic Silicon Photonic Elements and their Applications

Shrestha Basu Mallick, Il Woong Jung, Chia-Ming Chang, Sora Kim, Sanja Hadzialic, Olav Solgaard

Photonic Crystals (PCs) provide precise control over optical fields. Fabrication of Silicon PCs by etching into silicon using a single lithographically-defined etch mask has many advantages including simple processing, self-aligned structures, high quality reflecting surface (because of sub nm roughness and very low internal stress), tolerance of high temperature processing, resistance to corrosive chemicals, and compatibility with standard MEMS and IC processing. Also, the power handling capacities of such structures is expected to be higher. The GOPHER (Generation Of Photonic Elements by RIE) process utilizes alternate anisotropic reactive ion etching and isotropic etching to introduce a vertical refractive index variation. These structures are well suited for designing high quality broadband reflectors and sensors. They also have potential for lab-on-chip type structures for surface science applications and also for micro-fluidic applications. We have fabricated single layer and double layer PCs out of single crystal silicon and incorporated these into scanners. We are currently working on fabricating waveguides and resonators with this process.

Gallium Phosphide Photonic Crystal Nanocavities in the Visible

Kelley Rivoire, Andrei Faraon, Jelena Vuckovic

Photonic crystal nanocavities at visible wavelengths are fabricated in a high refractive index (n>3.2) gallium phosphide membrane. The cavities are probed via a cross-polarized reflectivity measurement and show resonances at wavelengths as low as 645 nm at room temperature, with quality factors between 500 and 1700 for modes with volumes $0.7(\lambda/n)^3$. These structures could be employed for submicron scale optoelectronic devices in the visible, and for coupling to emitters with resonances in the visible such as nitrogen vacancy centers, and bio- and organic molecules.

Planar Lenses Based on Nano-Scale Slit Array in Metallic Film

Lieven Verslegers, Edward Barnard, Mark L. Brongersma, Peter B. Catrysse, Shanhui Fan, Justin S. White, Zongfu Yu,

We experimentally demonstrate and characterize planar lenses based on a nano-scale slit array in a metallic film. Our lens structures consist of optically thick gold films with micron-size arrays of closely-spaced, nano-scale slits of varying widths milled using a focused ion beam. We find excellent agreement between electromagnetic field simulations of the design and confocal measurements on manufactured structures. We provide guidelines for lens design and show how actual lens behavior deviates from simple theory.

C. MICROSCOPY AND MOLECULAR IMAGING

High-Speed, Miniaturized Fluorescence Microscopy in Freely Moving Mice
*Laurie D Burns, Benjamin A Flusberg, Axel Nimmerjahn, Eric D Cocker, Eran A Mukamel,
Robert P J Barretto, Tony H Ko, Juergen C Jung, Mark J Schnitzer*

A central goal in neuroscience is to explain animal behavior in terms of causal cellular processes. However, concurrent observation of mammalian behavior and underlying cellular dynamics has been a longstanding challenge. We developed a miniaturized fluorescence microscope (1.1 g) for brain imaging in freely behaving mammalian subjects. We designed our microscope for use in mice due to the wide availability of genetically manipulated mouse models for study of cognitive functions, animal behaviors, and nervous system disorders.
Our microscope uses gradient refractive-index microlenses, a fiber-optic bundle as an image guide, and a custom miniaturized gear box for axial focusing capability. We made two versions of the microlens objective: a shorter version for imaging of surface tissues and a longer version for minimally invasive imaging of deeper tissues. The fiber bundle rotates within an optical commutator, allowing the mouse to move without significant mechanical resistance. We computationally re-construct stable records of events at the brain by using the data from an optical encoder that tracks the bundle's rotation. With this approach we have visualized microcirculatory and neuronal calcium dynamics in freely moving mice at imaging frame rates up to 100 Hz. This capability opens wide possibilities for future studies of how cellular function in the brain varies across different behavioral and physiological states.

Application of Hardware-Based Anti-Brownian Electrokinetic Trap to Determine Single-Molecule ATP Stoichiometry in a Multi-Subunit Enzyme
Yan Jiang, Adam E. Cohen, Nick Douglas, Judith Frydman , and W. E. Moerner

The hardware-based Anti-Brownian ELectrokinetic trap (ABEL trap) features a feedback latency as short as 25 us, suitable for trapping single protein molecules in aqueous solution. Preliminary data are presented in which the trap is applied to the problem of determining the distribution of numbers of ATP bound for single chaperonin multi-subunit enzymes.

Bowtie Nanoantennas as Near-field Sources for Optical Imaging
Anika Kinkhabwala, W. E. Moerner

Bowtie Nanoantennas, which consist of two 70nm gold triangles, concentrate incident optical fields beyond the diffraction limit to an area above the triangular tips of their gap. These structures could be useful in single molecule fluorescence, Raman, or even absorption experiments, but placing molecules precisely in the region of enhanced fields is a tricky problem. By fabricating bowtie nanoantennas onto an AFM tip (BOAT), the bowtie can be scanned above a single molecule using standard AFM technology, allowing precise positioning with respect to the molecule of interest. This poster will discuss the fabrication and initial optical

characterization of tips fabricated using E-beam lithography and Focused Ion Beam (FIB) milling.

Towards Superresolution Biological Imaging Via STimulated Emission Depletion (STED) Microscopy
Lana Lau, Magnus Hsu, Marcelle Koenig, William Moerner

Despite the advancements brought about by near-field microscopy techniques, an overwhelming 80% of all biological microscopy studies are still conducted in the far-field with visible light. However, the resolution of these studies has been conventionally limited by diffraction. In the Moerner Lab, we have recently implemented a STimulated Emission Depletion (STED) microscope whose resolution breaks the diffraction barrier by optically engineering the microscope's point spread function. Current work will focus on superresolution imaging of biological samples.

Photoactivatable and Photoswitchable Single-Molecule Fluorophores: DCDHFs and More
Samuel J. Lord, Nicholas R. Conley, Hsiao-lu D. Lee, Na Liu, W. E. Moerner, Reichel Samuel, Robert J. Twieg

There is a continuing need for single-molecule fluorophores optimized for the cellular environment. Especially valuable are fluorophores with sophisticated photophysics for applications requiring additional facets of control, such as photoactivation or photoswitching. We have reengineered a red-emitting DCDHF fluorophore so that it is dark until photoactivated with a short burst of low-intensity violet light. Photoactivation of the dark fluorogen leads to conversion of an azide to an amine, which shifts the absorption to long wavelengths. After photoactivation, the fluorophore is bright and photostable enough to be imaged on the single-molecule level in living cells. This provides a new class of bright photoactivatable fluorophores, as are needed for super-resolution imaging schemes that require active control of single molecule emission. A Cy3-Cy5 covalent heterodimer with photoswitching capability will also be presented.

Implantable Optical Fluorescence Biosensors for Molecular Imaging
Thomas D. O'Sullivan, Adam de la Zerda, Sanjiv S. Gambhir, James S. Harris, Jr., Ofer Levi, Elizabeth Munro, Natesh Parashurama,

In vivo molecular imaging is a field which enhances understanding of cellular and molecular pathways and mechanisms of disease by visualizing and quantifying biological processes. The ability to image fluorescence, in particular, is a powerful tool considering the wealth of fluorescent probes/proteins that are used to visualize dynamic in vivo processes. Current approaches to detect fluorescence in vivo rely on devices which use broad area illumination and cooled CCD detectors, generally requiring anesthetized animal models. An alternative is to engineer miniaturized fluorescence sensors for direct implantation in freely-moving subjects.

In this study, we designed and fabricated an implantable, GaAs-based semiconductor fluorescence biosensor, which incorporates an un-cooled photodetector with a 675nm vertical-cavity surface-emitting laser (VCSEL) optimized for sensing fluorescent Cy5.5 dye. The sensor and collimating lens are encapsulated in a sealed package for implantable rodent studies. For filtering unwanted spectra, a combination of physical and spectral blocking layers yields >OD4 excitation rejection at the detector for 1.3mW VCSEL power. The sensor detects near-IR fluorescent Cy5.5 molecules in vitro at 100nM concentration (in a 100µL volume) and linearly for concentrations up to 6µM. In a preliminary in vivo study, subcutaneously injected dye (1µM Cy5.5 in 50µL) was detected.

In Vivo Cellular Imaging with MEMS Scanners

Hyejun Ra, Christopher Contag, Emilio Gonzalez, Roger Kaspar, Gordon Kino, Michael Mandella, Wibool Piyawttanametha, Olav Solgaard

Confocal microscopy can be used for observing in vivo biological function and behavior provided that the objectives and scanning mechanisms can be made sufficiently small for endoscopic imaging implementations. In order to achieve sub-cellular resolution of a few microns, conventional objectives with high numerical apertures (NA) and dimensions on the centimeter scale are typically used. However, a Dual-Axes Confocal (DAC) microscope architecture achieves high resolution imaging with low NA lenses within a small dimension. By using a MEMS (Microelectromechanical Systems) scanner in DAC microscopes, real time in vivo imaging can be realized. We have successfully demonstrated a two-dimensional gimbaled MEMS scanner in double silicon-on-insulator (SOI) layers actuated by electrostatic vertical combdrives. The device is integrated into a fully-packaged and portable handheld DAC microscope system. In vivo fluorescence imaging is performed with three-dimensional imaging capabilities in investigating siRNA silencing in the skin.

Superresolution Imaging in Live Caulobacter Crescentus Cells Using Photoswitchable Enhanced Yellow Fluorescent Protein

Michael A. Thompson, Julie S. Biteen, W. E. Moerner, Lucy Shapiro, Nicole K. Tselentis

Recently, the use of photoactivation or switching to control single-molecule fluorescent labels has yielded images of cellular structures beyond the optical diffraction limit ("superresolution"). While previous work in live cells utilized sophisticated photoactivatable fluorescent proteins, we show here that superresolution imaging can be performed with fusions to a commonly used fluorescent protein, EYFP. Rather than being photoactivated, however, EYFP can be reactivated with violet light after apparent photobleaching. After initial imaging, only a sparse subset is reactivated and localized in each imaging cycle. We image cell-cycle-dependent superstructures of the bacterial actin protein MreB in live C. crescentus cells with sub-40-nm resolution for the first time, showing that EYFP is a useful emitter for in vivo superresolution imaging of intracellular structures in bacterial cells.

One-Way Electromagnetic Waveguide Formed at the Interface between a Plasmonic Metal under a Static Magnetic Field and a Photonic Crystal
Zongfu Yu, Shanhui Fan, Georgios Veronis, Zheng Wang

D.   NEUROSCIENCE

Selective Retinal Photocoagulation with Microsecond Exposures Using a Continuous Line Scanning Laser
Yannis M. Paulus, Mark S. Blumenkranz, Ray F. Gariano, Atul Jain, Hiroyuki Nomoto, Daniel Palanker, Georg Schuele, Christopher Sramek

Retinal photocoagulation with microsecond pulses allows for selective targeting of the retinal pigmented epithelium (RPE) and photoreceptors. We achieve such selectivity using a line pattern scanning laser with a beam dwell time down to 15 microseconds. We evaluate the effects of scanning rate and laser power on spatial confinement and safety of photocoagulation, as well as healing of the retinal lesions.

A 532nm Nd:YAG scanning laser system (PASCAL™) with a beam diameter of 100 µm was applied to rabbit retinas in-vivo. Linear scanning velocity varied from 1.6 to 6.6 m/s, corresponding to dwell times from 15 to 60 microseconds. Retinal damage was assessed ophthalmoscopically, with fluorescein angiography, live-dead fluorescent assay, and histologically with a follow-up ranging from 1 hour to 2 months.

Histologic analysis showed initial damage of RPE and drop-out of photoreceptors at one day, followed by photoreceptor layer reorganization at 3-7 days. Continuity of the outer nuclear layer and RPE was largely restored by one week, and normal appearance of the photoreceptors was achieved by 1-2 months. No glial scarring was observed. The width of the safe therapeutic window and spatial selectivity of photocoagulation increased with decreasing dwell time and beam size.

E. SOLAR CELL

Solution-Processable Transparent Electrodes from Graphene Oxide
Hector A. Becerril, Zhenan Bao, Yongsheng Chen, Zunfeng Liu, Peter Peumans, Randall Stoltenberg, Junbo Wu

Transparent electrodes are key for technologies such as solar cells, light-emitting diodes, optical displays, etc. The low sheet resistance and high transparency of indium-tin oxide (ITO) have made it the electrode material of choice in previous years, but the rising cost of indium and its incompatibility with flexible substrates make ITO less desirable for future applications. Metal nanowire meshes (NM) and carbon-nanotube networks (CNTN) have been proposed as large-scale solution-processable transparent electrodes. We have explored the potential of reduced graphene oxide (RGO), a derivative of graphite, as an abundant, solution-processable,

transparent electrode material that offers a smoother surface than NM and CNTN, and could achieve graphene-like charge transport. RGO thin-films are easily deposited from aqueous dispersions, but these are electrically insulating, and must be deoxygenated to attain conductivity. We studied deposition, patterning and deoxygenation of RGO, and found conditions that give promising films with sheet resistances as low as 1Kohm/square and transmittances of ~80% over the 400 nm to 1800 nm spectral range. We fabricated RGO-based working organic solar cells with efficiencies ~60% of those achieved with ITO electrodes. Further optimization of deoxygenation process will give rise to highly conductive, flexible RGO transparent electrodes compatible with plastic substrates.

Effect of Alkyl Chains on Thin Film Morphology of Acenaphthylthienopyrazine Based Low Band-Gap Polymers

Rajib Mondal, Zhenan Bao, Hector A. Becerril, Alex C. Mayer, Michael D. McGehee, Nobuyuki Miyaki, Jack Parmer

Several acenaphthylthienopyrazine-fluorene (ACT-FL) co-polymers with different side chains are studied in organic thin film transistors (OTFTs) and bulk heterojunction solar cells. The alkyl chains in ACT and FL moieties strongly affect the thin film morphology and ultimately the device performances. Thin films are usually more crystalline when the alkyl chains are linear as indicated by AFM and grazing incidence X-ray diffraction (GIXD). Very high hole carrier mobility (~0.2 cm2/Vs) can be achieved in the OTFT devices using the polymer substituted with dodecyl groups. Introduction of branched alkyl chain, such as 2-ethylhexyl, in the similar polymer backbone makes the film amorphous and reduces the mobility in OTFT devices. Maximum power conversion efficiency (PCE) of 1.38% was achieved using these polymers.

F.   TELECOM

Nonlinear Impairment Compensation Using Digital Backpropagation

Ezra Ip, Prof. Joseph M. Kahn

Digital backpropagation (BP) is a universal technique that can jointly compensate for linear and nonlinear impairments in fiber. In this poster, we present simulation results for long-haul systems with inline dispersion compensation. We find that a receiver implementing BP with a step-size equal to a span length gives drastically better performance than linear equalization only, enabling the transmission of 21.4 Gb/s RZ-QPSK over 6,400 km of single-mode fiber.

G.   OTHER

Thermal Loading of Optical Resonators for Future Gravitational-Wave Detectors
Amber L. Bullington, Robert L. Byer

The Laser Interferometer Gravitational-wave Observatory (LIGO) with sites in Hanford, Washington and Livingston, Louisiana is part of a worldwide network of detectors actively searching for gravitational waves. The next-generation detectors for LIGO will employ an increase in laser power twenty times greater than the current generation of LIGO. As circulating power in the detector increases, detrimental thermal distortion of optics may affect interferometer performance. To test the impact of thermal loading in a resonator, a Fabry-Perot ring cavity is illuminated with high-power laser light to demonstrate the effects of thermal distortion of the cavity's optics. Higher-order modes frequency-degenerate with the fundamental mode, decreased power transmission, and thermally-induced power fluctuations contribute to the degradation of the performance of a thermally loaded resonator. From experimental observations, estimations of power handling limitations predict how resonators for future gravitational-wave detectors will perform.

RPE PPLN Waveguides for Parametric Temporal Imaging
Derek Chang, Carsten Langrock, Martin M. Fejer

A temporal imaging system can be used to slow down (or stretch) a waveform in time so that ultrashort optical pulses can be measured by conventional equipment. A key element in temporal imaging is the time lens which imparts a quadratic phase shift onto the waveform being imaged. We use parametric interactions in linearly chirped aperiodically poled lithium niobate waveguide devices to transfer quadratic phase from a linearly chirped pump pulse onto a signal waveform. In our current generation of devices, we design the bandwidth of the quasi-phasematched grating to pass the sum-frequency component and suppress the pump and signal second-harmonic components to improve the signal-to-noise ratio. In addition, we use the method of deleted domain reversal and nonlinear chirp apodization to minimize the passband ripple of the transfer function. Both apodization methods show a trade off between passband ripple size and roll-off sharpness yet maintain sufficient conversion efficiency for practical device implementations.

Single Photon Nonlinear Optics with Quantum Dots in Photonic Crystal Resonators
Andrei Faraon, Dirk Englund, Ilya Fushman, Pierre Petroff, Nick Stoltz, Jelena Vuckovic

A photonic crystal cavity with a strongly coupled quantum dot is coherently driven using short laser pulses. Depending on the driving frequency, photon blockade or photon induced tunneling is observed. In the case of photon blockade, a single photon trapped inside the cavity can block the transmission of subsequent photons. For photon-induced tunneling the reverse happens, a single trapped photon enhancing the probability of subsequent photons to tunnel through the

resonator. These phenomena enable a new class of logic devices based on optical non-linearities at the single photon level. Future photonic crystal devices of this kind will integrate nano-resonators with strongly coupled emitters, interconnected in a photonic network via photonic crystal waveguides. We took the first steps towards this goal and built integrated devices composed of waveguide-coupled cavities with local tuning and out-coupling capabilities. A singe quantum dot was used to control the transmission function of the device via dipole induced transparency. Future improvements of the device design will enable logic devices based on photon blockade and photon induced tunneling.

Transparent Ceramic for Optical Application at Stanford
Deschamps Guillaume, R.Byer, Romain Gaume, Ye He

Transparent ceramics have brought more and more interest than single-crystals in high power laser due to the advantages in ceramic fabrication techniques, such as reduced processing time, scaling to large aperture sizes and reduced fabrication temperatures. Here the fabrication of transparent Nd:YAG ceramics has been investigated and optimized by adjusting stoichiometry in mixing powder of Alumina and Yttria. Optical properties and microstructure have been measured to confirm a tolerant range of 0.1mol % stoichiometry shift. Ceramics in a good optical quality have been successfully produced in a appropriate fabrication process.

Excitation Transfer Studies of Phase Transition Kinetics
Alexei A. Goun, David B. Spry, Michael D. Fayer

We demonstrate the use of the fluorescent excitation transfer (FRET) technique for the measurements of the phase transition kinetics. The time scale of the initial stage of the phase separation was measured in the temperature jump pump, excitation transfer probe experiment.

Large Area High Reflectivity Broadband Photonic Crystal Mirror MEMS Scanner
Il Woong Jung, Shrestha Basu-Mallick, Olav Solgaard

We introduce a MEMS scanner with a monolithic silicon 2-D photonic crystal (PC) mirror with broad-band high reflectivity (>90%) in the 1550nm wavelength band. The photonic crystal is generated as an integrated part of the MEMS scanner fabrication process, resulting in a monolithic structure with a mirror that is ultra-flat over a large 500μm x 500μm aperture.

Dynamics of Synchronously Pumped Optical Parametric Oscillators Induced by Self-Phase Modulation
Joseph Schaar, Martin Fejer, Jason Pelc

We experimentally observe oscillations, with frequencies between 100 and 700 kHz, of the intracavity power of a singly resonant synchronously pumped optical parametric oscillator.

Numerical investigations show the oscillations are caused by the interaction of the parametric gain, group velocity mismatch between the interacting waves, and self-phase modulation of the resonant wave. A heuristic model based on periodic pulse reshaping describes the dependence of the oscillation frequency on the pump power, cavity losses, and cavity-length detuning. A comparison of the experimental, numerical, and modeling results is presented.

Complete Optical Control of a Single Electron Spin in a Quantum Dot
David Press, Thaddeus D. Ladd, Yoshihisa Yamamoto, Bingyang Zhang

We demonstrate complete coherent control over an initialized electron spin state using picosecond optical pulses. First we vary the intensity of a single optical rotation pulse to observe over six Rabi oscillations between the two spin-states. Next we apply two sequential pulses to observe high-contrast Ramsey interference. Such a two-pulse sequence is sufficient to realize an arbitrary single qubit gate completed on a picosecond timescale. Along with the spin initialization and final projective measurement of the spin state, these results demonstrate a complete set of all-optical single-qubit operations.

STANFORD PHOTONICS RESEARCH CENTER

2008 Student Profiles

Name:	Onur Akkaya
Address:	E.L. Ginzton Laboratory, Electrical Engineering Department, Stanford University
Email:	ocakkaya@stanford.edu
Office Phone:	650.521.7324
Date of Birth:	04/30/1984
Citizenship:	Turkey

Degrees Conferred

Master of Science in Electrical Engineering, Stanford University, June 2008.
Bachelor of Science in Electrical and Electronics Engineering, Middle East Technical University, June 2006.

Candidate for Ph.D.

Electrical Engineering Department
Date expected: June 2011

Research Supervisor

Professor Olav Solgaard

Current Research

Fiber-Optics Sensor Networks
Novel Fiber-Optic Sensors

Experience

06/07–present: Research assistant at Electrical Engineering Department, Stanford University under Prof. Olav Solgaard.

- Developed architectures for multiplexing large numbers of fiber-optic sensors with an enhanced signal-to-noise ratio performance
- Involved in processing of high-sensitivity optical pressure sensors at Stanford Nanofabrication Facility

06/05-07/05: Summer intern at ASELSAN INC., Ankara, Microelectronics, Guidance and Electro Optics Division, Electronic System Design Directorate

06/04-07/04: Summer intern at TUBITAK BILTEN (The Scientific & Technical Research Council of Turkey / Information Technologies and Electronics Research Institute), Ankara, Electronic System Design Group

Name: Amber L. Bullington

Address: Ginzton Laboratory, 450 Via Palou, Stanford, CA 94305

Email: abull@stanford.edu

Office Phone: (650) 723-0246

Date of Birth:

Citizenship: USA

Degrees Conferred

Master of Science in Electrical Engineering, Stanford University, April 2003.
Bachelor of Science in Electrical Engineering, Cornell University, May 2001.

Candidate for Ph.D.

Electrical Engineering Department
Date expected: Fall 2008

Research Supervisor

Professor Robert L. Byer

Current Research

Experimental testing of table-top ring cavities under high power laser illumination with simulated predictions of future configurations for the Laser Interferometer Gravitational-wave Observatory (LIGO).

Experience

01/02 – present: Research assistant at Stanford University under Prof. Robert L. Byer. Studies of high power interferometry for the Laser Interferometer Gravitational-wave Observatory (LIGO).

03/03 – present: Science Monitor for LIGO during scientific data collection sessions.

06/02 – 08/02: Summer intern at LIGO. Utilization of test mass butterfly modes for inferometer alignment.

05/00 – 08/00: Summer intern at Celeritek, Inc. Process engineer improving manufacturing of GaAs ICs for high frequency applications.

06/99 – 05/00: Undergraduate researcher at Cornell University under Professor Norman Tien. A MEMS raster scanning mirror for a projection display.

Name: Laurie Burns

Address: Clark Center W080
                 318 Campus Drive West
                 Stanford, CA 94305-5435

Email: ldburns@stanford.edu

Office Phone: (650) 725-4097

Degrees Conferred

Bachelor of Science in Physics, Massachusetts Institute of Technology, 2006

Candidate for Ph.D.

Dept. of Applied Physics
Date expected: December 2011

Research Supervisor

Professor Mark Schnitzer (Applied Physics and Biology)

Current Research

Instrumental design for and experiments with portable microscopy using fiber optics and miniaturized optics for imaging in awake, freely moving animals.

Experience

01/2003-08/2003: Undergraduate research at MIT with Professor Min-Chang Lee, Plasma Science and Fusion Center. Studied plasma physics and attended a summer program at University of Alaska, Fairbanks for field experiments.

05/2005-06/2006: Undergraduate thesis research at MIT with Professor Bernd Surrow, Laboratory of Nuclear Science. Built and tested a triple-GEM (Gas Electron Multiplier) prototype detector. Wrote undergraduate thesis for Physics degree.

09/2006-12/2006: Research rotation at Stanford with Professor Shanhui Fan and Dr. Michel Digonnet, Dept. of Applied Physics. Worked on Faraday rotation effects in fiber optics.

01/2007-present: Doctoral research at Stanford with Professor Mark Schnitzer, Depts. of Applied Physics and Biology. Development and use of portable, miniaturized microscopes for imaging in awake, freely moving animals.

Name: Derek Chang

Address: Edward L. Ginzton Lab Box S-22
Stanford University
Stanford, CA 94305-4088

Email: dchang00@stanford.edu

Office Phone: (650) 723-1718

Degrees Conferred

Master of Science in Electrical Engineering, Stanford University, June 2008
Bachelor of Science in Electrical Engineering, California Institute of Technology, June 2006

Candidate for Ph.D.

Electrical Engineering
Date expected: 2012

Research Supervisor

Professor Martin M. Fejer

Current Research

Design, fabrication, and characterization of reverse proton exchange (RPE) periodically poled lithium niobate (PPLN) waveguide devices for parametric temporal imaging.

Experience

06/2007 – Present	Research assistant at Stanford Univerity under Professor Martin M. Fejer
	Described above under current research.
06/2004 – 09/2006	Undergraduate researcher at Caltech under Professor Amnon Yariv
	- *Designed and analyzed circular bragg resonators with different geometries using finite difference time domain (FDTD) simulations The goal was to maximize the quality factor by adjusting device parameters.*
	- *Measured and characterized fabricated devices.*
06/2003 – 09/2003	Technical intern at Rockwell Scientific under Dr. Gregory Provan
	- *Bayesian network modeling of the Boeing 767 electrical system*
	- *Helped develop wireless network trangulation methods for ground based positioning systems.*
06/2002 – 09/2002	Technical intern at Rockwell Scientific under Dr. Gregory Provan
	- *Developed software for bayesian network modeling*
	- *Developed Java file format converter*
06/2001 – 09/2001	Technical intern at Rockwell Scientific under Dr. Jeffrey Cheung
	- *Created ceramic samples and grew large film samples*
	- *Determined film thickness and uniformity as well as performed radio frequency attenuation measurements.*

Name: Alexei Goun

Address: 126 Blackwelder Court, apt 1104, Stanford, CA 94305

Email: agoun@stanford.edu

Office Phone: (650)704-7410

Date of Birth: November, 12 1976

Citizenship: Russian

Degrees Conferred

Bachelor of Science, Applied Mathematics and Mechanics

Master of Optical Science and Engineering, CREOL/University of Central Florida

Candidate for Ph.D.

Graduating Summer 2008

Research Supervisor

Dr. Michael D. Fayer, Chemistry Department

Current Research

Spectroscopic studies of the kinetics of Phase Separation.

Experience

Optical Design, Image Processing, Ultrafast Laser Systems.

Name:	Ye He
Address:	94 Thoburn Ct, Apt 101, Stanford, CA94305
Email:	yehe@stanford.edu
Office Phone:	650-723-1668
Date of Birth:	Optional
Citizenship:	China

Degrees Conferred

Bachelor of Science in Physics, University of Science and Technology of China, Hefei, June 2006.

Candidate for Ph.D.

Department: Applied Physics
Date expected: September 2011

Research Supervisor

Professor R.Byer

Current Research

Transparent Ceramic on high power laser

Experience

06/08-now: Research assistant at Stanford University under Prof. R. Byer. Fabricate transparent rare earth doped YAG ceramics for laser application and characterize them.

09/07-06/08: Research assistant at Stanford University under Prof. R. Feigelson. Prepare single crystal and ceramic material for scintllator application and try to study non-proportionality mechanism.

04/07-09/07: Research assistant at Stanford University under Prof. Shanhui Fan and Dr. Michel Digonnet. Measure the Verdet constant for Photonic Band-gap fiber resulting from Faraday Effect, simulate the experiment in computer, and compare the results to figure out the polarization properties of PBF.

01/07-04/07: Research assistant at Stanford University under Prof. Ian Fisher. Prepare rare earth telluride and measure the resistivity using SQUID and Hall coefficient using PPMS. Try to identify the transition temperature for Charge Density Wave (CDW). Measure the angle resolved magnetic resistivity of HoTe3 in low temperature.

10/06-01/07: Research assistant at Stanford University under Prof. Beasley. Use XPS to analyze the property of SiC and grapheme and try to prepare epitaxial graphene on SiC surface.

12/05-06/06: Achieve Undergraduate Thesis in the ZnO Lab Group, Physics Department, USTC leaded by Prof. Zhuxi Fu.

Name:	Ezra Ip
Address:	366 Packard Building, 350 Serra Mall, Stanford, CA 94305-9515
Email:	wavelet@stanford.edu
Office Phone:	650-283-5044
Date of Birth:	3/27/81
Citizenship:	New Zealand

Degrees Conferred

M.S. in Electrical Engineering, Stanford University, June 2004.
B.E. (Hons), University of Canterbury, Christchurch, New Zealand, April 2001.

Candidate for Ph.D.

Department of Electrical Engineering, Stanford University
Date expected: December 2008

Research Supervisor

Professor Joseph M. Kahn

Current Research

Fiber optic communications, free space communications, digital signal processing, nonlinear optics

Experience

06/03–present: Research assistant at Stanford University under Prof. Joseph. M. Kahn. Studied coherent detection and digital signal processing techniques for compensating impairments in single-mode fiber. Topics included laser phase noise mitigation using feedforward carrier recovery and phase locked loops; chromatic dispersion and polarization mode compensation using fractionally spaced linear equalizers; and nonlinear compensation using digital backpropagation. Constructed a 4.976 Gb/s QPSK heterodyne receiver. Set up a fiber re-circulating loop for long-haul experiments. Studied parametric wavelength conversion using a singly resonant optical parametric oscillator, and demonstrated the world's first free-space mid-infrared coherent QPSK link.

06/08–08/08:   Instructor for EE102B (Signal Processing and Linear Systems II) at Stanford University.

06/05–09/05:   Summer intern at NEC Labs America. Studied advanced modulation formats for 40 Gb/s long-haul transmission. Performed system modeling and simulation using VPI.

11/00–09/01:   Research Engineer at Industrial Research Ltd. Studied MIMO systems for wireless communications. Collaborated in hardware implementation of MIMO.

02/00–11/00:   Final Year Project at University of Canterbury. Implemented an OFDM wireline system on DSP.

Name:	Jae-Woong Jeong

Address:	E. L. Ginzton Laboratory, 41-C
	450 Via Palou
	Stanford, CA 94305

Email:	jjeong1@stanford.edu

Office Phone:	(650) 723-1992

Citizenship:	Republic of Korea

Degrees Conferred

Master of Science in Electrical Engineering, Stanford University, June 2008.
Bachelor of Science in Electrical Engineering, the University of Texas, Austin, May 2005.

Candidate for Ph.D.

Electrical Engineering
Date expected: 2012

Research Supervisor

Professor Olav Solgaard

Current Research

Design, fabrication, and characterization of tunable optical bandpass filters using electrostatic combdrive actuators.

Experience

10/07–present: Research assistant at Stanford University under Prof. Olav Solgaard. Research on MEMS optical filters with tunable center wavelength and passband.

01/06-03/06: Intern at LG Micron Research Center, Anyang, Korea. Study and characterization of display brilliance enhancement films for LCD backlight unit.

10/03-08/04: Research assistant at the University of Texas at Austin under Prof. Rebecca Richards-Kortum. Research on fiber-optic confocal reflectance microscopy for early cancer detection.

Name:	Yan Jiang
Address:	Chemistry Stauffer II Room 11A, 375 N-S Axis, Stanford, CA 94305
Email:	yanjiang@stanford.edu
Office Phone:	(650)724-4052
Date of Birth:	05/25/1986
Citizenship:	PR China

Degrees Conferred

Bachelor of Science in Fundamental Sciences (Physics and Mathematics), Tsinghua University, Beijing, PR China, Jul 2006.

Candidate for Ph.D.

Department: Applied Physics

Date expected: Jun 2012

Research Supervisor

Professor W.E. Moerner

Current Research

Trapping and manipulating individual molecules: We recently developed an Anti-Brownian ELectrokinectic (ABEL) trap, which uses fluorescence detection, electrokinetic forces and real-time feedback to trap and manipulate individual molecules in solution. We are now trapping single chaperonin/ATP-Cy3/BeFx complexes and counting the number of the ATPs on each chaperonin. We are also trying to improve the controlling scheme of the feedback loop and the fabrication of microfluidic device in order to obtain better trapping performance.

Experience

01/07–present: Research assistant at Stanford University under Prof. Moerner. With the newly developed ABEL trap, we are trapping chaperonin/ATP-Cy3/BeFx complexes and counting the number of the ATPs on each chaperonin.

10/06-12/06: Research assistant at Stanford Linear Accelerator Center under Prof. Su. I searched for 2-dimensional ansatz of parameters for the parameterized simulation of Electromagnetic Shower in the calorimeter of ATLAS detector.

05/04-07/06: Research assistant at Laboratory of Soft Matter Physics, Institute of Physics, Chinese Academy of Sciences. I assisted in setting up single molecule mechanical manipulation equipment, including micropipette and magnetic tweezers. I also analyze and improved a geometric model of DNA spool condensation and decondensation through a method of free energy reconstruction and medium level of simulation.

Name:	**Il Woong Jung**

Address: Ginzton Labs 450 Via Palou Rm. 50

Email: iwjung@stanford.edu

Office Phone: 650-723-9659

Date of Birth: 01/07/75

Citizenship: Republic of Korea

Degrees Conferred:
Doctor of Philosophy in Electrical Engineering, Stanford University, June 2007.
Master of Science in Electrical Engineering, Stanford University, Dec 2003.
Master of Science in Physics and App. Phys., Yonsei University, Aug 2001.
Bachelor of Science in Physics and App. Phys., Yonsei University, Feb 1997.

Current Position
Research Associate in Electrical Engineering

Research Supervisor:
Professor Olav Solgaard

Current Research:
Monolithic silicon photonic crystal MEMS devices

Experience:
06/07 – present
Postdoctoral Scholar/Research Associate at Stanford University under Prof. Olav Solgaard. Photonic crystal MEMS devices and Spatial Light Modulators for optical maskless lithography

09/01 - 06/07
Research assistant at Stanford University under Prof. Olav Solgaard. Development of MEMS deformable micromirror arrays for applications in coherent free-space communication and adaptive optics. Development of MEMS spatial light modulators for applications in maskless lithography.

03/97 - 02/98, 03/00 – 08/01
Research assistant at Yonsei University under Prof. Hangnam Ok.
Crystal structure and magnetic property study by Mossbauer spectroscopy of lithium ferrites.

Name: Sukru Ekin Kocabas

Address: Edward L. Ginzton Laboratory, Box N-145,
                    Stanford University, Stanford, CA, 94305 – 4088

Email: kocabas@stanford.edu

Office Phone: (650)725-2291

Degrees Conferred
Master of Science in Electrical Engineering, Stanford University, 2004.
Bachelor of Science in Electrical Engineering, Bilkent University, Ankara, Turkey, 2002.

Candidate for Ph.D.
Major – Electrical Engineering, Minor – Physics,
Date expected: March, 2009

Research Supervisor
Prof. David A.B. Miller

Current Research
Plasmonics
Nano-fabrication of optical detectors incorporating antennas for light
Modeling of the propagation and scattering of light

Name:	Lana Lau
Address:	Stanford Department of Chemistry Stanford University 333 Campus Drive Stanford, CA 94305
Email:	lana@stanford.edu
Office Phone:	650-724-4052
Date of Birth:	Aug. 15, 1983
Citizenship:	U.S.A.

Degrees Conferred

Bachelor of Science in Chemistry, University of California, Berkeley, May 2005.

Candidate for Ph.D.

Chemistry Department
Date expected: June 2011

Research Supervisor

Professor William E. Moerner

Current Research

Microscopy Imaging: Currently implementing a superresolution microscope for biological imaging.

Experience

09/06–present:	Graduate research assistant at Stanford University under Prof. William Moerner. Research involves implementing superresolution microscopy techniques to biological imaging.
11/05-05/06:	Research assistant at Chinese University of Hong Kong under Dr. Bo Zheng. Research involved applying microfluidic techniques to design microwell arrays for biochemical assays.
06/04-07/05:	Research assistant at University of California, Berkeley under Prof. Stephen Leone. Studies involved observing fundamental chemical reaction dynamics, specifically vibrational wavepacket dynamics of diatomic and polyatomic molecules.
06/02-06/03:	Research assistant at the University of California, Berkeley under Prof. Jean Frechet. Studies involved designing microparticles with controlled degradation for drug delivery and vaccine development.

Name:	Wah Tung, Lau
Address:	PO Box, 16885, Stanford, CA 94309
Email:	wlau@stanford.edu
Office Phone:	650-387-9445
Citizenship:	Hong Kong (China)

Degrees Conferred

Master of Science in Electrical Engineering, Stanford University, June 2001.

Bachelor of Engineering in Electrical and Electronic Engineering, The University of Hong Kong, June 1999.

Candidate for Ph.D.

Department of Electrical Engineering, (Date expected: 2009).

PhD Minor at Physics Department (Conferred).

Research Supervisor

Professor Shanhui Fan

Current Research

Manipulation of Thermal Electromagnetic Fields of Nano-Photonics devices

Experience

09/01–present: Research assistant at Stanford University under Professor Shanhui Fan

We performed theoretical studies and numerical simulations on diverse areas in nanophotonics: We had come out with a design procedure for single-mode, large bandwidth nano-waveguides using photonic crystals. Another project was to investigate the spatial coherence of thermal electromagnetic fields in the near-field regime of dielectric thin films. Currently, we are looking at the thermal-radiative properties of various nano-devices.

05/01-09/01: Research assistant at Stanford Linear Accelerator Center under Professor Martin Perl

To help improve an existing experiment that searched for freely existing fractionally charged elementary particle that is unknown to the Standard Model, by carefully examining the deflection of liquid micro-droplets in a chamber of large electric field.

06/00-09/00: Summer intern at Philips Semiconductor, Albuquerque, New Mexico

Worked as an engineer in the quality-control unit. The main duty was to design testing procedure for quality control of semiconductor electronic devices.

06/98 – 08/98 Exchanged student at the Department of Automation, Tsinghua University, Beijing, China

Develop website for a model industrial enterprise in China.

Name:	Meredith M. Lee
Address:	Center for Integrated Systems, 420 Via Ortega, Stanford, CA 94305
Email:	mmlee@stanford.edu
Office Phone:	650-868-5826
Date of Birth:	12/22/1981
Citizenship:	USA

Degrees Conferred

Master of Science in Electrical Engineering, Stanford University, June 2005.
Bachelor of Science in Electrical Engineering, Stanford University, June 2004.

Candidate for Ph.D.

Electrical Engineering
Date expected: 2009. NSF Graduate Fellow and NDSEG Fellow.

Research Supervisor

Professor James S. Harris and Professor Shanhui Fan

Current Research

Design, simulation, fabrication, and characterization of a 2D photonic crystal slab resonance-based index-of-refraction sensor for lab-on-a-chip applications.

Experience

06/05–08/05: **Optical Communications Intern at MIT Lincoln Laboratory, Lexington, MA.** Investigated the fiber fuse phenomenon in polarization-maintaining fibers at 1.55μm for free-space optical links. Designed experiments to measure power density threshold, fuse propagation velocity. Utilized FEMLAB for multi-physics numerical analysis.

06/04–09/04: **Test Technology Development Intern at Intel Corporation, Hillsboro, OR.** Designed benchtop electrical tester to detect thermo-mechanical defects in CPU package interconnects. Implemented standalone system exceeding sensitivity criteria for Pentium 4 defect detection.

03/04–06/04: **Research Assistant at Stanford University** under Professors Shanhui Fan, Martin Fejer and James S. Harris. Worked on design and fabrication of tightly confining AlGaAs waveguides and microcavities for all-optical switching. Utilized Fabry-Perot resonance and a variant of the cut-back method to determine propagation loss and characterize fabricated waveguides.

6/03–9/03: **Microelectronics Intern at IBM T. J. Watson Research Center, Yorktown Heights, NY.** Investigated DI/High Concentration Ozone techniques for processing Si, Ge. Analyzed oxide growth, surface roughness, wet etching, organic film removal, and gate oxide integrity.

6/02–9/02: **Photonics Intern at Agilent Laboratories, Palo Alto, CA.** Designed and built optical reflectance in-situ monitor for epitaxial crystal growth reactor (MOCVD).

Name: Samuel J. Lord

Address: Department of Chemistry, MC 5080 mailbox 99, Stanford, CA 94305-5080

Email: sjlord@stanford.edu

Office Phone: (650) 724–4052

Degrees Conferred

Bachelor of Science in Chemistry, University of North Carolina at Chapel Hill, 2004.

Candidate for Ph.D.

Chemistry, Chemical Physics
Date expected: 2010

Research Supervisor

Professor W. E. Moerner

Current Research

Single-molecule spectroscopy and fluorophore design.

Experience

2004–present: Research assistant at Stanford University under Professor W. E. Moerner. Designing and analyzing novel fluorophores (in close collaboration with a synthetic lab); carefully quantifying single-molecule and bulk photophysics of fluorophores.

2003: Summer REU through CPIMA at Stanford University, under Professors Eric Shaqfeh and Steven Chu. Studied single strands of DNA in concentrated/entangled solutions.

2002–2004: Undergrad research at University of North Carolina at Chapel Hill under Professor Sergei Sheiko. Used atomic-force microscopy to study polymer physics.

Name:	Dany-Sebastien Ly-Gagnon
Address:	450 Via Palou, Box N-135, Stanford, CA 94305
Email:	dalyx@stanford.edu
Office Phone:	(650) 725-2291

Degrees Conferred

M.S. in Electrical Engineering, University of Tokyo, Japan, October 2004.
B.S. in Electrical Engineering, Ecole Polytechnique of Montreal, Canada, May 2002.

Candidate for Ph.D.

Ph.D. Candidate in Electrical Engineering
Date expected: December 2010

Research Supervisor

Prof. David A.B. Miller

Current Research

Nanometallic-enhanced integrated photodetectors.

Experience

04/06–present: Research assistant at Stanford University under Prof. David A.B. Miller.

Performed research in integrated photonics for optical interconnects using nanometallic-enhanced devices.

03/05-09/05: ASIC engineer intern at Force10 Networks.

Developed integrated circuits & testbenches for high-speed routers.

10/02-12/04: Research assistant at University of Tokyo under Professor Kazuro Kikuchi.

Performed research in coherent detection and digital signal processing for optical fiber telecommunication networks.

05/02-09/02: Architectural verification intern at Procket Networks.

Developed software models of the integrated circuits to explore architectural issues of the system.

Name:	Thomas D. O'Sullivan
Address:	Center for Integrated Systems
	Department of Electrical Engineering
	420 Via Palou CISX-B113
	Stanford, CA 94305-4075
Email:	tdo@stanford.edu
Web:	**http://snow.stanford.edu/~tdo/**
Office Phone:	650-725-6970
Citizenship:	USA

Degrees Conferred

Master of Science in Electrical Engineering, Stanford University, June 2007.

Bachelor of Science in Electrical Engineering, Northwestern University, June 2005.

Candidate for Ph.D.

Department of Electrical Engineering

Date expected: June 2010

Research Supervisor

Professor James S. Harris

Current Research

Design and fabrication of implantable, integrated optical sensors (VCSEL/detector/optical filters) for *in vivo* molecular imaging based on fluorescence and Raman modalities

Experience

09/06–present: Research assistant at Stanford University under Prof. J.S. Harris. (see current research)

06/06-08/06: Summer research assistant and graduate fellow, US Department of Homeland Security Transportation Security Laboratory (TSL). Command, Control, Communications, Computers, and Intelligence (C4I) Laboratory Intern; research related to transportation security checkpoint technologies.

12/02-06/05: Research assistant at Northwestern University under Prof. M. Razeghi. Material growth and fabrication of high detectivity GaAs-based quantum dot infrared photodetector (QDIP) and quantum well infrared photodetector (QWIP) and focal plane arrays.

06/04-08/04: Summer research assistant at the Idaho National Laboratory, National Security Division. Unmanned aerial vehicle (UAV) team member; assisted with the design, production, and operation of autonomous unmanned aerial vehicles.

| **Name:** | Jason S. Pelc |
| | |

Address:	Dept. of Applied Physics
	E. L. Ginzton Laboratory
	450 Via Palou
	Stanford, CA 94305

Email: jpelc@stanford.edu

Office Phone: (650) 723-1718

Date of Birth: February 8, 1984

Citizenship: USA

Degrees Conferred

Master of Science in Applied Physics, Stanford University, June 2008.
Bachelor of Science in Physics with Electrical Engineering, Mass. Institute of Technology, June 2006.

Candidate for Ph.D.

Department of Applied Physics
Date expected: June 2011

Research Supervisor

Professor Martin M. Fejer

Current Research

Design and fabrication of waveguide nonlinear optical devices in periodically poled lithium niobate for single photon detection, quantum communication, and quantum computing. Theory and modeling of synchronously pumped optical parametric oscillators.

Experience

04/07-present:	Research assistant at Stanford University under Prof. M. M. Fejer. Theory, modeling, and fabrication of nonlinear optical devices.
09/05-06/06:	Research assistant at MIT under Prof. N. Mavalvala. Investigated radiation pressure effects in high-finesse optical cavities for generation of squeezed light.
05/04-08/04:	Research intern at GE Global Research, Niskayuna, NY under C. J. Hardy. Simulation, fabrication, and testing of novel rf receiver array design for multicoil MRI systems.

Name:	Hyejun Ra
Address:	Department of Electrical Engineering, Stanford University
	E. L. Ginzton Laboratory, 41-C
	450 Via Palou
	Stanford, CA 94305
Email:	hra@stanford.edu
Office Phone:	(650) 723-1992
Citizenship:	Republic of Korea

Degrees Conferred

Master of Science in Electrical Engineering, Stanford University, April 2004.

Bachelor of Science in Electrical Engineering, Seoul National University, Feb. 2001.

Candidate for Ph.D.

Department of Electrical Engineering

Date expected: January 2009

Research Supervisor

Professor Olav Solgaard

Current Research

- Performed research on MEMS optical scanners for free space communication and *in vivo* cellular imaging.

- Designed and implemented the 2-D endoscopic MEMS scanner for dual-axes confocal microscopy.

- Developed an optical benchtop prototype for imaging with the MEMS device.

- Assembled and packaged system into a miniaturized dual-axes confocal handheld probe, capable of 3-D imaging in both reflectance and fluorescence modes.

- Conducting *in vivo* small animal imaging with the miniaturized dual-axes confocal microscope system.

Experience

10/02 – present:	Research assistant at Stanford University under Prof. Olav Solgaard. Research on biomedical imaging with optical MEMS scanners.
09/03 – 12/03:	Teaching assistant for graduate level 'Photonics Laboratory' at Stanford University.
04/07 – 06/07:	Teaching assistant for undergraduate level 'Photonics Laboratory' at Stanford University.

Name:	Kelley Rivoire

Address:	Ginzton Lab GL 53
	450 Via Palou
	Stanford, CA 94305

Email:	krivoire@stanford.edu

Office Phone:	650-723-2279

Date of Birth:	5/24/1984

Citizenship:	USA

Degrees Conferred

Bachelor of Science in Physics, Massachusetts Institute of Technology, June 2006.

Candidate for Ph.D.

Electrical Engineering
Date expected: December 2012

Research Supervisor

Professor Jelena Vuckovic

Current Research

Visible nanophotonic devices using photonic crystals

Experience

3/07–present: Research assistant at Stanford University under Prof. Jelena Vuckovic. Research in photonic crystal devices

02/05-05/06: Undergraduate research at MIT under Prof. Marc Baldo. Fabricated and characterized organic LEDs with enhanced efficiency due to mixing of exciton spin states

6/02-8/02, 6/03-8/03: Summer research student in Center for Biomedical Engineering at M.D. Cancer Center in Houston, TX. Performed statistical analyses of data from studies intended to

determine whether spectroscopy can serve as an effective real-time diagnostic tool for cervical cancer

Name:	Joseph E. Schaar
Address:	Stanford University (Electrical Engineering)
	Stanford, CA 94305
Email:	jschaar@stanford.edu
Office Phone:	650-723-1718
Citizenship:	United States of America

Degrees Conferred

Master of Science in Electrical Engineering, Stanford University, March 2005.
Bachelor of Science in Electrical Engineering, University of Arizona, May 2003.

Candidate for Ph.D.

Electrical Engineering, graduation date expected: June 2009

Research Supervisor

Professor Martin M. Fejer

Current Research

THz wave generation in gallium arsenide using resonantly enhanced difference frequency generation in synchronously pumped optical parametric oscillators (SPOPO). Numerical simulation of SPOPOs using numerical integration of coupled-wave equations, and simulation of optical cavity eigenmodes in the presence of higher-order nonlinearities. Design of negative feedback control system to frequency stabilize doubly resonant SPOPOs. Investigation of SPOPOs with Kerr-induced non-stationary dynamics.

Experience

01/05–present:

Graduate research assistant at Stanford University working with Prof. Martin M. Fejer and Dr. Konstantin L. Vodopyanov.

05/03-09/03 & 06/04-09/04:

Summer internships at Raytheon Systems Company, Tucson, AZ. Design of switching power supplies for X-Band transmitters as well simulations of electromagnetic resonances in single-walled carbon nanotubes.

05/02-05/03:

Internship at National Semiconductor, Tucson, AZ. Design and study of analog switching power supply topologies and their applications to PC and RAM industries.

06/00-08/00:

Internship at Microchip Technology, Chandler, AZ. Design of microcontroller applications for automotive safety control systems.

Name: Michael Thompson

Address: Department of Chemistry
375 N-S AXIS STAUFFER 2 Rm 11B
Stanford , CA 94305

Email: mathomps@stanford.edu

Office Phone: (650) 724-4052

Date of Birth: 1/17/1985

Citizenship: USA

Degrees Conferred

Bachelor of Science in Chemistry, University of California, Irvine, June 2007.

Candidate for Ph.D.

Chemistry
Date expected: June 2012

Research Supervisor

Professor W. E. Moerner

Current Research

Superresolution imaging: using the emission from single molecules to achieve sub-diffraction limit fluorescence imaging in three dimensions in biological systems.

Experience

08/07–present: Research assistant at Stanford University under Prof. Moerner. Superresolution microscopy using single molecules.

06/04-06/07:   Undergraduate research assistant at UC Irvine under Prof. Reginald Penner. Synthesis and characterization of metal nanowires using electrochemical methods.

Name:	Lieven Verslegers

Address: Department of Electrical Engineering, Ginzton Laboratory, Room 41J

Email: lievenv@stanford.edu

Office Phone: 6502937002

Date of Birth: 16 April 1983

Citizenship: Belgium

<u>Degrees Conferred</u>

MS in Electrical Engineering, Ghent University, July 2006.
BS in Electrical Engineering, Ghent University, July 2004.

<u>Candidate for Ph.D.</u>

Department of Electrical Engineering
Date expected: December 2011

<u>Research Supervisor</u>

Professor Shanhui Fan

<u>Current Research</u>

Nanophotonics - plasmonic lenses

<u>Experience</u>

01/08–present: Research assistant at Stanford University under Prof. Shanhui Fan.
                 Nanophotonics - plasmonic lenses.
01/07-12/07:   Research assistant at Stanford University under Prof. Peter Peumans.
                 Organic photovoltaics - near-infrared absorbers.
10/05-06/06:   Research assistant at Ecole Nationale Supérieure des Télécommunications under Prof. Maurice Gagnaire.
                 Ethernet passive optical networks - packet delay analysis.
08/05-09/05:   Summer intern at Telenet Mechelen.
                 Optical access networks - feasibility study.
07/04-07/04:   Summer intern at Molex Slovakia.
                 Pressure sensors - quality control.

Name: **Samuel Wong**

Address: Ginzton Laboratory, 450 Via Palou, Stanford, CA 94305

Email: stwong@stanford.edu

Office Phone: (650) 725-2281

Citizenship: USA

Degrees Conferred:
  Master of Engineering in Electrical Engineering and Computer Science
  Massachusetts Institute of Technology, June 2001.
  Bachelor of Science in Electrical Engineering
  Massachusetts Institute of Technology, June 2001.

Candidate for Ph.D.
  Doctor of Philosophy in Electrical Engineering, September 2008 (expected)

Research Supervisor:
  Professor Robert Byer

Current Research:
  Development of frequency comb generators using self-phase-locked degenerate femtosecond
  synchronously pumped optical parameter oscillators.

  Investigation of efficient power-scaleable ultrafast lasers using mode-locking and phase-
  locking techniques and exploration of ceramic materials.

Experience:
  10/01 – present:
  Research assistant at Stanford University under Prof. Byer. Working on mode-locked solid-
  state lasers and nonlinear optics.

  07/01- 09/01:
  Optical engineer at Phaethon Communications. Worked on dispersion compensation in
  optical fiber communications.

  06/00 - 06/01:
  Research assistant at Massachusetts Institute of Technology under Professor Haus. Worked
  on dispersion-managed solitons in optical fiber.

  06/99 - 05/00:
  Lab assistant at MIT Lincoln Laboratory. Worked on fiber lasers, dispersion properties in
  optical fiber, and semiconductor mode-locked lasers.

Name:	Zongfu Yu
Address:	Department of Applied Physics, Stanford, CA
Email:	zfyu@stanford.edu
Office Phone:	Not Available
Date of Birth:	Not Available
Citizenship:	Not Available

Degrees Conferred

Bachelor of Science in Physics, University of Science and Technology , Hefei, China, June 2004.

Candidate for Ph.D.

Department of Applied Physics
Date expected: June 2009

Research Supervisor

Prof. Shanhui Fan

Current Research

Plasmonic devices including plasmonic switching device, metallic plasmonic lens and photodetectors enhanced by surface plasmons.

Nonreciprocal optics and its application for integrated optical isolators and circulators.

Dynamic photonic devices, modulated silicon devices for dynamic control of light, applications including tunable optical delay, optical packet switching, and optical isolation.

Numerical method for nanophotonic simulation, finite difference time domain and frequency domain.

Experience

09/04–present: Research Assistant at Stanford University

Name:	Qiang Zhang
Address:	E. L. Ginzton Laboratory 25B, Stanford, CA, 94305
Email:	qiangzh@stanford.edu
Office Phone:	650-723-3003
Date of Birth:	Dec. 10th, 1979
Citizenship:	China

Degrees Conferred

Ph. D. of Science in Physics, University of Science and Technology of China, July 2006.
Bachelor of Science in Physics, University of Science and Technology of China, July 2001.

Research Supervisor

Yoshihisa Yamamoto

Current Research

Quantum Cryptography, Quantum Optics

Experience

04/08-present: Researcher at National Institute of Informatic, Japan under Prof. Yoshihisa Yamamoto. Quantum Repeater based on semiconductor.
09/06-present: Post-doctoral researcher at Stanford University under Prof. Yoshisa Yamamoto. Quantum Cryptography over fiber link.
06/07-07/07: Visiting Scholar at NTT Basic Research Laboratory, Japan. Quantum cryptography based on entangled photon pairs.
08/05-09/06: Research assistant at University Heidelberg, Germany, under Dr. Jian-Wei Pan. Quantum computation based on muliti-photon entanglement.

STANFORD PHOTONICS RESEARCH CENTER
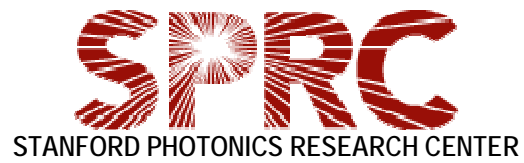
2008 Student Technical Reports

MEGABITS SECURE KEY RATE QUANTUM KEY DISTRIBUTION

Qiang Zhang[1,2], Hiroki Takesue[3], Toshimori Honjo[3], Kai Wen[1], Toru Hirohata[4], Motohiro Suyama[5], Yoshihiro Takiguchi4, Hidehiko Kamada3, Yasuhiro Takura3, Osamu Tadanaga3, Yoshiki Nishida3, Masaki Asobe[3], Alois Mair[1], Yoshihisa Yamamoto[1,2]

1 Edward L. Ginzton Laboratory, Stanford University, Stanford, California 94305, USA
2 National Institute of Informatics, 2-1-2 Hitotsubashi, Chiyoda-ku, Tokyo, 101-843, Japan
3 NTT Basic Research Laboratories, NTT Corporation, 3-1 Morinosato Wakamiya, Atsugi, Kanagawa 243-0198, Japan
4 Central Research Laboratory, Hamamatsu Photonics K.K.
5 Electron Tube Division, Hamamatsu Photonics K.K.

Quantum cryptography (QC) can provide unconditionally secure communication between two authorized parties based on the basic principles of quantum mechanics. However, imperfect practical conditions limit its transmission distance and communication speed. Here we implement differential phase shift (DPS) quantum key distribution (QKD) with up-conversion assisted hybrid photon detector (HPD) to achieve 1.3 M bits per second secure key rate over a 10-km fiber. This is the first megahertz bit rate QKD tolerant against the photon number splitting (PNS) attack, general collective attacks on individual photons, and any other known sequential unambiguous state discrimination (USD) attacks.

In the DPS protocol, the sender first encodes one photon into a sequential pulse train, randomly sets the relative phase of each pulse in the train as 0 or π, and then sends it to the receiver through a fiber link. The receiver uses a 1-bit delay Mach-Zehnder interferometer to make the sequential pulses interfere. Each output of the MZI is connected to a single photon detector, respectively. The relative phase of the sequential pulses decides which detector will receive the photon. When one of the detectors fires, the receiver can conclude whether the phase is 0 or π according to the which-detector information. The receiver records the phase result and the time instance information when he detects a photon. Later the receiver reports the time instance information, from which the sender can tell the value of the relative phase. Therefore the sender and receiver can share the random phase as the quantum key. This protocol is simple but tolerant against all individual attack including the PNS attack.

Here we utilize periodically poled Lithium Niobate (PPLN) waveguide based up-conversion hybrid photon detectors in the experiment. We mix the signal photon with strong pumping light at 980 nm in a wavelength division multiplexing (WDM) coupler and send them to a fiber pigtailed PPLN waveguide for SFG. This device can convert the 1550 nm signal to a 600 nm sum frequency output with an internal conversion efficiency of 99%, detected by a HPD. The HPD incorporates an avalanche diode (AD) into a vacuum tube to receive and amplify the photoelectron from its cathode. In our case, the photon is first injected into the

GaAsP cathode (3mm effective diameter) to generate a photoelectron. The photoelectron is then accelerated by –8,500 V bias and focused onto the 1mm AD, which is 400 V biased. Then, the electron deposits its kinetic energy in the AD and produces thousands of electron hole pairs, which is called an electron bombarded gain. The generated electrons drift in the AD, and are further multiplied by ten to one hundred times by impact ionization. The up-conversion detector's overall quantum efficiency and noise could be controlled by adjusting the pumping laser of the up-conversion detector. The timing jitter (FWHM) of the HPD at Megahertz count rates is still less than 200 ps. To achieve a Megabits per second secure key rate over 10 km fiber, we set the quantum efficiencies of the detectors at 4% and the noise count rates at 30 kHz with 120 mW pump power. We chose a time window of 280 ps and the noise count rate per window was 8.4×10^{-6}.
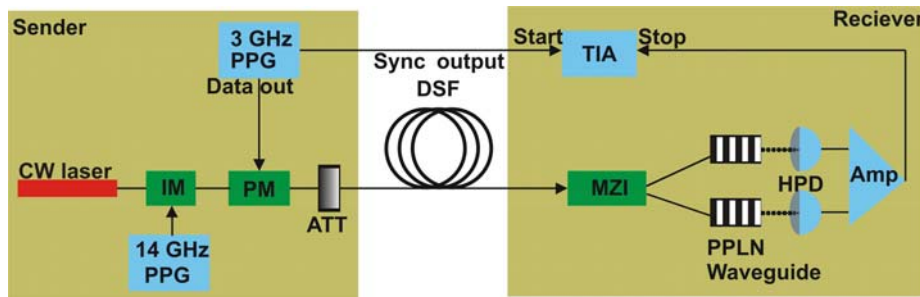
Figure 1 Setup for Megabits Secure Key Rate QKD

The experimental setup is shown in Figure 1. A CW laser was first modulated into a 2 GHz pulse train by a LiNbO$_3$ intensity modulator (IM), with a pulse duration of 70-ps full width at half maximum (FWHM) of a central wavelength of 1550 nm. A 3 GHz pulse pattern generator drove a pseudo random number sequence into a phase modulator to encode the pulse train. We attenuated the encoded pulse train by around 80 dB and set the average photon number per pulse as 0.2. Then we sent the encoded, attenuated pulse to the receiver through a 10-km dispersion shifted fiber (DSF). The receiver used a 1 GHz, 1-bit delay Mach Zehnder interferometer (MZI) to make the sequential pulses interfere. Each output of the MZI is directly connected to an up-conversion assisted HPD, respectively. The output signals of the up-conversion HPDs were sent to a time interval analyser (TIA) to record the detection time instances and which-detector information. This information was used to generate the sifted key.

In the experiment, sifted keys were actually generated between the sender and receiver, and the error rate was measured by directly comparing the sender's key with the receiver's. For each data point described below, we undertook five QKD runs, and the secure key rates were achieved with the experimental results for the sifted key generation rates and bit error rates. The sender and receiver were located in the same room.

We performed the 10-km fiber transmission experiment using fiber spools, while other data points were taken with an optical attenuator simulating fiber loss.
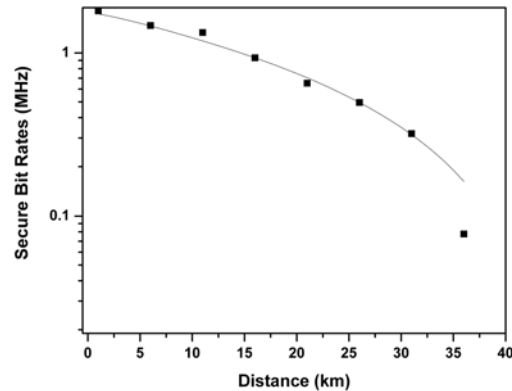
Figure 2 Theoretical curves and experimental results for the

secure key generation rate as a function of fibre length.

We have demonstrated a quantum cryptography system with a megabits per second secure key rate over 10 km fiber link, which was tolerant to all individual attacks including the PNS attack and all known USD attacks. We believe it will be operable in a standard telecommunication network soon. The transmission distance could be extended by reducing the noise counts caused by the parasitic nonlinear process by using an 1810 nm pump. A higher bit rate could be achieved by either develop a special cathode for the 600 nm SFG wavelength or reduce the cathode thickness to improve the timing jitter.

References

- Gisin, N., Ribordy, G., Tittel, W. & Zbinden, H. Quantum Cryptography. *Rev. Mod. Phys.* **74**, 145 (2002).
- Inoue, K., Waks, E. & Yamamoto, Y. Differential-phase-shift quantum key distribution. *Phys. Rev. Lett.* **89**, 037902 (2002).
- Fukasawa, A., Haba, J., Kageyama, A., Nakazawa, H. & Suyama, M. High Speed HPD for Photon Counting. *IEEE Trans. Nucl. Sci.* **55**, 758 (2008).
- Langrock, C., et. al., Highly efficient single-photon detection at communication wavelengths by use of upconversion in reverse-proton-exchanged periodically poled LiNbO$_3$ waveguides. *Opt. Lett.* **30**, 1725 (2005).
- Diamanti, E., Takesue, H., Langrock, C., Fejer, M. M. & Yamamoto, Y. 100 km secure differential phase shift quantum key distribution with low jitter up-conversion detectors. *Opt. Express* 14, 13073 (2006).
- Takesue, H., et. al., Quantum key distribution over a 40-dB channel loss using superconducting single-photon detectors. *Nat. Photonics* **1**, 343 (2007).

FABRICATION OF MONOLITHIC SILICON PHOTONIC CRYSTALS AND THEIR APPLICATIONS

Shrestha Basu Mallick, Sora Kim, Sanja Hadzialic, Il Woong Jung, Chia-Ming Chang, Rishi Kant, Roger Howe and Olav Solgaard
Ginzton Laboratory, Stanford University

Fabrication of Silicon Photonic Crystals (PCs) by etching into silicon using a single lithographically-defined etch mask has several advantages including simple processing, self-aligned structures (all patterns are created by one mask), very low internal stress, tolerance of high temperature processing, resistance to corrosive chemicals, and compatibility with standard MEMS and CMOS processing. The GOPHER (Generation Of Photonic Elements by RIE) process utilizes alternate anisotropic reactive ion etching and isotropic etching to introduce a vertical refractive index variation. The index variation is needed in order to obtain guided resonance modes in PCs which are responsible for the characteristic spectral features of PCs. The fabrication process for single layer PCs [1] is shown in Figure 1.The first oxide film acts as a hard mask to transfer the pattern to the silicon substrate via a reactive ion etch. Another oxidation step follows to protect the sidewalls against further etching. Since oxidation consumes silicon, a consequence of this passivation is that the holes grow larger when the oxide is removed. This should be accounted for in the design and is beneficial in cases where a large air fill factor is desirable. Here the additional oxidation steps have been used in some of the fabricated devices to get hole separations of the order of 50 nm, which is much smaller than the lithography limit of the optical lithography tool that was used for the patterning. After the protective oxide film is formed, it is removed from bottom of the holes by a reactive ion etch. A second directional silicon etch is used to make the holes protrude deeper into the substrate, and is followed by an isotropic SF_6 plasma etch.
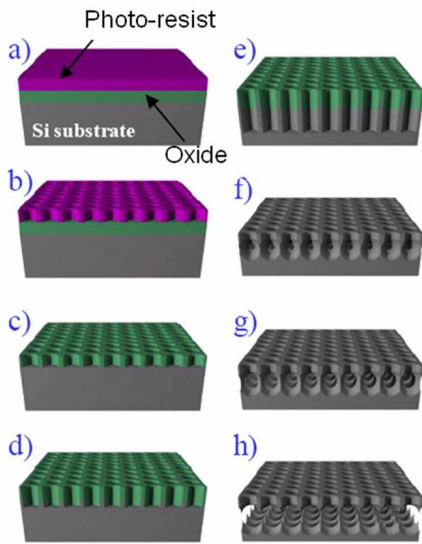
Fig. 1: a) Deposited layers b) PC holes patterned with lithography, c) Pattern transferred to oxide layer, d) Pattern transferred to Si substrate, followed by oxidation and directional etch to remove oxide from the bottom ,e) Holes etched deeper into the substrate, fgh)Isotropic etch
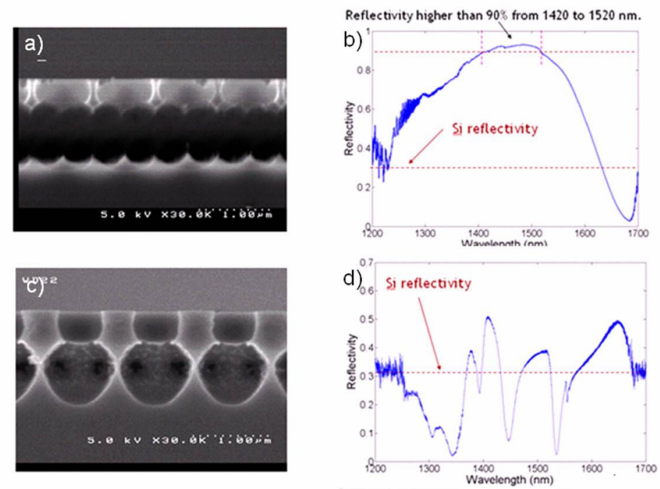
Fig. 2: a) SEM images of the cross sections of completely undercut structure, b) Reflection spectrum from the completely undercut PC Structure c) SEM images of the cross sections of partially undercut structure b) Reflection spectrum from the partially undercut PC structure.

Two different structures were fabricated as seen in Figure 2 a) and c).One of them is completely released, with hole diameter 790 nm and 820 nm pitch, and the other one is partially undercut with hole diameter 620 nm and 1 um pitch. The optical measurement results for the completely undercut structure are shown in Fig. 2b) This structure has a very broad high reflectivity region with reflectivity higher than 90% in the range from 1420 to 1520 nm. The partially undercut structure also shows regions of reflectivity higher than that for silicon (31%) (Fig. 2d). In addition, this structure exhibits a sharp interference creating a transmission maximum around the 1550 nm wavelength.

The GOPHER process is then extended to double-layer structures [2]. This is a step towards creating multilayered structures with sub micron periodicity with the potential to facilitate fabrication of three dimensional (3D) PCs using silicon micromachining. The process demonstrated here is more versatile than earlier reported multilayer processes because the isotropic etch steps are alternated with anisotropic etches. Thus this process can be used to make a single or multiple layers of PC membranes with various degrees of undercut. In addition, the process has more degrees of freedom and gives a greater degree of control over the ratio of the radius of the spherical voids to the pitch of the PCs, which can be varied by the relative durations of the isotropic and anisotropic etches. This ratio is a key factor in tuning the guided resonance mode characteristics.

Figure 3 compares the reflection spectra of a single layer and double layer GOPHER structure that have the same initial design of holes of diameter 700 nm with a pitch of 1100 nm. The two crystals are processed identically up to the first isotropic etch. As a result of the protective oxidation, the holes in the single layer structure have a diameter of 880 nm and the holes in the double layer structure have a diameter of 930 nm. It is seen that there are more resonances in the double-layer structure and the resonances appear sharper. Also, the overall reflectivity increases. The reflectivity of the peak at the center of the spectrum goes from around 44% to 67%. This agrees with the predictions of FDTD simulations that indicate a general trend of sharper resonances and increased reflectivity as the number of layers is increased. It should be noted that the difference in the radii of the holes changes the nature of the spectrum, which explains the slightly shifted peaks. For the structure in Figure 4, the initial design was for holes with 600 nm diameter and a pitch of 900 nm. Measurements show that after processing the hole diameter is 850nm. The first isotropic undercut seems to have cleared most of the material away, leaving a free standing membrane with a large air fill factor resulting from the enlarged holes. This, in itself, gives a spectrum with broadband reflectivity. The second isotropic etch gives spheres of diameter 450 nm. Simulations indicate that this will increase the reflectivity further. Reflectivity measurements of the current structure indicate a maximum reflectivity of 96 % with over 90% reflectivity from1580 nm to 1650nm. By decreasing the pitch, the broadband region can be shifted towards shorter wavelengths.
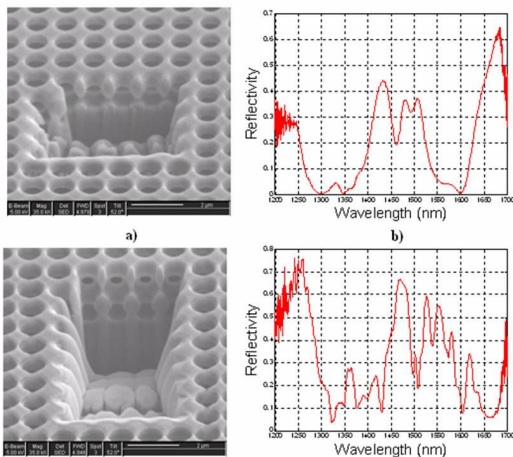
Fig.3a,b) SEM and reflections spectrum of a single-layer structure. c, d) SEM and reflection spectrum of two-layer PC.
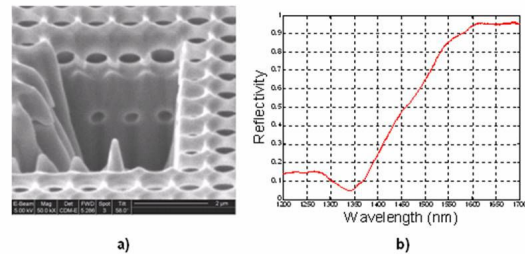
Fig.4a,b) SEM and reflection spectrum of high reflectivity structure

It was also demonstrated by our group [3] that the optical reflection spectra of GOPHER PCs can be modified by hydrogen annealing, leading to higher reflectivity and sharper resonance peaks due to improved structural uniformity. Figure 5 (a) and (b) show the structural changes of the PCs due to the long hydrogen anneal. The silicon surfaces are smooth and no longer have the sharp spikes created by the isotropic etching with SF_6. However, the sidewalls are not straight and still show sharp corners at the edges of the oxide layers that protect the sidewalls. Figure 6 compares the reflection spectra of two structures that are nominally identical, but one has undergone hydrogen anneal and the other has not. The spectra shown as black lines correspond to the structure before hydrogen annealing, while red lines correspond to the structure after hydrogen annealing. For both of the polarizations the reflectivity has increased and sharper resonance peaks are observed. The polarization dependence can be explained by the 70nm hole elongation along the x direction and 40nm difference in the pitch of PCs along the x and y directions, introduced by the e-beam lithography.

After the first hydrogen anneal, the protective oxide on the sidewalls was removed, and the second hydrogen anneal was performed. As shown in Fig. 7 (a) and (b), after the second hydrogen anneal the interfaces are smoother, the edges are rounded, and the holes are more uniform and symmetric, leading to significant changes in the reflectance spectrum as shown in Fig. 7 (c). It is interesting to note that the polarization dependence of the reflections is decreased.
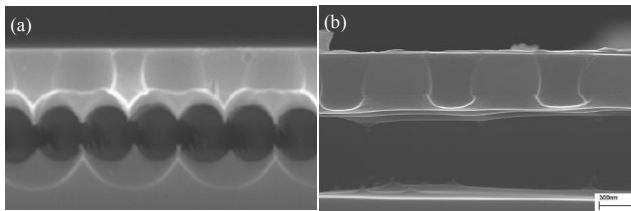
Fig 5 (a) PC cross-section before the first hydrogen anneal. (b) PC cross-section after the first hydrogen annealing.
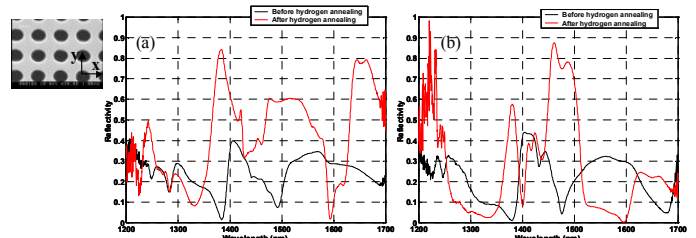
Fig 6(a) Measured reflection spectra for perpendicular polarizations ((a): x polarized, and (b): y polarized). Black: reflection spectra before the first hydrogen anneal. Red: reflection spectra after the first hydrogen anneal.
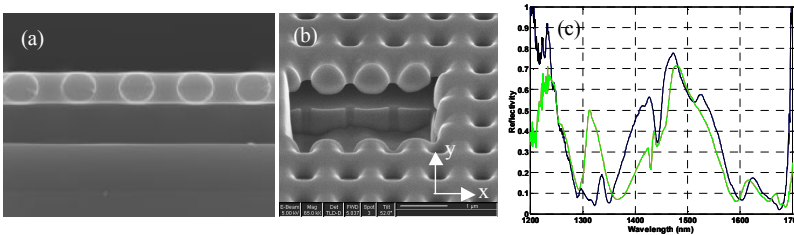
Fig. 7. (a) (b) SEMs of the PCs after the second hydrogen anneal. (c) Reflection spectra for perpendicular polarizations: green: x polarized, black: y polarized

References

[1] S. Hadzialic, S. Kim, S. Basu Mallick, A. Sudbo, and O. Solgaard, "Monolithic Photonic Crystals", 2007 IEEE/LEOS Annual Meeting Conference Proceedings, Lake Buena Vista, Florida, 21-25 October 2007, pp. 341-342

[2]S. Basu Mallick, S. Kim, S. Hadzialic, A. Sudbo, and O. Solgaard, "Double-layered Monolithic Photonic Crystals," CLEO, San Jose, CA, May 2008

[3] S. Kim, R. Kant, S. Hadzialic, R. Howe, and O. Solgaard, "Interface Quality Control of Monolithic Photonic Crystals by Hydrogen Annealing", CLEO, San Jose, CA, May 2008

SiGe/Ge Quantum Well Modulators Employing the Quantum-Confined Stark Effect

Stephanie A. Claussen*, Rebecca K. Schaevitz, Jonathan E. Roth, Onur Fidaner, Emel Tasyurek, Shen Ren, Elisabeth Edwards, Ross Audet, Lilian Tran, and David A. B. Miller
Ginzton Laboratoryy, Stanford University
Corresponding author:sclaussen@stanford.edu

Germanium is increasingly important for integrating photonics into silicon IC technology. Recent demonstrations of the quantum-confined Stark effect (QCSE) [1] in SiGe/Ge quantum wells (QWs) [2] open many new device possibilities, including high-performance, group IV optical modulators and detectors. These QW designs show a strong electroabsorption affect, which led to the first QCSE-based electroabsorption modulators in SiGe. Here, we begin by investigating some of the key materials properties that affect our QW device design. These include the quantum mechanical transitions that occur in the QWs and the femtosecond dynamics of the photoinduced carrier populations. We then go on to present the results from a number of different device structures, including a waveguide modulator [3] and detector [4] and a novel side-entry modulator on silicon [5] and silicon-on-insulator (SOI) wafers [6].

The device used to test photocurrent and observe the QCSE is a p-i-n diode with $Si_{0.1}Ge_{0.9}$ background composition and a superlattice of $Ge/Si_{0.16}Ge_{0.84}$ QWs in the intrinsic region. The well widths range between 16nm and 24nm with barrier widths adjusted for strain-balancing. The quantum wells are formed using the appropriate direct gap bands of both Si and Ge. The addition of strain due to lattice mismatch, the large direct bandgap of Si, and the unknown band lineups of Si and Ge all contribute to significant unknowns in the material parameters needed for modeling.

We have investigated the shifts of multiple different transitions for the first time in such QWs, fitting experimental photocurrent results (Fig. 1(a)) with quantum-mechanical tunneling resonance calculations [7]. Initial modeling of the shifting of the exciton peaks with applied electric field using material parameters extracted from theory and bulk Si and Ge did not perfectly match the experimental data (Fig. 1(b)). It was found that non-parabolicity, a linearity of the band at higher energies above bandgap, plays a significant role in the direct conduction band of Ge. By adding the non-parabolic energy-momentum relationship derived by Ekenberg, *et al* [8], into the tunneling resonance model, we were able to accurately fit the experimental data for all well widths (Fig. 1(b)). The slight discrepancies in some of the transitions can be explained by other effects, such as underlying absorption of the Franz-Keldysh effect and the indirect absorption.
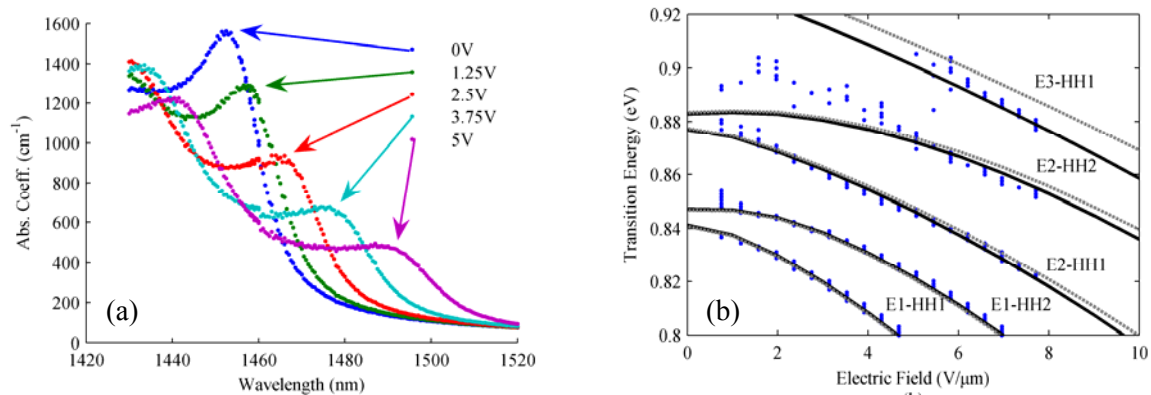
Fig. 1: (a) Photocurrent Spectra of 16nm well, (b) Experimental peaks (blue dots) of a 23nm well with the simple model (gray dashed line) and the non-parabolic model (black solid line). E and HH refer to electron and heavy hole sub-bands, respectively, in the Ge quantum wells.

Using the same p-i-n diode device structure, we have also investigated the dynamic process in SiGe/Ge wells of the intervalley scattering of electrons in the conduction band from the direct Γ valley to the indirect L valley. Time-resolved transmission data was recorded using a pump-probe setup to measure the intervalley scattering time. We see a strong bleaching soon after the point of zero delay between the pump and probe beams, followed by a strong recovery (Fig. 2). This data is reported at a bias of 21V and at a temperature of 100°C, due to what we believe is the optimized overlap of the exciton peak and the laser linewidth of our 1550nm short-pulsed laser. The dominant absorption change on a sub-picosecond time scale is due to bleaching associated with the electrons occupying the direct Γ conduction band valley. We expect that electrons excited into the direct gap zone-center Γ conduction band valley may scatter on a time scale of a few hundred femtoseconds into the lower energy, indirect L valley, leading to a corresponding rapid recovery of the absorption bleaching. We deduce an upper estimate for the electron intervalley scattering time of ~200fs, based on fitting an exponential recovery to the absorption bleaching (Fig. 2).
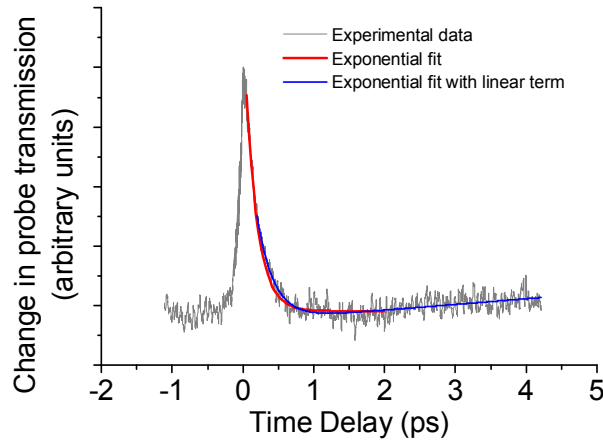
Fig. 2. Change in the transmission of the probe beam as a function of the relative time delay between the pump and probe pulses. The transmission recovers in around ~200fs.

Using the sample with a 16nm well, we have demonstrated interconnect devices in both waveguide [3,4] and mesa structures [5,6]. The first-generation waveguide structure (see Fig. 2(a)) was able to demonstrate a clear open-eye diagram at 2.5 Gb/s at 1530nm (see Fig. 2(b)) with 120ps full-width half-maximum [3]. As a modulator it was showed a 7.72dB contrast ratio (CR) for a 6V swing at 1476nm [4]. Heating to 100°C has proven effective for shifting the spectrum to the C-band without degradation of the exciton peaks.
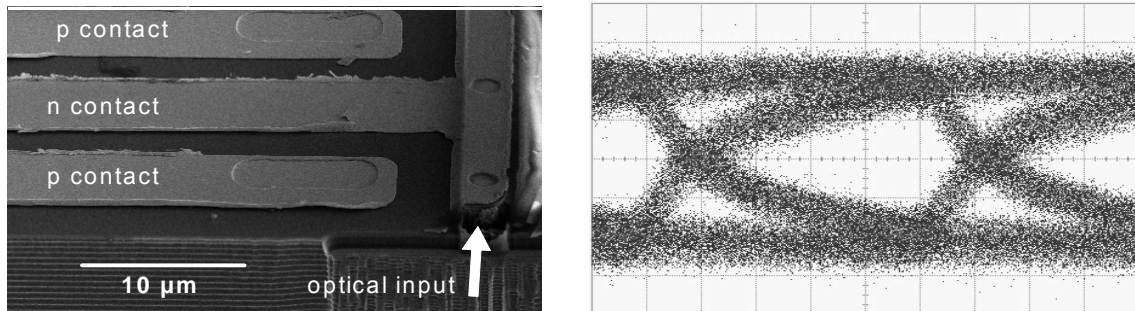
Fig. 3. (a) Waveguide structure and (b) Experimental data showing 2.5 Gb/s NRZ Eye diagram at 1530 nm. (horizontal 75 ps/div and vertical 5 mV/div) [4]

Novel side-entry electroabsorption modulators designed as an asymmetric Fabry Perot resonator led to maximal contrast ratios of the transmitted light owing to frustrated total internal reflect (TIR) [4,5]. Initial devices with 40 QWs on Si substrates demonstrated a 7.3dB CR at 1457nm for

a 10V swing and a greater than 3dB CR from 1441nm to 1461nm with significant misalignment tolerance.
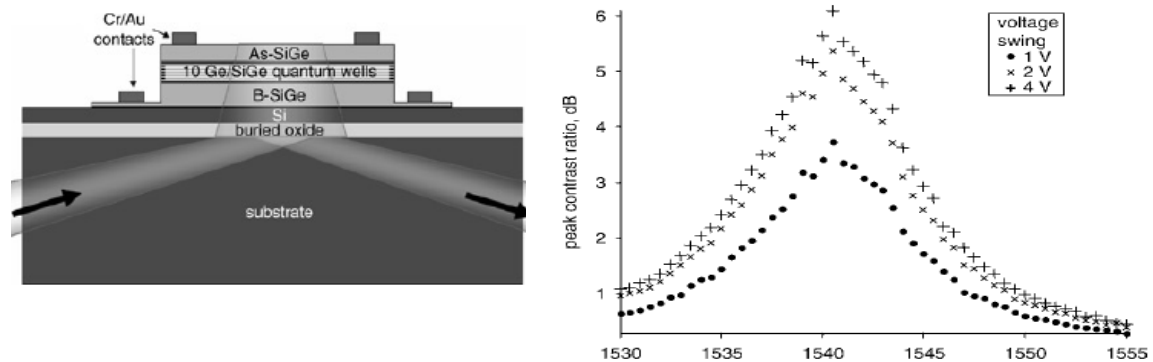
Fig. 4. (a) Side-entry electroabsorption modulator on SOI [6]. (b) Peak contrast ratio for electroabsorption modulator on SOI at 1541nm and 100C [6]

These devices were significantly improved when the same material structure was grown on an SOI wafer. The buried oxide acted as a mirror enhance by the laser's angle of incidence, improving the confinement of light at certain resonance conditions (see Fig. 3). Additionally, the device was heated to 100C to shift the exciton peaks to higher wavelengths. The resulting contrast ratios are a significant improvement over the Si wafer devices. These experimental results are the first demonstration of an electroabsorption modulator employing the QCSE in SiGe in the C-band with voltage swings compatible with CMOS electronics.

The SiGe/Ge material system has significant implications in achieving a strong electroabsorption modulator and detector compatible with Si technology. We have presented material properties that accurately model the experimental data and have measured the intervalley scattering time of electrons in the conduction band. Without any optimization, we have demonstrated a high speed waveguide detector and a modulator that operates in the C-band with only a 1V swing.

References:
[1] D. A. B. Miller, *et al*. "Band-edge electroabsorption in quantum well structures: the quantum-confined Stark effect," *Phys. Rev. Lett.* **53**, 2173-2176 (1984).
[2] Y. H. Kuo, *et al*. "Strong quantum-confined Stark effect in germanium quantum-well structures on silicon," *Nature* **437**, 1334-1336 (2005).
[3] O. Fidaner, *et al*. "Waveguide Electroabsorption Modulator on Si Employing Ge/SiGe Quantum Wells," *OSA Frontiers in Optics*, FMC2 (2007).
[4] O. Fidaner, *et al*. "Ge-SiGe Quantum-Well Waveguide Photodetectors on Silicon for Near-Infrared," *IEEE Photonics Technol. Lett.*, **19**, no. 20, 1631-1633 (2007).
[5] J. E. Roth, *et al*. "Optical modulator on silicon employing germanium quantum wells," *Optics Express*, **15**, no. 9, 5851-5859 (2007)
[6] J. E. Roth, *et al.* "C-band side-engry Ge quantum-well electroabsorption modulator on SOI operating at a 1 V swing," *Electron. Lett.*, **44**, no. 1 (2008).
[7] R. K. Schaevitz, *eta al*. "Material Properties of Si-Ge/Ge Quantum Wells," *IEEE J. Selected Topics in Quantum Electronics*, **14**, 4, 1082-1089 (July/Aug. 2008)
[8] U. Ekenberg. "Nonparabolicity effects in a quantum well: Sublevel shift, parallel mass, and Landau levels." *Phys. Rev. B* **40**, No. 11, 7714-7726 (1989)

MEMS OPTICAL FILTER WITH TUNABLE CENTER WAVELENGTH AND PASSBAND

Jae-Woong Jeong, Il Woong Jung, and Olav Solgaard

Ginzton Laboratory, Stanford University

Tunable optical bandpass filters are key components for dynamic wavelength provisioning in reconfigurable optical networks and communication systems. Among several methods implementing tunable optical filters, MEMS technology has strong potential for high-performance filters. By using MEMS actuators, precise and independent control of center wavelength and bandpass is possible. Several researchers reported tunable optical filters using micromirror arrays [1 – 3], but the tuning of their center wavelengths and bandwidths are digitalized, thus lacking continuous tuning capability. In this paper, based on MEMS platform technology, we introduce a tunable MEMS optical bandpass filter with large vertical mirrors (450um tall) assembled on MEMS actuators. The fabrication process requires only one mask, and the platform technology allows a compact chip size with high optical quality vertical mirrors. In addition, electrostatic combdrive actuators enable independent and continuous control of center wavelength and optical passband.

A conceptual schematic of the tunable optical bandpass filter with MEMS mirrors is shown in Figure 1.
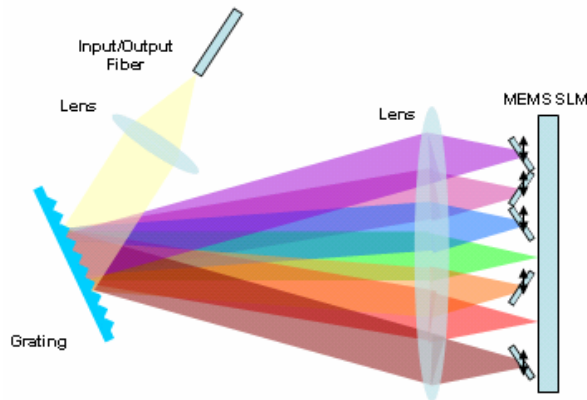
Figure 1: A schematic diagram of the tunable optical bandpass filter system

By changing the size and center location of the aperture of the MEMS reflector, we can precisely control the bandwidth and center wavelength of the optical filter without modifying the shape of its transition band. The light reflected from the fixed back-mirror traces back through the incident optical path and couples back into the input/output optical fiber. On the other hand, light that is incident on the movable blocking micromirrors do not return to the fiber. The reflection angle from the blocking mirrors is set to 30º, which makes the insertion loss high outside the passband.

Electrostatic combdrive actuators are used to achieve linear, large displacements. In addition, double folded-beams (Fig. 2) are used as springs to sustain large stable displacements. This particular type of spring has high stiffness in the orthogonal direction of displacement, thus exhibiting a larger linear deflection range than a single straight-beam spring. The length, width, and height of the folded beam in our design are L = 1100um, b = 3um, and h = 40um, which yields a spring constant of 0.346 N/m. The combdrives are designed to have 4um-width comb finger and 6.5um comb gap. The total number of movable combs is 344.

For fabrication, we used a SOI wafer with a thickness of 40µm, 4µm, 400µm in the device layer, buried oxide, and substrate, respectively. The process starts with wet oxidation of the wafer at 1000ºC in order to grow a thin layer of oxide, which will be used as a hard mask for deep reactive ion etching (DRIE). Then, the resist is patterned and etched into the oxide hard mask. The device layer is etched using DRIE. Finally, the wafer is diced into 7.65mm × 7.65mm dies and released in 49% liquid HF. Figure 2 shows SEM images of the fabricated device.
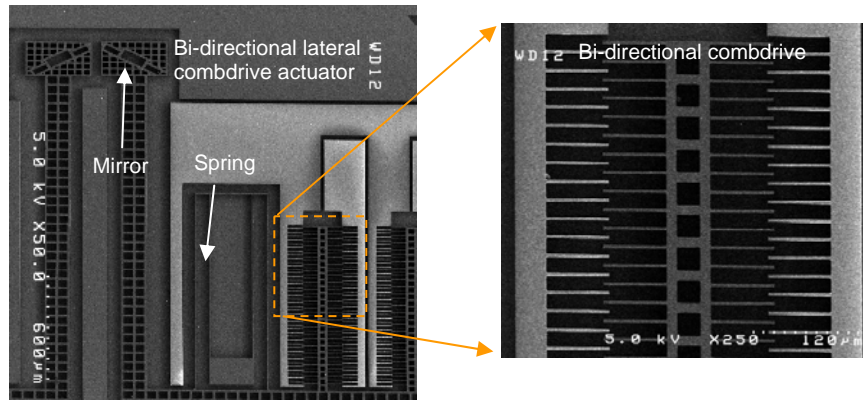
Figure 2: SEM image of a fabricated two-actuator model device

Figure 3 plots the static deflection curves in two opposite directions of the actuator. The measurement shows that the actuator has the maximum stable displacement of ~45um to the left and ~50um to the right, therefore achieving the maximum tuning range of ~95um.
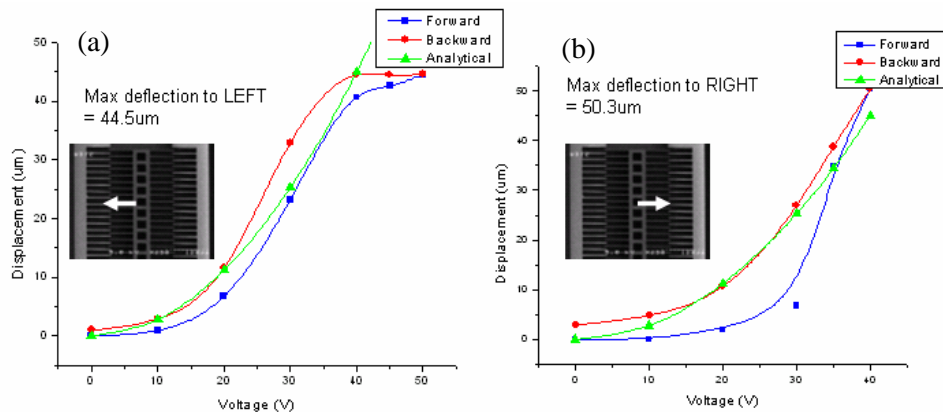
Figure 3: Static deflection measurement (a) displacement to the left, (b) displacement to the right

Future work will include assembly of the vertical mirrors to the mirror pads and demonstration of the device in an optical system as shown in Figure 4.
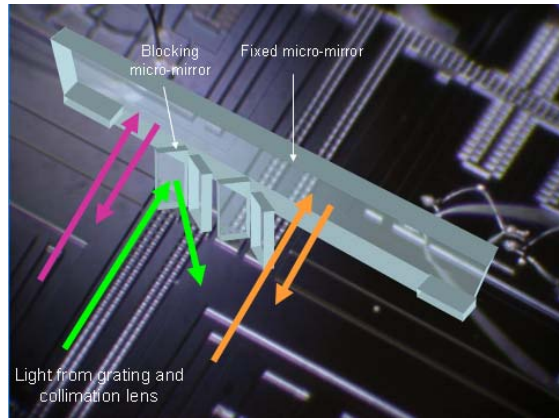
Figure 4: The schematic diagram showing micro-assembly of components and light-path

References

[1]   M. Knapczyk, A. Krishnan, L. Grave de Peralta, A. A. Bernussi, and H. Temkin, "Reconfigurable optical filter based on digital mirror arrays," IEEE Photon. Tech. Lett., vol. 17, pp. 1743 – 1745, 2005.

[2]   G. Wilson, C. J. Chen, P. Gooding, and J. E. Ford, "Spectral filter with independently variable center wavelength and bandwidth," IEEE Photon. Tech. Lett, vol. 18, pp. 1660 – 1662, 2006.

[3]   T. Zhou, D. O. Lopez, M. E. Simon, F. Pardo, V. A. Aksyuk, and D. T. Neilson, "MEMS-based 14GHz resolution dynamic optical filter," Electron. Lett., vol. 39, pp. 1744 – 1746, 2003.

Spectral Analysis of Scattering in Metal-Insulator-Metal Waveguides and Related Equivalent Circuit Models

Şükrü Ekin Kocabaş, Georgios Veronis, David A.B. Miller and Shanhui Fan

Ginzton Labs, Stanford University, CA & Louisiana State University, Baton Rouge, LA

kocabas@ieee.org, gveronis@lsu.edu, dabm@ee.stanford.edu, shanhui@stanford.edu

Abstract: We show that the two dimensional MIM plasmonic waveguide has a discrete and a continuous spectrum, similar to the dielectric slab waveguide. Using this complete spectrum, we calculate the equivalent circuit model for waveguide junctions.

We show how to analyze metal-insulator-metal waveguides based on their full modal spectrum, and apply this model to understand scattering at waveguide junctions. The modal spectrum for plasmonic guides, though related to that of dielectric guides, has important differences in both the continuous and the discrete part of the mode spectrum that are essential for modeling scattering and that are related to phenomena known from open microwave guides [1].
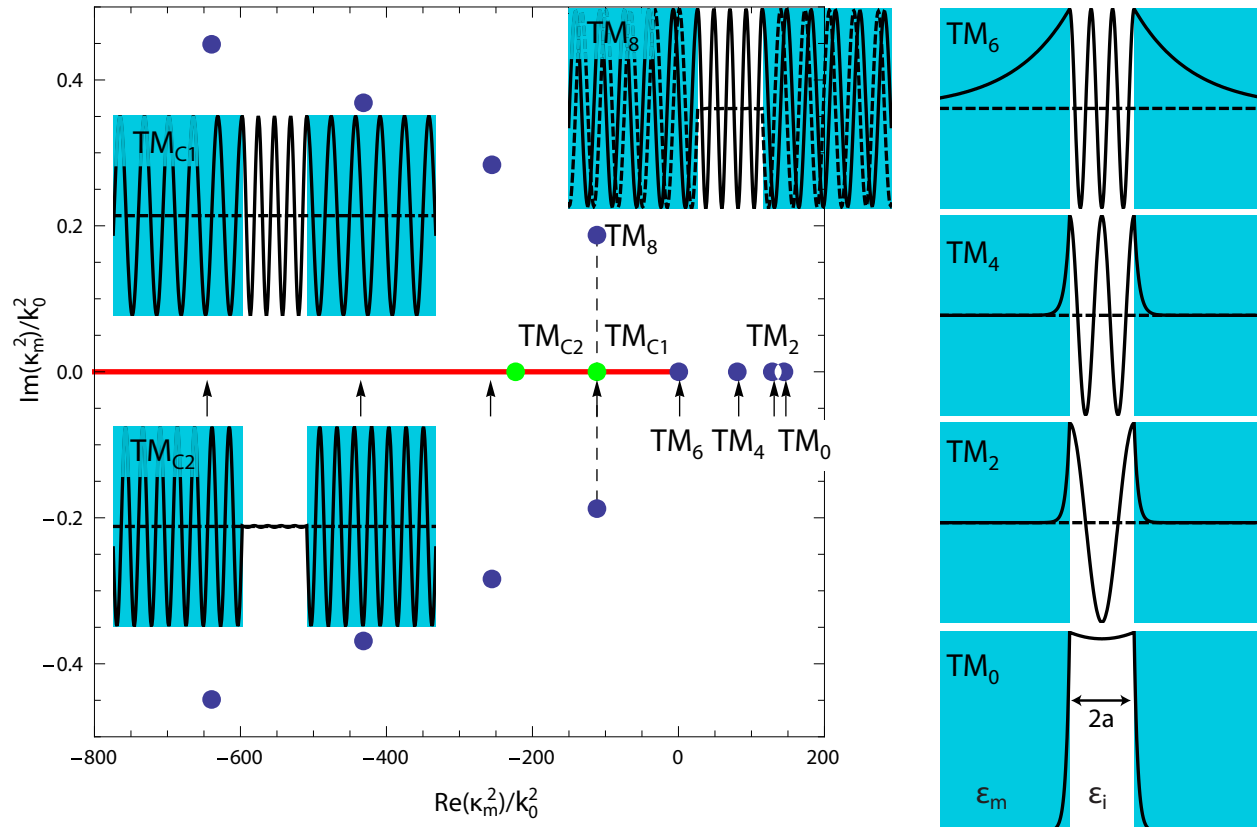
Fig. 1. Spectrum of the MIM waveguide for a lossless metal with $\varepsilon_m = -143.497$, an air of vacuum core with $\varepsilon_i = 1.0$ and $2a = \lambda/4$ where $k_0 = 2\pi/\lambda$ and where $\lambda = 1550$nm is the wavelength of operation. There are four real modes and an infinite number of complex modes, all denoted with the ● symbol. The **thick line** denotes the continuous spectrum. Due to the fact that ε_m is real, complex modes come in complex conjugate pairs. Insets show the magnetic field mode shapes for the discrete spectrum (TM_0 through TM_8) and the continuous spectrum (TM_{C1} and TM_{C2})—solid lines in the insets are the real part of the mode, dashed lines are the imaginary part. The location of the drawn continuous modes are shown by the ● symbol. Continuous modes are purely oscillatory whereas complex modes have a small decay. Arrows (↑) denote the position of the modes of a parallel plate waveguide with a separation of a.

We are interested in analyzing the scattering of the main *transverse magnetic* (TM) mode of the MIM waveguide at symmetric MIM junctions. Such a problem can be analyzed by the even TM modes which we visualize on the κ_m^2

plane in Fig. 1. Here, κ_m refers to the exponential decay of the discrete spectrum in the metal. The spectrum for a lossless metal, $\varepsilon_m \in \mathbb{R}$, has a real and a complex discrete part as well as a continuous one. The discrete spectrum is obtained by finding the roots of the dispersion equation via the use of the *argument principle method* [2]. $\kappa_m = 0$ is the bifurcation point at which the real spectrum splits into two complex branches with a forward and a backward phase velocity respectively.

The continuous spectrum is found by replacing the condition of square integrability of the modes by the weaker condition of finiteness of the modes at their domain of definition [3, p. 16]. This implies a non-zero, yet finite electromagnetic field at infinity. These infinite-extent, therefore infinite energy, continuum modes are integrated to realize any physically possible finite energy field configuration.

It is possible to expand an arbitrary field profile in terms of the complete spectrum of the MIM waveguides. By the use of the well known mode-matching technique [4]—which we verified against *finite-difference frequency-domain* (FDFD) calculations—one can then analyze the scattering of electromagnetic waves at MIM waveguide discontinuities. In Fig. 2 we show the reflection coefficient of the main mode of the MIM waveguide as a result of scattering from a waveguide junction. Such an analysis reveals the qualitative similarity between modal scattering at parallel plate and MIM waveguide junctions.
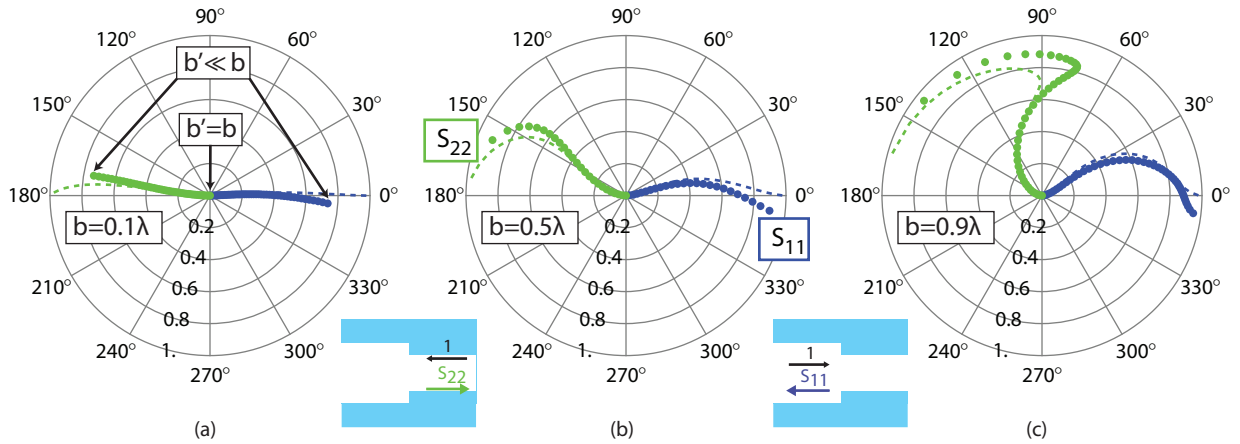
Fig. 2. Polar plot of S_{11} (●, plots heading out to the right half of the diagram) and S_{22} (●, plots heading out towards the left half of the diagram) on the complex plane, which is called the Smith chart in the microwave literature. Circles are used for the MIM case, dashed lines are used for the PEC (perfect electrical conductor) case. Each subplot is for a fixed left waveguide thickness b with a varying right waveguide thickness b'. In all three subplots the origin is the zero reflection point which corresponds to $b' = b$. As b' decreases progressively towards zero, we move progressively along the curves away from the origin. The end points of the dashed curves on the unit circle correspond to $b' = 0$. In all three cases, the free-space wavelength of light is fixed at $\lambda = 1550$nm. (a) $b = 0.1\lambda$. (b) $b = 0.5\lambda$. (c) $b = 0.9\lambda$.

Once the scattering coefficients of a waveguide junction are obtained, one can then use the scattering matrix formalism to design interacting junction geometries. For instance, a generalization of the quarter wave impedance matching technique of transmission line theory results in the following conditions between the elements of the scattering matrices for a three waveguide system as depicted in Fig. 3(a)

$$|^L S_{22}| = |^R S_{11}| \qquad \text{(magnitude condition)} \qquad (1)$$

$$\angle^L S_{22} + \angle^R S_{11} = 2k_C \ell + 2\pi n \qquad \text{(phase condition)} \qquad (2)$$

Here k_C refers to the propagation wave vector of the main mode of the center waveguide. Satisfying the conditions above leads to a reflectionless transition from an MIM waveguide on the left to the one on the right via the matching section in between. In our design we choose the left waveguide width to be 0.9λ and the center waveguide width to be 0.5λ as shown in the inset in Fig. 3. The parameters that we need are the insulator width of the right waveguide, w, and the length of the center waveguide, ℓ.

The width of the right waveguide can be chosen by satisfying (1). In Fig. 3(b) P_L is the location of the $b = 0.9\lambda$ to $b' = 0.5\lambda$ junction on the $^L S_{22}$ curve. To satisfy (1) we need to have $|^L S_{22}| = |^R S_{11}|$. The solution can be graphically found by drawing a circle in the complex plane with a radius $|P_L|$ centered at the origin and finding its intersection with the $^R S_{11}$ curve. The intersection point is denoted by P_R. P_R corresponds to a right waveguide thickness of 0.16λ.

The phase condition (2) is then easily calculated from the phases of the scattering coefficients, $\angle P_L$ and $\angle P_R$. After some simplification through the use of the numerical value for k_C one gets $\ell/\lambda = 0.1377 + 0.4861n$, where n is any positive integer. We verified this design by FDFD simulations.

The use of the transmission line theory is very common in microwave literature. It leads to a concise representation of field propagation. Once the scattering matrix, $\mathbf{S}$, for a junction is characterized, the matrix can be mapped to an equivalent circuit in a transmission line model. There is no unique way to describe $\mathbf{S}$ using lumped circuit elements [5, p. 316]. To choose one circuit out of the infinite possible set that could correspond to the same $\mathbf{S}$, we investigated the well studied PEC case and added another term to the PEC parallel plate waveguide junction model to account for the properties of metals at optical frequencies. The resulting circuit model for symmetric MIM junctions is as shown in Fig. 3(c).

In conclusion, we characterized the even part of the TM spectrum for the MIM waveguide geometry. We showed that combination of the discrete and the continuous spectrum forms a complete basis. Using this modal representation, we analyzed scattering of modes at waveguide junctions and came up with a circuit model that shows and extends the analogy to microwave guides.
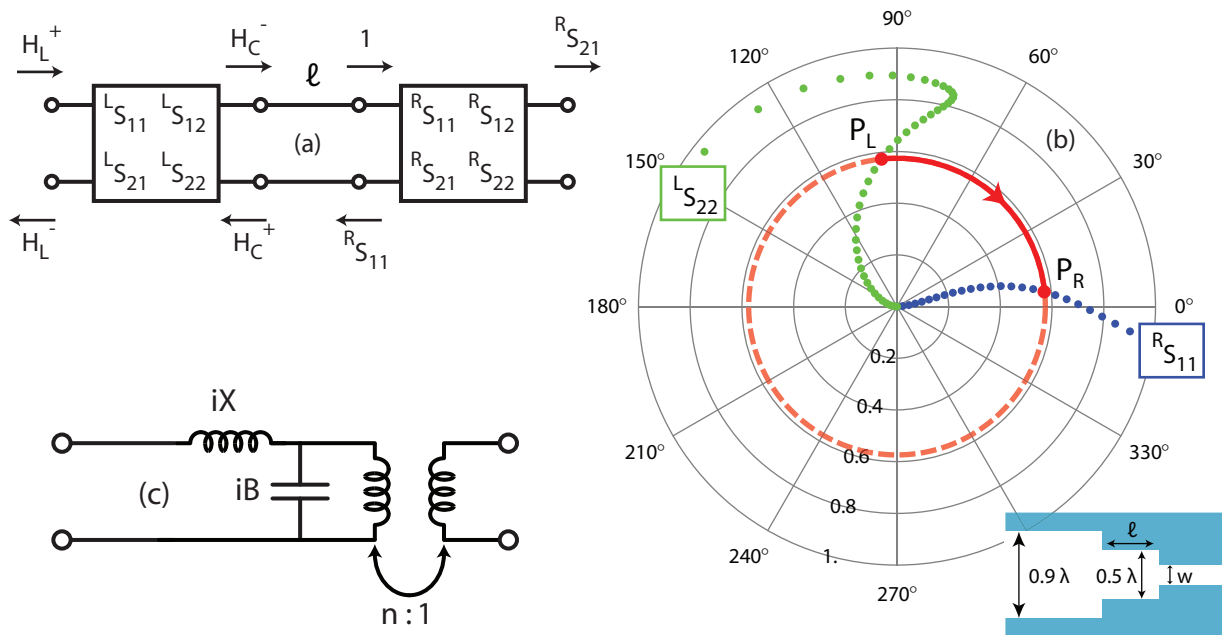
Fig. 3. (a) Schematic diagram of modal propagation in a three waveguide system as shown on the inset. The left and right junctions are shown as boxes with an $\mathbf{S}$ matrix description. The center waveguide is shown as a transmission line of length ℓ. The source that creates the fields is normalized such that the mode that propagates to the right has a unit magnitude at the input of the right junction. (b) Graphical solution of (1) and (2) on the complex plane. Point P_L is the location of the left junction on the $^LS_{22}$ curve where $b = 0.9\lambda$ and $b' = 0.5\lambda$. Point P_R is the location of the right junction on the $^RS_{11}$ curve where $b = 0.5\lambda$ and $b' = 0.16\lambda$. (c) Equivalent circuit model for a waveguide junction described by a scattering matrix $\mathbf{S}$. B signifies the near field interactions, n signifies the characteristic impedance ratio of the waveguides on both sides of the junction and X signifies the reactive surface impedance of metals at optical frequencies.

References

[1] T. Rozzi and M. Mongiardo, *Open Electromagnetic Waveguides*. The Institution of Electrical Engineers, 1997.

[2] E. Anemogiannis and E. N. Glytsis, "Multilayer wave-guides - efficient numerical analysis of general structures," *Journal of Lightwave Technology*, vol. 10, no. 10, pp. 1344 – 1351, OCT 1992.

[3] V. V. Shevchenko, *Continuous Transitions in Open Waveguides*. Boulder, Colorado: Golem Press, 1971.

[4] P. J. B. Clarricoats and K. R. Slinn, "Numerical solution of waveguide-discontinuity problems," *Proc. IEE*, vol. 114, pp. 878 – 887, 1967.

[5] E. L. Ginzton, *Microwave Measurements*. McGraw-Hill Book Company Inc., 1957.

PLASMONIC PHOTODETCTORS IN SI CMOS

Liang Tang, Salman Latif, David. A. B. Miller
Ginzton Laboratory, Stanford University

Plasmonics is an emerging device technology which exploits the unique optical properties of metallic nanostructures to manipulate and route light at the nanoscale [1]. Plasmonics has the potential to play a unique and important role in integrating optical devices with Si electronics on the chip level. In particular, the confinement of light with metallic nanostructures to dimensions comparable to electronic devices may bridge the gap between microscale dielectric photonic devices and nanoscale electronics [2, 3]. However, little work has been done in the context of integrating plasmonic devices on a realistic electronics platform. Current Si-based integrated circuit technology already uses metallic nanostructures, such as Cu and Al interconnects, to route electronic signals between transistors on a chip. This mature processing technology can thus be used to our advantage in integrating plasmonic devices with electronic circuits. Using Al metal, here for the first time, we demonstrate plasmonic devices fabricated on a commercial Complementary Metal–Oxide–Semiconductor (CMOS) chip, paving the way for plasmonics to become the next wave of chip-scale optoelectronic technology.

Our test chip is fabricated in a commercial Silicon on Sapphire (SOS) CMOS process, developed by Peregrine Semiconductor. Previous work in our group showed that the SOS process was a feasible platform for integrating photodetectors with CMOS electronics [4]. A 70nm thick active Si layer is used to form a lateral P-I-N structure. The width of the intrinsic region between the heavily doped P+ and N+ contact areas is set by the finger spacing parameter, which varied between 1.2 μm and 6 μm in different structures. Multiple fingers are combined in parallel to extend the detector area in the lateral direction. We operate these detectors at blue wavelengths (425 nm). The absorption depth in silicon at that wavelength is approximately 180 nm, so reasonable responsivity is possible under surface normal illumination. Most importantly, the absence of a semiconductor substrate results in extremely low capacitance devices. A 5 μm x 5 μm size detector with a finger spacing of 1.2 μm and $\sim$ 30 ps rise time is calculated to have a capacitance of $\sim$ 4 fF.

Metallic nanostructures, designed appropriately, can be used to enhance photocurrent density in a semiconductor photodetector. In this approach, we use a C-shaped nanoaperture in a thin Al layer to enhance the relative photocurrent of the PIN detector. The single C-shaped aperture, without any other supporting surface structures, can collect light from an area much larger than the physical area of the aperture, leading to strong field concentration in the aperture. To fabricate nanoapertures on the chip, we

first make an opening in the target region above the photodetectors using focused-ion beam (FIB) milling, leaving the rest of the chip protected. After removing the top dielectric layers and exposing the interdigitated

(a)

(b)
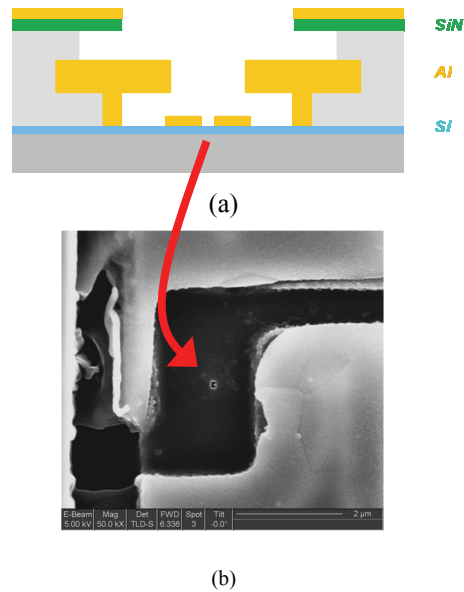
Fig. 1: (a) Cross-sectional view of the final device, and (b) SEM image of the final device

metal fingers, we use buffered oxide etch to remove the remaining dielectrics until the intrinsic Si layer is exposed. Then Al of 150 nm thickness is deposited on the intrinsic Si. Finally, FIB is used to make the nanoapertures in the Al layer. Fig. 1 shows a drawing of the cross-sectional view and the SEM image of the final device. Note the nanoscale C-shaped aperture in the center of the SEM image. The aperture is about 1 μm lower in height than the top surface of the metal fingers.

For comparison purposes the photocurrent from a C aperture and a square aperture of the same designed area are measured using a chopped laser beam and a lock-in amplifier. An 850 nm short pulse laser is used to generate the 425 nm laser beam through second harmonic generation.

The laser spot is focused to about 11 μm in diameter. We measure the polarization dependence of the photocurrent by rotating a half-wave plate in the optical path (Fig. 2). The C aperture photocurrent reaches maxima when the light polarization is parallel to the two "arms" of the aperture (y polarized) and falls to minima when it is perpendicular to them (x polarized), as expected theoretically. This polarization dependent signal of the C aperture detector is direct evidence of an antenna effect in the blue. In contrast, there is no evident polarization dependence for the square aperture detector. The photocurrent of the C

aperture detector for *y*-polarized light is measured to be 4.5 times that of a square aperture of the same designed area. The particular C aperture used in this measurement has a smallest feature size of 40 nm. The SEM images of the C aperture and square aperture are shown in Fig. 2(b) and 2(c) respectively.
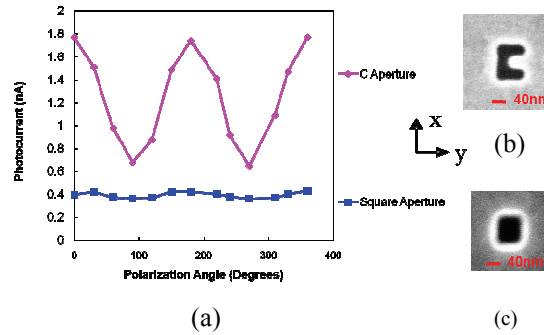
Fig. 2: (a) Photocurrent polarization dependence, (b) SEM image of the C-aperture and (c) SEM image of the square aperture

In summary, we present a plasmonic photodetector integrated in a commercial CMOS chip. This is the first demonstrated plasmonic effect in Si CMOS. The photocurrent density of a CMOS detector is enhanced three times with a C-shaped nanoaperture. In the future, we envision 3D integration of plasmonic structures on a standard Si chip for more sophisticated optoelectronic functions.

References

1. R. Zia, J. A. Schuller, A. Chandran, and M. L. Brongersma *Materials Today,* v.9, no.7-8, 20-27 (2006).
2. L. Tang, D. A. B. Miller, A. K. Okyay, J. A. Matteo, Y. Yuen, K. C. Saraswat, and L. Hesselink, *Opt. Lett.* **31**, 1519 (2006).
3. L. Tang, S.E.Kocabas, S. Latif, A. Okyay, D. Ly-Gagnon, K. Saraswat, and D.A.B.Miller, *Nature Photon.* **2**, 226–229 (2008) .
4. A. Bhatnagar, S. Latif, C. Debaes, and D. A. B. Miller, *J. Lightw. Technol.*, vol. 22, no. 9, 2213-2217 (2004).

Tuning Coherent Radiative Thermal Conductance in Multilayer Photonic Crystals

Wah Tung Lau, Jung-Tsung Shen, Georgios Veronis, Shanhui Fan

Ginzton Laboratory, Stanford University, Stanford, California, 94305, USA

Recently there has been a lot of interest in exploring coherent thermal transport at nanoscale [1-5]. Most of these studies have exploited phonons as heat carriers, and are restricted at low temperature to avoid strong phonon-phonon interaction in solids [1-3]. Meanwhile, interaction between photons is much weaker, thus coherent transport should occur at higher temperatures. For this reason, here we consider the thermal conductance of a multilayer photonic crystal, consisting of alternating layers of dielectric and vacuum (Fig. 1). Because of the vacuum layers, thermal transport should only be due to photons. With transparent material as the dielectric, the absorption length of photons can be much longer than the crystal periodicity, and hence heat conduction is essentially coherent. Here we show that the band structure significantly affects the thermal conductance of this system.
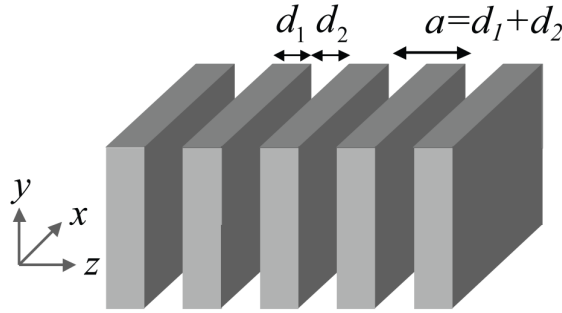
Figure 1: Schematic of the geometry. Layers of lossless silicon slabs of refractive index $n = \sqrt{12}$, thickness d_1 and infinite cross sectional area, are periodically placed with spacing d_2 in vacuum to form a multilayer photonic crystal with periodicity a along the z-direction.

For heat conduction along the z-direction, the coherent radiative thermal conductance per unit area $G(T)$ in three-dimensional systems is [1]:

$$G(T) = k_B \int_0^\infty \frac{d\omega}{(2\pi)^3} \frac{[(\hbar\omega)/(k_B T)]^2 \, e^{(\hbar\omega)/(k_B T)}}{[e^{(\hbar\omega)/(k_B T)} - 1]^2} A(\omega), \qquad (1)$$

where T is the operating temperature. ω is the photon frequency, and $\omega(\mathbf{k})$ is the dispersion relation of the crystal. At a constant frequency, $\omega_0 = \omega(\mathbf{k})$ describes a constant frequency surface in $\mathbf{k}$-space. $A(\omega = \omega_0)$ is the magnitude of the projected area of such constant frequency surface onto the k_x-k_y plane. For vacuum with both polarizations considered, $A_{\text{vac}}(\omega) = 2\pi(\omega/c)^2$. For our structure with cylindrical

symmetry, $A(\omega) \equiv 2\pi \sum_{m,\zeta} \int_{k^{(1)}_{m,\zeta}(\omega)}^{k^{(2)}_{m,\zeta}(\omega)} k_{\parallel} dk_{\parallel}$, where $k_{\parallel}$ is the magnitude of $\mathbf{k}$ along the x-y plane, $k^{(1)}_{m,\zeta}(\omega)$ and $k^{(2)}_{m,\zeta}(\omega)$ are the minimum and maximum $k_{\parallel}$ values of the projected band with index m at ω. $\zeta = s, p$ denotes the s- or p-polarizations and $A(\omega) = A_s(\omega) + A_p(\omega)$. As an illustration, the projected band diagram for s-polarization of the structure with $d_2 = d_1$ is shown in Fig. 2(a) [6]. The photon states in $0 < k_{\parallel} < \omega/c$ are extended in vacuum, while states in $\omega/c < k_{\parallel} < n\omega/c$ are evanescent in vacuum. The regions in $0 < k_{\parallel} < n\omega/c$ with no photon state are the partial photonic bandgaps.

$A_s(\omega)/A_{\text{vac}}(\omega)$ can now be calculated and is plotted in Fig. 2(b). At small ω, there are substantial photon states evanescently coupled through vacuum and $A_s(\omega)/A_{\text{vac}}(\omega) > 1/2$. As ω increases, evanescent coupling strength becomes progressively smaller, while partial bandgaps persist below the vacuum light line in the entire frequency range. Hence $A_s(\omega)/A_{\text{vac}}(\omega) < 1/2$ at large ω. $A(\omega)/A_{\text{vac}}(\omega)$ behaves similarly.
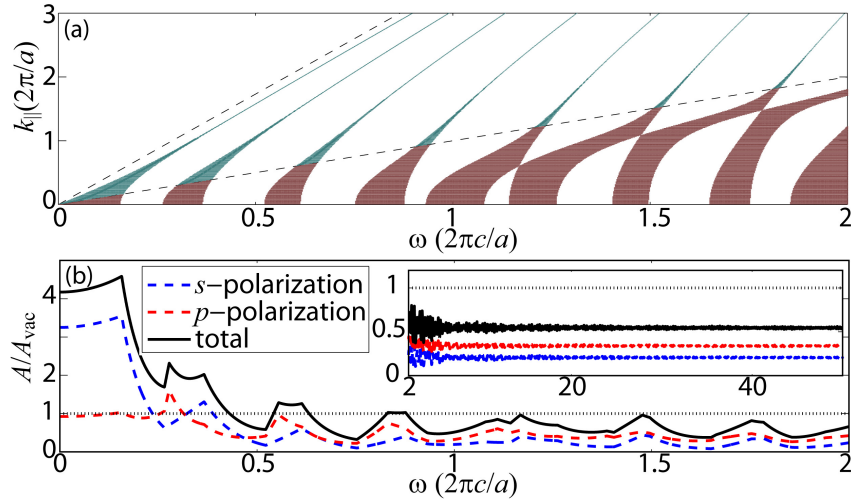
Figure 2. (a) Projected band diagram $(\omega, k_{\parallel}) \backslash$ of s-polarization of the structure in Fig. 1 with $d_2 = d_1$. The bands in $0 < k_{\parallel} < \omega/c$ (brown), and in $\omega/c < k_{\parallel} < n\omega/c$ (green) are separately colored. The vacuum ($\omega/c = k_{\parallel}$) and the material ($\omega/c = nk_{\parallel}$) light-lines are also shown. (b). The black line shows the total normalized projected area $A(\omega)/A_{\text{vac}}(\omega)$ for the same structure in (a), together with the contributions from s- (blue) and p- (red) polarized fields. The vacuum level $A(\omega)/A_{\text{vac}}(\omega) = 1$ is also indicated. The inset shows the result at high frequency.

We can now calculate $G(T)$ for $d_2 = d_1$ using Eq. (1). The result is normalized with respect to the vacuum value $G_{\text{vac}}(T) = (\pi^2 k_B^4 T^3)/(15\text{h}^3 c^2)$, and is shown in Fig. 3 (black curve). At low temperature, photons

populate a small bandwidth of ω where $A(\omega)/A_{vac}(\omega) > 1$, hence $G(T)/G_{vac}(T) > 1$. $G(T)/G_{vac}(T)$ then decreases to below 1 at higher temperature as photons distribute over a larger range of ω where $A(\omega)/A_{vac}(\omega) < 1$. Thus, photonic crystals can be used to generate a medium with thermal conductance below that of vacuum.

Using the same set of dielectric slabs, we can tune the thermal conductance by varying the slab separation at a constant temperature. In Fig. 3, we also plot the results for $d_2 = 9d_1$ and $0.111d_1$. For this range of d_2, thermal conductance generally decreases as d_2 increases. In particular, when the temperature is $T_a = 0.02(hc/k_B d_1)$, the thermal conductance can be tuned by more than an order of magnitude. With silicon as the dielectric, the choice of T_a here corresponds to $287.8K$ when d_1 is $1\mu m$. Thus, such effect is readily observed at room temperature [7].
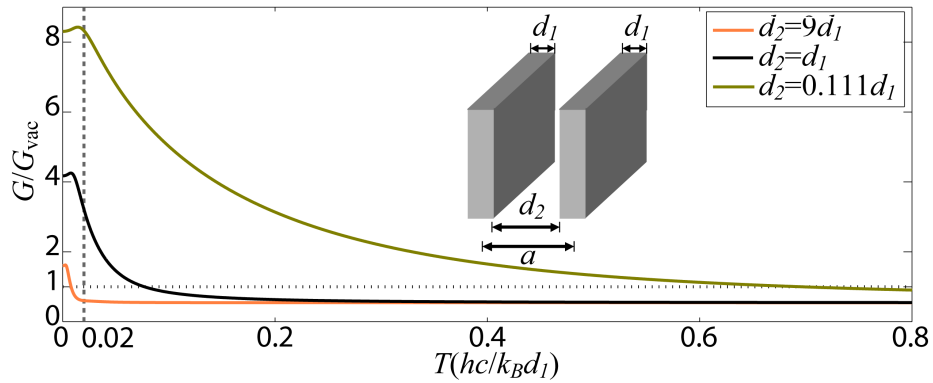
Figure 3: Normalized radiative thermal conductance $G(T)/G_{vac}(T)$ for three structures with constant silicon slab thickness, but different slab separations. The temperature of $T_a = 0.02(hc/k_B d_1)$, where significant variation as a function of d_2 occurs, is indicated as a vertical dashed line. The vacuum conductance $G(T)/G_{vac}(T) = 1$ is shown as a horizontal line. The inset shows the schematic of the structure.

[1] K. Schwab, E. A. Henriksen, J. M. Worlock and M. L. Roukes, Nature (London) **404** 974 (2000).

[2] L. G. C. Rego, and G. Kirczenow, Phys. Rev. Lett. **81**, 232 (1998).

[3] G. Chen, J. Heat Transfer **121** 945 (1999).

[4] M. Meschke, W. Guichard and J. P. Pekola, Nature (London) **444**, 187 (2006).

[5] D. R. Schmidt, R. J. Schoelkopf and A. N. Cleland, Phys. Rev. Lett. **93**, 045901 (2004).

[6] A. Yariv and P. Yeh, *Photonics, Optical Electronics in Modern Communications* (Oxford University Press 6th edition, 2007).

[7] W. T. Lau, J.- T. Shen, G. Veronis, P. Braun, S. Fan, Appl. Phys. Lett. **92**, 103106 (2008).

Integrated photodetectors in
metal slot plasmonic waveguides

Dany-Sebastien Ly-Gagnon, Sukru Ekin Kocabas, David A.B. Miller
Edward L. Ginzton Laboratory, Stanford University, Stanford CA 94305-4088
dalyx@stanford.edu, kocabas@stanford.edu, dabm@ee.stanford.edu

Abstract: We developed a characteristic impedance model to investigate the transmission properties of plasmonic metal slot waveguides. We used this model to design photodetectors integrated in metal slot plasmonic waveguides.

1. Introduction

Metal slot plasmonic waveguides can provide an interesting geometry to design integrated devices with high confinement of the guided mode at infrared wavelengths [1-4]. The performance of such devices depends on the transmission and reflection properties of the integrated waveguide device, which can be calculated with computer-aided tools such as the Finite-Difference Time-Domain (FDTD) method. We investigate the use of a simpler model based on characteristic impedance to characterize the properties of the guided modes in metal slot plasmonic waveguides. Fig. 1 shows a cross section of a metal slot plasmonic waveguide structure, where the region indicated by ε_m is metal, ε_1 and ε_c are both dielectrics. This waveguide supports a bound mode where light propagates in the z-direction (normal to the plane of the figure). We show that a characteristic impedance model can be used to calculate the transmission and reflection properties of such waveguides in the design of complex waveguide structures. We apply this technique in design of a photodetector based on an asymmetric Fabry-Perot resonator embedded in the waveguide.
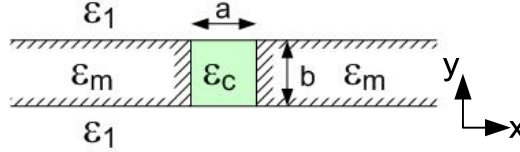
Fig. 1 Metal slot plasmonic waveguide cross section where light propagates in the z-direction.

2. Characteristic Impedance Model

We develop a characteristic impedance model to describe the transmission and reflection properties of the fields as they propagate through a series of different waveguides. We then use a transfer matrix approach to relate the coefficients of the forward and backward versions of the propagating mode, and calculate the transmission and reflection coefficients at each of the discontinuities along the propagation direction.

Considering only the fundamental mode of each waveguide, we build a transmission line model for the propagation of the fields throughout the whole structure. Continuity in the boundary conditions of the tangential electric and magnetic fields reduces to

$$(A_i + B_i) = C_{i,i+1}(A_{i+1} + B_{i+1}) \qquad \text{(1a)}$$

$$\frac{(A_i - B_i)}{Z_i} = C_{i,i+1}\frac{(A_{i+1} - B_{i+1})}{Z_{i+1}}, \qquad \text{(1b)}$$

where A_i and B_i are the amplitudes of the forward and backward propagating modes, respectively, and Z_i is the characteristic impedance of the waveguide. $C_{i,i+1}$ relates to the coupling coefficient at the junction and is calculated with the mode overlap as

$$C_{i,i+1} = \int_S \bar{e}_{i+1} \times \bar{h}_i \cdot \hat{n} \, dS \, , \qquad \text{(2)}$$

where $\bar{e}_i$ and $\bar{h}_i$ are the normalized tangential electrical and magnetic fields, $\hat{n}$ is the propagation direction, and S is the entire cross section of the junction.

At the junction between two waveguide cross sections, a transfer matrix $T_{i,i+1}$ relates the forward and backward propagating modes and is expressed as

$$\begin{bmatrix} A_i \\ B_i \end{bmatrix} = \begin{bmatrix} 1/\tau & \rho/\tau \\ \rho/\tau & 1/\tau \end{bmatrix}\begin{bmatrix} A_{i+1} \\ B_{i+1} \end{bmatrix} = \begin{bmatrix} T(1,1) & T(1,2) \\ T(2,1) & T(2,2) \end{bmatrix} = T_{i,i+1}, \quad (5)$$

where

$$\tau = \frac{2Z_{i+1}C_{i,i+1}^{-1}}{Z_i + Z_{i+1}} \text{ and } \rho = \frac{Z_{i+1} - Z_i}{Z_i + Z_{i+1}} \qquad (6)$$

The impedance of the mode is related to the effective permittivity ε_{eff} and the propagation constant γ by

$$Z_i = \sqrt{\frac{\mu}{\varepsilon_{eff,i}}} = \frac{j\omega\mu}{\gamma_i} \qquad (7)$$

The propagation constant $\gamma = \alpha + j\beta$ is complex in lossy waveguides, and thus the characteristic impedance of the waveguide is also complex for these waveguides. The propagation through a waveguide of length L can be modeled as

$$P_i = \begin{bmatrix} \exp(\gamma L_i) & 0 \\ 0 & \exp(-\gamma L_i) \end{bmatrix}. \qquad (8)$$

Several sections of waveguides can be modeled by a transfer matrix analogous to that of a standard transmission line by alternating junction matrices and propagation matrices as

$$\begin{bmatrix} A_i \\ B_i \end{bmatrix} = T_{i,i+1}P_{i+1}T_{i+1,i+2}P_{i+2}...T_{i+n-1,i+n}\begin{bmatrix} A_{i+n} \\ B_{i+n} \end{bmatrix} = T_{i,i+n}\begin{bmatrix} A_{i+n} \\ B_{i+n} \end{bmatrix}. \qquad (9)$$

Thus, the transmission and reflection properties of an arbitrary waveguide can be calculated from the propagation constants of a given waveguide section.

3. Design of Structures Using the Characteristic Impedance Model

We use the characteristic impedance model to design a germanium-based photodetector at 1.3μm. The cross section of the structure is depicted in Fig.1, with dimensions a x b of 80nm x 80nm. The design consists of an asymmetric Fabry-Perot resonator, using the first piece of germanium as the front reflector and the primary absorbing region, followed by a back reflector that is designed by alternating different elements of germanium with silicon dioxide spacers, nominally in the form of a Bragg reflector structure (see Fig. 2).
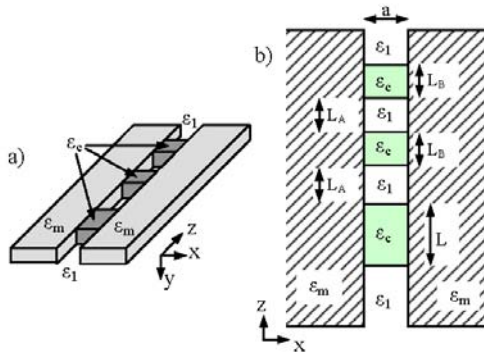
Fig. 2: Asymetric Fabry-Perot structure. a) Perspective view. b) Top view.
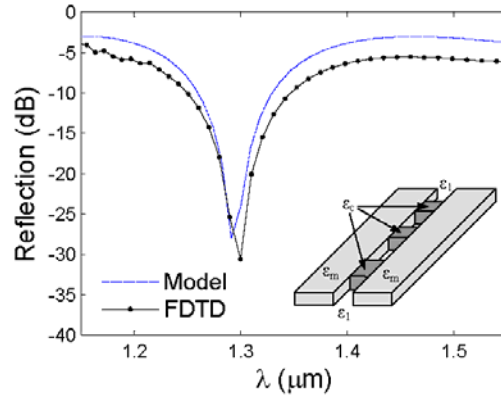
Fig. 3: Reflection at the front surface of the structure

We used SiO2 as the surrounding material, with refractive index of 1.44. At 1.3μm, the germanium has a complex refractive index of $4.23 + 7.8 \times 10^{-2}j$, which corresponds to a power loss absorption coefficient in bulk germanium of $\alpha_G = 7540$ cm^{-1}. The back reflector was designed by considering unit cells of the Bragg reflector structure. The unit cell consists of a cross section with silicon dioxide in the core for a propagation length of L_A, followed by a similar structure but filled in the core with germanium for a propagation length of L_B. The unit cell was designed such that no field would propagate through the entire structure if the unit cell were repeated a large number of times. For the given refractive indices of silicon dioxide and germanium, a length of 190nm for both L_A and L_B would create a Bragg back reflector at 1.3μm. We find that a length L of 260nm would maximize the absorbed power in the first cross section and that less than 1% of the power is reflected. The amount of power reflected from the asymmetric Fabry-Perot as a function of the wavelength is shown in Fig. 3. We note that the model correctly predicts the shape of the reflection spectrum and its minimal value at 1.3μm. FDTD simulations also showed a reflected power of less than 1% at that wavelength. (For simplicity of comparison of the model and the FDTD simulations in Fig. 3, the "germanium" is taken to have the same complex index independent of wavelength.)

The amount of power absorbed in this device by different portions of the structure is shown in Fig. 3 as calculated by the FDTD. There are two loss mechanisms: the loss due to attenuation of the propagating fields in the metal and the absorption in the germanium semiconductor that contributes to photocurrent. The fraction of power absorbed into a given volume can be calculated from the power flowing into this closed surface less the power flowing out of it. At 1.3μm, 30.9% of the power was absorbed in the metal past the front surface. The germanium elements, which represent a volume of 4.1×10^{-3} μm^3 absorbed 69.0% of the total power. The first section of germanium, which consists of a cuboid of 80nm x 80nm x 260nm absorbed 54.1% of the incoming power. Also, the absorption peak occurs at 1.3μm, where the photodetector was designed to operate. Assuming unit internal quantum efficiency, this detector would have a responsivity of 0.72 A/W at 1.3 μm.

Such a device could be fabricated from germanium-on-insulator wafers by first patterning the germanium and subsequently depositing metal with a lift-off process. The two metals stripes on each sides of the germanium could be used to bias the photodetector and create a metal-semiconductor-metal junction. Light could be coupled at the end of the device by a dielectric waveguide or an optical fiber, or by a nanometallic scatterer located close to the waveguide, though such coupling mechanisms remain subject for further investigation.
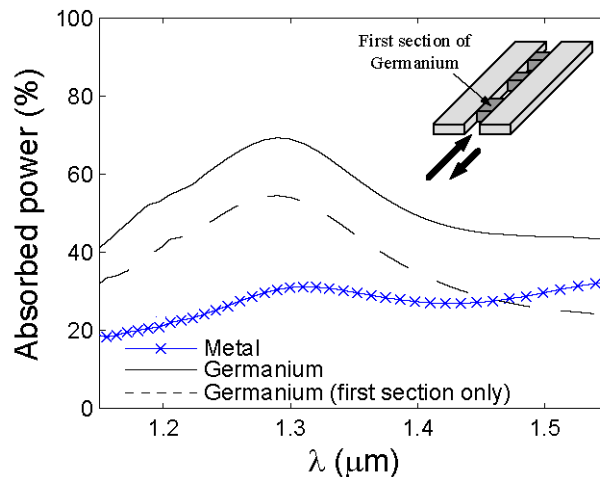
Fig. 4: Absorbed power in the asymmetric Fabry-Perot photodetector.

[1] G. Veronis and S. Fan. "Guided subwavelength plasmonic mode supported by a slot in a thin metal film." *Optics Letters*, 30(24):3359–3361, December 2005.
[2] L. Liu, Z. Han, and S. He. "Novel surface plasmon waveguide for high integration." *Optics Express*, 13(17):6645–6650, August 2005.
[3] J.A. Dionne, H.J. Lezec and H.A. Atwater, "Highly confined photon transport in subwavelength metallic slot waveguides," *Nano Letters*, vol. 6, no. 9, pp. 1928-1932, 2006
[4] R. Zia, M.D. Selker, P.B. Catrysse and M.L. Brongersma, "Geometries and materials for subwavelength surface plasmon modes," *J. Opt. Soc. Am. A*, vol. 21, no. 12, pp. 2442-2446, Dec. 2004.

GALLIUM PHOSPHIDE PHOTONIC CRYSTAL NANOCAVITIES IN THE VISIBLE

Kelley Rivoire, Andrei Faraon, Jelena Vuckovic
Ginzton Laboratory, Stanford University

Photonic crystal nanocavities confine light in ultrasmall volumes, making them ideal for low-power, on-chip optoelectronic devices as well for exploring fundamental light-matter interactions. Although most experimental work in photonic crystal cavities has been done at telecom bands, photonic crystal devices operating in the visible part of the spectrum could serve as light sources and spectroscopic devices operating below 750 nm. Photonic crystal cavities with resonances in the visible could also be coupled to novel light emitters such as nitrogen vacancy centers, fluorescent molecules, and visible colloidal quantum dots.

Operation at visible wavelengths requires different materials from those typically used in photonic crystals like gallium arsenide and silicon because these materials absorb strongly in the visible. Work to date in visible photonic crystals has relied on materials that suffer from lower refractive index[1,2], which limits device quality factors; or require quaternary materials systems[3], which are difficult to grow and process.

In our experiments, we show that photonic crystal devices at visible wavelengths can be fabricated in gallium phosphide. Gallium phosphide is a high refractive index (n=3.25 at 700 nm, n=3.44 at 555 nm at room temperature[4]) III-V semiconductor with an indirect band gap at 555 nm at room temperature.

Linear three hole defect (L3) cavities were simulated and fabricated in a 140 nm thick GaP membrane. Simulation results indicate that quality factors above 10,000 can be obtained for this type of cavity using a triangular lattice of lattice constant a with slab thickness d/a=0.55 and hole radius r/a=0.3. The electric field profile for the fundamental L3 cavity mode is shown in Fig. 1b.

To fabricate structures, the 140 nm thick GaP membrane was grown on a 1 μm thick sacrificial AlGaP layer. Patterns were defined by electron-beam lithography and then transferred into the membrane by dry etching. The sacrificial layer was undercut with hydrofluoric acid to yield suspended membrane structures (Fig. 1b).

The fabricated photonic crystal resonators were probed using a confocal cross-polarized reflectivity measurement[5,6] technique as depicted in Fig. 1a. A vertically polarized (V) probe is directed through a polarizing beam splitter (PBS) and a half wave plate (HWP) onto the photonic crystal cavity, which has a mode that is also vertically polarized (V). The reflected output is observed through the PBS, which acts as a

horizontal (H) polarizer. Rotation of the HWP allows part of the cavity-coupled light to be transmitted at the PBS into the output port with intensity following a sin*(4θ)* dependence (Fig. 1).
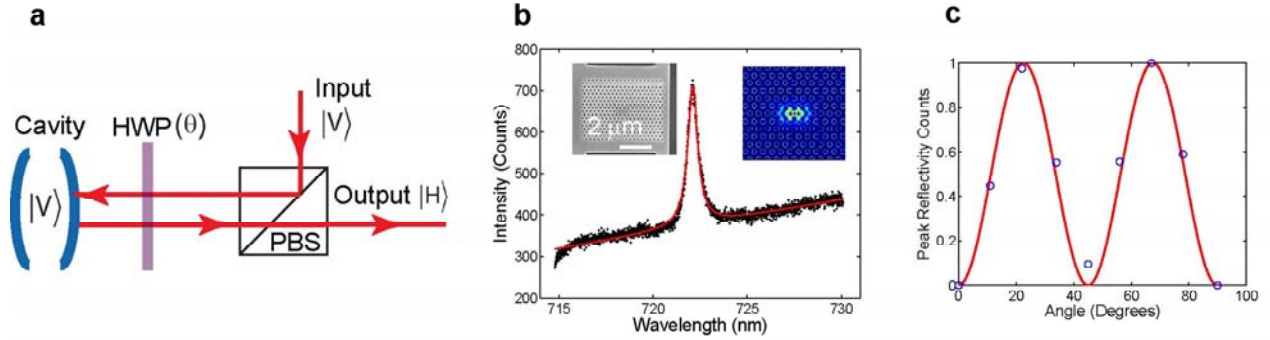
Figure 1: (a) Experimental setup. The V-polarized cavity is probed in a cross-polarized setup using a PBS and a HWP. The cavity signal observed at the output follows a sin(4θ) dependence where θ is the HWP setting (θ=0 corresponds to V polarization). (b) Spectrum of a cavity measured with configuration of Fig. 1a with HWP at θ=67°. A fit to a Lorentzian (solid line) gives Q=1100. Insets show scanning electron microscope image (left) and simulated electric field intensity for the high Q mode (right). (c) (Circles) Normalized counts in cavity peak as a function of HWP angle. (Line) Fit with sin(4θ).

To fabricate cavities with resonant wavelengths spanning a large interval, lattice constant a (210nm<a<246nm) and hole radius (0.25<r/a<0.35) were modified. These changes in the fabrication parameters resulted in cavities with resonances spanning from 645 nm to 750 nm (Fig. 2). The measured resonances have shorter wavelengths than predicted from finite difference time domain simulations (by about 0.05a/λ). We believe this difference may be a result of imperfect selectivity between the sacrificial layer and membrane during the wet etch step, which reduces the membrane thickness. Measured quality factors are between 500 and 1700. This is about one order of magnitude smaller than predicted by simulations because of imperfections introduced in the fabrication process; however, these Qs can still enable a significant Purcell effect, up to 185, as mode volume is only 0.7(λ/n)^3.

The shortest resonant cavity wavelength observed at room temperature was 645 nm with quality factor 610. The resonance wavelength depends on the temperature-dependent refractive index of the membrane. Cooling the sample at 11K in a continuous flow liquid helium cryostat caused the resonance to shift from 645 nm to 641 nm and the quality factor to decrease to 490 as shown in Fig. 2b.
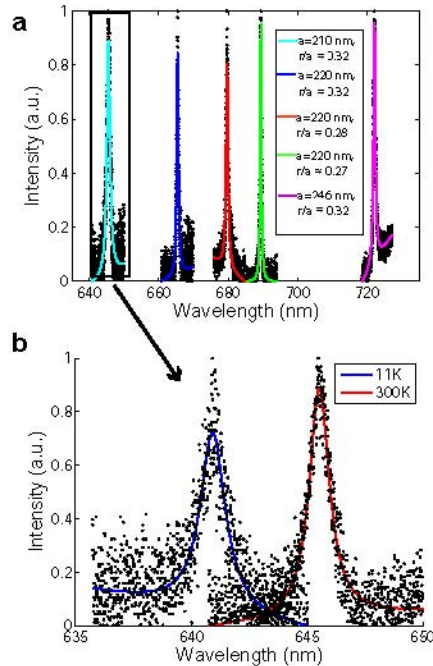
Figure 3: (a) Shift of photonic crystal resonance at room temperature as a and r/a are changed. Solid lines are fits to Lorentzians. (b) Cavity resonance measured at room temperature (blue) and low temperature (red). Solid lines indicate fits to Lorentzians.

In summary, we demonstrate a new gallium phosphide-based materials system for photonic crystals in the visible. We probe linear three-hole defect cavities in reflectivity and observe resonances from 645 nm to 750 nm at room temperature with quality factors as high as 1700.

References:

1. Y. Choi, K. Hennessy, R. Sharma, E. Haberer, Y. Gao, S. DenBaars, S. Nakamura, and E. Hu, Appl. Phys. Lett. **87**, 243101 (2005).

2. M. Makarova, J. Vuckovic, H. Sanda, and Y. Nishi, Appl. Phys. Lett. **89**, 221101 (2006).

3. Z. Zhang, T. Yoshie, X. Zhu, J. Xu, and A. Scherer, Appl. Phys. Lett. **89**, 071102 (2006).

4. D. Nelson and E. Turner, Journal of Applied Physics **39 ,** 3337 (1968).

5. H. Altug and J. Vuckovic, Optics Letters **30**, 982 (2005).

6. D. Englund, A. Faraon, I. Fushman, N. Stoltz, P. Petroff, and J. Vuckovic, Nature. **450**, 857 (2007).

PLANAR LENSES BASED ON NANO-SCALE SLIT ARRAY IN METALLIC FILM

Lieven Verslegers[1], Peter B. Catrysse[1], Zongfu Yu[1], Justin S. White[2], Edward Barnard[2], Mark L. Brongersma[2], and Shanhui Fan[1]

[1] *Ginzton Laboratory, Stanford University*

[2] *Geballe Laboratory, Stanford University*

The miniaturization of lenses has been essential in the development of modern solid-state image sensors and can also have important implications for other opto-electronic applications such as displays, solid state lighting and potentially solar cells. The focusing capability of conventional, dielectric-based microlenses, however, deteriorates as their physical dimensions are reduced towards a single-wavelength scale. Recently, nano-patterning of optically thick metallic films was theoretically proposed as an alternative to achieving refractive lensing. We report the first experimental demonstration of far-field lensing using a plasmonic slit array.

We fabricate the planar nano-slit lens by focused ion beam milling through a thin gold film, deposited on a fused silica wafer (Figure 1a and inset). We illuminate the lens through the fused silica with a wide-area uniform laser beam and we use a confocal scanning optical microscope to map out the focusing pattern (Figure 1b). Figure 1c shows a detailed simulation of the focusing pattern, using a finite-difference
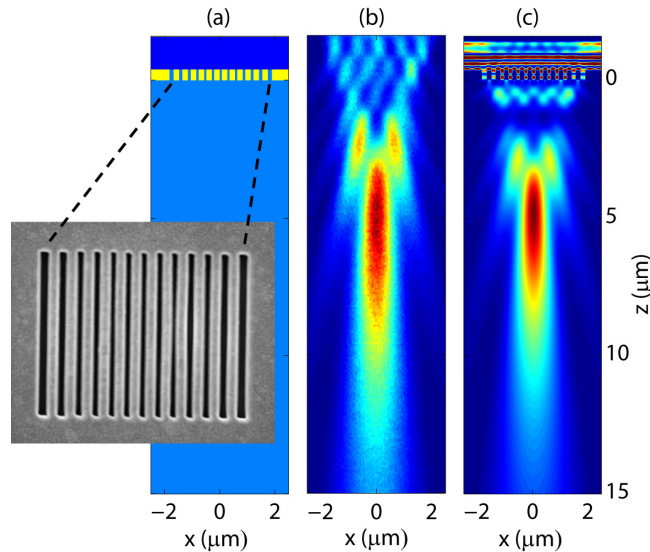
Figure 1: Cylindrical lens with planar geometry based on a nano-scale slit array in a metallic film. (a) Geometry of the lens. It consists of a 400 nm gold film (yellow) with air slits with different widths (80 to 150 nm by 3 um) (light blue) milled therein on a fused silica substrate (dark blue). The inset shows a scanning electron micrograph of the structure as viewed from the bottom. (b) Focusing pattern measured by confocal scanning optical microscopy. (c) FDFD simulated focusing pattern of the field intensity trough the center of the slits.

frequency-domain (FDFD) method. Simulation and measurement are in excellent agreement. Moreover, the simulation image is generated using the designed parameters as the slit width, rather than the actual slit width measured in the SEM. The agreement here thus indicates the robustness in design and the fault tolerance of this approach for focusing.

References

- Z. Sun and H. K. Kim, "Refractive transmission of light and beam shaping with metallic nano-optic lenses", *Appl. Phys. Lett.* **85**, 642 (2004).
- H. Shi, C. Wang, C. Du, X. Luo, X. Dong, and H. Gao, "Beam manipulating by metallic nano-slits with variant widths", *Opt. Express* **13**, 6815 (2005).
- E. N. Economou, "Surface Plasmons in Thin Films", *Phys. Rev.* **182**, 539 (1969).
- P. Ruffieux, T. Scharf, H. P. Herzig, R. Völkel, and K. J. Weible, "On the chromatic aberration of microlenses", *Opt. Express*. **14**, 4687 (2006).

PHOTOACTIVATABLE AND PHOTOSWITCHABLE SINGLE-MOLECULE FLUOROPHORES: DCDHFS AND CY3-CY5 COVALENT DIMER

Samuel J. Lord, Nicholas R. Conley, Hsiao-lu D. Lee, Na Liu, Reichel Samuel,
Robert J. Twieg, W. E. Moerner
Department of Chemistry, Stanford University and Department of Chemistry, Kent State University

Recent advances in optical imaging with single molecules beyond the diffraction limit (e.g., PALM, FPALM, STORM)[1-3] have introduced a new requirement for fluorescent labels: emitters must be actively controlled (usually via photoswitching or photoactivation) to ensure that only a single molecule is switched on at a time in a diffraction-limited region. The location of each of these sparsely distributed molecules is precisely determined, and a super-resolution image is obtained from the summation of many successive rounds of photoactivation. The ultimate spatial resolution is determined by a number of factors, most importantly the total number of photons detected from each individual molecule.
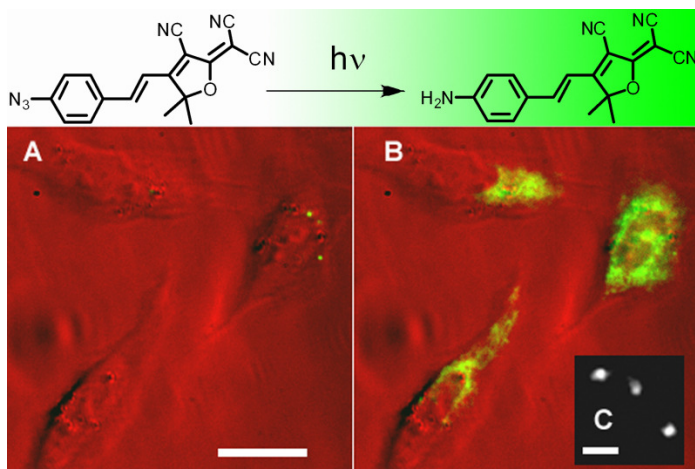
Figure 1. Azido-DCDHFs are photoactivatable. (A) Three cells incubated with azido molecules are dark before activation. (B) The fluorophore lights up in the cells after activation with a 10-s flash of diffuse, low-irradiance (0.4 W/cm^2) 407-nm light. False color: red is the white-light transmission image and green shows the fluorescence images, excited at 594 nm (~1 kW/cm^2). Scalebar: 20 μm. (C) Single molecules of the activated fluorophore in a cell under higher magnification. Scalebar: 800 nm. (Adapted and reproduced with permission from *J. Am. Chem. Soc.* **2008**, *130*, 9204–9205. Copyright 2008 American Chemical Society.)

We have been developing organic fluorophores that can be turned on using a second activating laser. First, we have reengineered a red-emitting dicyanomethylenedihydrofuran (DCDHF) push−pull fluorophore so that it is dark until photoactivated with a short burst of low-intensity violet light.[4] This occurs because the azide disrupts the charge-transfer band of the fluorophore and blueshifts the absorption so that it is no longer

resonant with the imaging laser; photogenerating the amine returns the electron donor–acceptor character and thus the fluorescence. The activated DCDHF fluorophore emits millions of photons before irreversible photobleaching, many-fold more than most photoswitchable fluorescent proteins.[4]
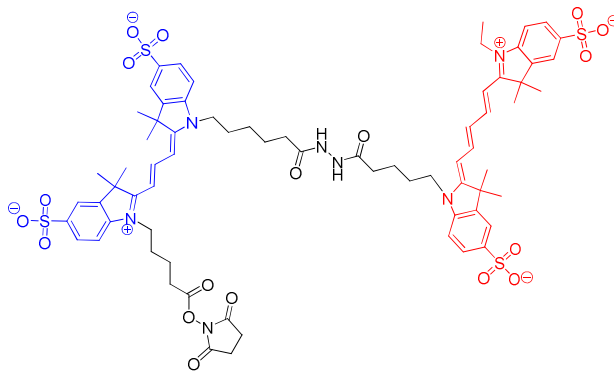
Figure 2. Structure of Cy3-Cy5 covalent heterodimer with NHS ester reactive group.

Photoswitching using some more common fluorophores—the cyanine dyes—is also possible. Proximal Cy3 and Cy5 fluorophores, separated by less than 3 nm, form an optical switch in the presence of a thiol and an enzymatic oxygen scavenging system.[5] Photoexcitation of the Cy5 results in fluorescence emission or, with a much lower probability, causes the Cy5 to enter into a long-lived, but metastable, dark state. Photoinduced recovery of the emissive Cy5 is achieved by excitation of the Cy3 fluorophore at a shorter wavelength. This switch operates for hundreds of cycles and has been demonstrated using other structurally analogous fluorophores.[3]
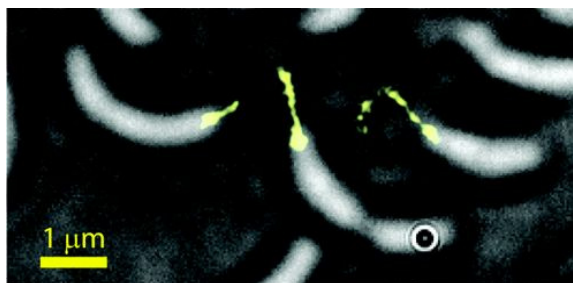
Figure 3. Super-resolution fluorescence image made using the Cy3-Cy5 covalent heterodimer labeling *C. crescentus* stalks (yellow). The 30-nm resolution fluorescence image is superimposed on a white-light image of the cells. The data were acquired over 2048 100-ms imaging frames with 633 nm excitation at 400 W/cm^2. After initial imaging and photobleaching of the Cy3-Cy5 dimers, the molecules were reactivated every 10 s for 0.1 s with 532 nm light at 10 W/cm^2. (Reproduced with permission from *J. Phys. Chem. B.* **2008**, ASAP. Copyright 2008 American Chemical Society.)

Significantly, proximal but not covalently linked Cy3 and Cy5 has found application in stochastic optical reconstruction microscopy (STORM),[3] a technique for super-resolution imaging which requires single-

molecule imaging and photoswitching. However, this method suffers from the drawback that complementary strands of DNA[3, 5] or antibodies[6] must be employed to pair the fluorophores. To provide controllably linked Cy3 and Cy5, we have prepared the discrete Cy3-Cy5 covalent heterodimer that is amine-reactive NHS ester (Figure 2), and we report its photoswitching properties at the single-molecule level *in vitro* and in bacteria.

Cy3-Cy5 covalent heterodimers were prepared from commercially available, reactive cyanine dyes, utilizing the coupling reaction between commercially available fluorophores with hydrazides and NHS esters.[7] The single photoswitching properties of the Cy3-Cy5 heterodimer exhibit controllable reactivation, varying "on" times, and occasional spontaneous recovery from a long-lived dark state. Nonspecific protein labeling of surface lysines with the Cy3-Cy5-NHS provides the opportunity to label cell surfaces in a straightforward way. This molecule was applied to a study of the short, thin stalks of cells of the bacterium *Caulobacter crescentus*. A concentrated suspension of these cells was incubated with Cy3-Cy5-NHS in a growth medium to nonspecifically label the cell surface. The cells were then washed to remove unbound fluorophore, concentrated, resuspended in a growth medium containing a thiol source and an oxygen scavenger, and transferred to an agarose pad containing 1% β-mercaptoethanol. Super-resolution fluorescence images of the Cy3-Cy5-coated *Caulobacter* stalks were obtained by the STORM technique with 30.3 nm resolution (Figure 3).

References

(1) Betzig, E.; Patterson, G. H.; Sougrat, R.; Lindwasser, O. W.; Olenych, S.; Bonifacino, J. S.; Davidson, M. W.; Lippincott-Schwartz, J.; Hess, H. F. *Science* **2006**, *313*, 1642–1645.
(2) Hess, S. T.; Girirajan, T. P. K.; Mason, M. D. *Biophys. J.* **2006**, *91*, 4258–4272.
(3) Rust, M. J.; Bates, M.; Zhuang, X. *Nat. Meth.* **2006**, *3*, 793–795.
(4) Lord, S. J.; Conley, N. R.; Lee, H. D.; Samuel, R.; Liu, N.; Twieg, R. J.; Moerner, W. E. *J. Am. Chem. Soc.* **2008**, *30*, 9204–9205.
(5) Bates, M.; Blosser, T. R.; Zhuang, X. *Phys. Rev. Lett.* **2005**, *94*, 108101-1–108101-4.
(6) Huang, B.; Wang, W.; Bates, M.; Zhuang, X. *Science* **2008**, *319*, 810–813.
(7) Al Jammaz, I.; Al-Otaibi, B.; Okarvi, S.; Amartey, J. *J. Labelled Compd. Radiopharmaceut.* **2006**, *49*, 125–137.

IMPLANTABLE OPTICAL FLUORESCENCE BIOSENSORS FOR MOLECULAR IMAGING

Thomas D. O'Sullivan[1], Elizabeth Munro[2], Adam de la Zerda[3], Natesh Parashurama[3], Ofer Levi[2], Sanjiv S. Gambhir[3], and James S. Harris, Jr.[1]

[1]*Solid State and Photonics Laboratory, Stanford University*
[2]*Institute of Biomaterials and Biomedical Engineering, University of Toronto, ON, Canada*
[3]*Molecular Imaging Program at Stanford, Departments of Radiology and Bioengineering, Bio-X Program, Stanford University*

In vivo molecular imaging is a field which enhances understanding of cellular and molecular pathways and mechanisms of disease by visualizing and quantifying biological processes. The ability to image fluorescence, in particular, is a powerful tool considering the wealth of fluorescent probes/proteins that are used to visualize dynamic *in vivo* processes including the role of stem cells in regeneration, to the dynamics of cancer cell death, to changes in formation of blood vessels (angiogenesis). Current approaches to detect fluorescence *in vivo* rely on devices which use broad area illumination and cooled CCD detectors, generally requiring anesthetized animal models. This limits the usefulness of the technique for long-term, continuous studies [1]. An alternative is to engineer miniaturized fluorescence sensors for direct implantation in freely-moving subjects.

Miniaturized, integrated fluorescence sensors that include an excitation source and emission detector have been demonstrated for *in vitro* lab-on-a-chip applications [2], and could be useful for continuous *in vivo* studies. A major challenge, which limits the sensitivity of these miniaturized sensors *in vivo*, is rejecting the excitation light sufficiently such that weak emission can be detected. Typical large-format fluorescence imagers (such as the IVIS Systems from Xenogen/Caliper Life Sciences, Inc.) utilize high-quality fluorescence filters capable of rejecting excitation light over 6 orders of magnitude (>OD6). It is necessary to achieve at least this level of rejection in miniaturized sensors suitable for *in vivo* applications because of the high fraction of tissue-backscattered light. Researchers have employed several techniques to reject excitation light in integrated fluorescence detectors, including dielectric quarter-wave stacks, semiconductor quarter-wave stacks, and absorption filters [2].These techniques can be aided by the use of a directional source, such as a laser, so that back-reflected light does not directly propagate to the detector, and by designing sensors with physical blocking layers between sources and detectors.

INTEGRATED SENSOR

We have designed and fabricated a GaAs-based fluorescence sensor that includes a 675nm vertical-cavity surface-emitting laser (VCSEL) source, PIN photodiode detector, and dielectric stack emission filter coated on the detector (Fig. 1) suitable for sensing Cy5.5 fluorescent dye. The detector is monolithically integrated

above the VCSEL on a GaAs substrate. We have reduced detector dark current (<100pA at -0.1V bias) by passivating the detector sidewalls with silicon nitride and prevented lateral light leakage by covering the sidewalls with a thick layer of hardened resist and depositing an opaque gold layer (indicated in Fig. 1).
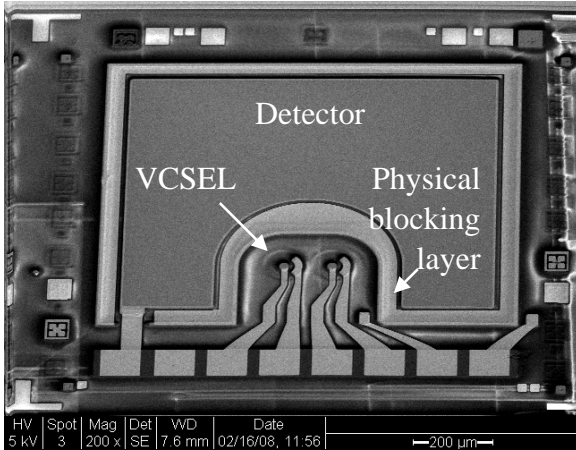
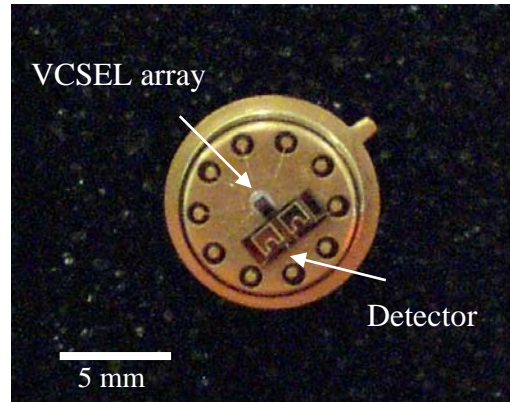**Fig. 1 Integrated fluorescence sensor (dielectric coating is removed for clarity)**

Fig. 2 Hybrid fluorescence sensor

The final steps of processing include patterning for lift-off of an electron-beam evaporated thick (6.89m) dielectric stack notch filter designed to reject excitation light >OD6. While other researchers have successfully deposited dielectric stack filters on silicon integrated fluorescence sensors [3], to our knowledge, there is no published work on coating these thick filters on GaAs. Because the quality of this coating must be extremely high, we are collaborating with a commercial provider of optical coatings (Chroma Technology Corp., Rockingham, VT). Our preliminary experiments have shown that, as expected, deposition conditions for coating fused silica (FS), a common optical filter substrate, are different for successfully coating GaAs substrates. Temperature variations and/or the material sticking coefficient affect the thickness of the individual dielectric layers, causing a shift of the transmission notch. We are presently optimizing the deposition conditions in order to achieve high-quality coatings on GaAs.

HYBRID SENSOR

While work continues on the integrated sensor dielectric coating, we have fabricated a hybrid sensor that incorporates a separate detector with a 675nm VCSEL in a hybrid configuration (figure 2). In this case, we employed a commercially-available fluorescence emission filter (#hq750/40, Chroma Technology, Corp.) diced and bonded directly to the top of the detectors. We have achieved >OD4 excitation rejection at the detector, while the VCSEL emits 1.3mW optical power (figure 3). With this sensor, we have been able to

conduct preliminary *in vitro* and *in vivo* studies on the sensitivity of the device to Cy5.5 fluorescent molecules.
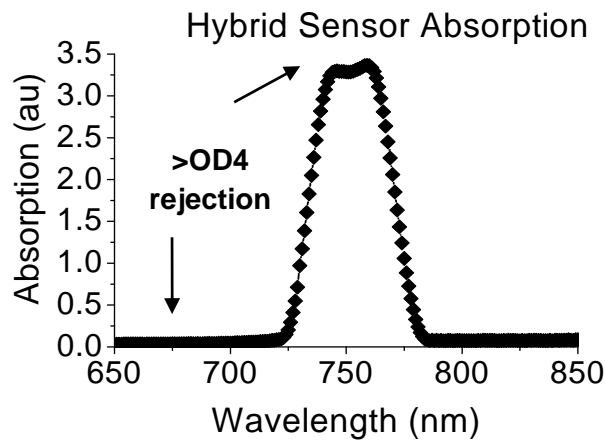
Fig. 3 Absorption spectrum of hybrid sensor
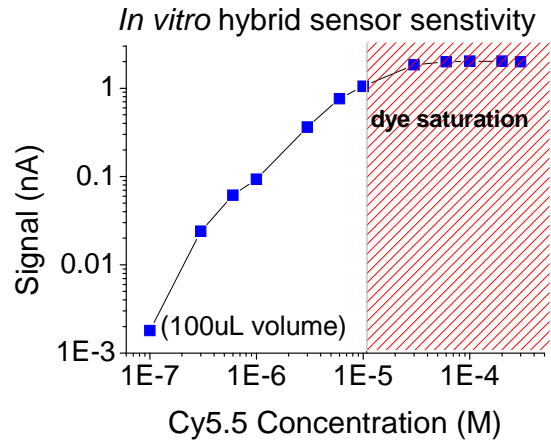
Fig. 4 *In vitro* sensitivity of hybrid sensor to Cy5.5 dye in 100µL volume

The hybrid sensor detects near-IR fluorescent Cy5.5 molecules *in vitro* at 100nM concentration (in a 100µL volume) and linearly for concentrations up to 6µM (figure 4). In a preliminary *in vivo* study, subcutaneously injected dye (1µM Cy5.5 in 50µL) was detected in a nude mouse.

CONCLUSION

We conclude that *in vivo* sensing is possible with these miniaturized sensors. Once we have optimized the dielectric emission filter coating, thus rejecting more excitation light and enabling a truly integrated sensor, sensor sensitivity will increase and we will be able to further decrease the size of the sensor package. This will permit the sensor to be directly implantable in rodent models and employed in continuously-monitored, freely-moving studies. Our future work includes fabricating detector arrays for spatial resolution and using multiple filters for increasing spectral resolution, and allowing the multiplexing of fluorescent molecules.

References

1 O. Levi et al, Appl Optics 46 (2007), 1881-1889.
2 M. Dandin et al, Lab Chip 7 (2007), 955-977.
3 T. Kamei et al, Appl Phys Lett 89 (2006), 114101.

In vivo cellular imaging with MEMS scanners

Hyejun Ra, Wibool Piyawattanametha, Michael Mandella, Christopher Contag, Gordon Kino, and Olav Solgaard

Confocal microscopy can be used for observing biological behavior *in vivo* provided that the objectives and scanning mechanisms can be made sufficiently small for endoscopic implementations. Confocal microscopes enable optical sectioning of tissue with sub-cellular resolution, a level of performance that is not easily approached by other imaging modalities [1]. In order to resolve cellular structures, an axial resolution of a few microns is needed. To achieve this level of resolution, conventional objectives with high numerical apertures (NA) and dimensions on the centimeter scale are typically used. However, a novel dual-axes confocal (DAC) microscope architecture achieves high resolution imaging with low NA lenses (Fig. 1) [2]. By using a MEMS (microelectromechanical systems) scanner as the active imaging device in dual-axes confocal microscopes, real-time *in vivo* imaging can be realized.
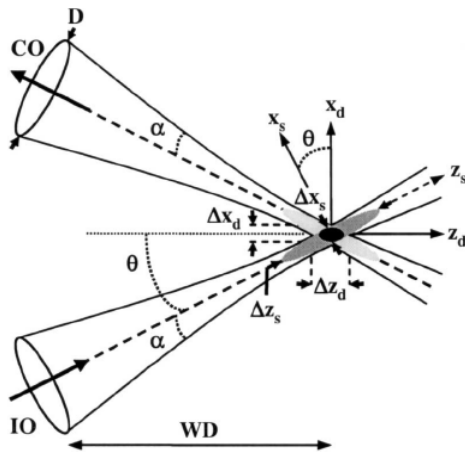
Figure 1: Dual-axes confocal architecture.
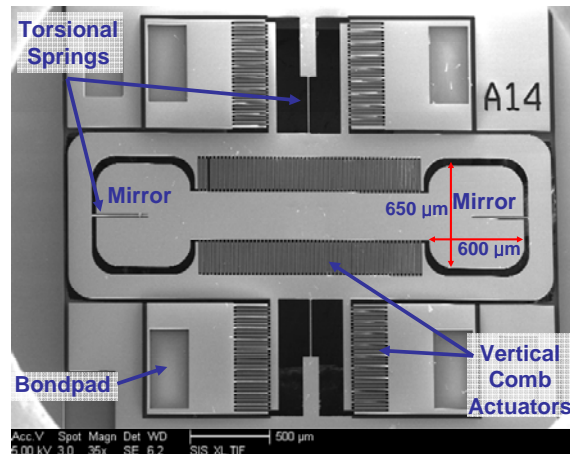
Figure 2: SEM of 2-D MEMS scanner.

Figure 2 shows an SEM of the fabricated 2-D MEMS scanner for DAC microscopy [3]. The scanner is characterized for static deflection and frequency response. Static optical deflections of ±4.8° are achieved at 160 V for the outer axis, and ±5.5° at 170 V for the inner axis. The resonant frequency is 500 Hz and 2.9 kHz for the outer and inner axis, respectively. The scanner performance supports a large field of view (FOV) and fast real-time imaging for the DAC microscope system.

The 2-D MEMS scanner is integrated with miniature optics into a handheld DAC microscope. A diagram of the imaging system is shown in Fig. 3. An optically pumped semiconductor laser at 488 nm wavelength is used as the light source. The laser light is coupled into a single mode fiber (SMF) which collimates the beam using a graded index (GRIN) collimator at the distal end. The collimated beam is focused by a parabolic mirror, reflects off the MEMS scanner, and continues through a

hemispherical lens (HL) into the sample. Signal from overlapping focal volumes within the sample propagates through the other optical branch. The collected photon signal is amplified by a photomultiplier tube (PMT). As the MEMS mirror raster scans the sample, signal from each pixel is collected and displayed on the computer screen as an en face image using a frame grabber and image acquisition software. 3-D volume data is obtained by translating the MEMS scanner in the z (depth)-direction using a computer-controlled piezoelectric actuator. The stack of 2-D *en face* images can later be compiled into a 3-D image. Imaging can be performed in reflectance mode or in fluorescence mode by inserting a long-pass optical filter in the collection path for the latter case.
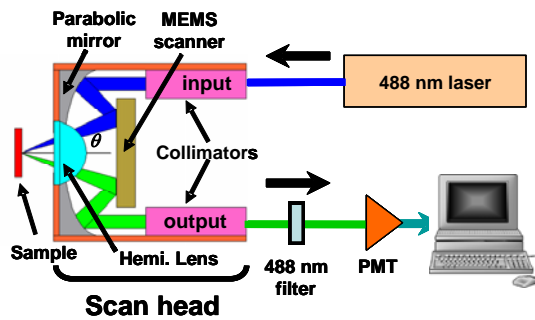
Figure 3: Diagram of the imaging system.

A schematic diagram of the 10 mm diameter imaging head is shown in Fig. 4(a) with a photograph of the MEMS scanner mounted on a printed circuit board (PCB) in the inset. Fig. 4(b) shows the fully assembled handheld probe mounted in an upright position. The probe assembly starts with mounting two fiber-pigtailed GRIN collimators in the two precision machined v-grooves within the housing. Then a pair of Risley prisms is mounted in each v-groove in front of the collimators to adjust for the illumination and collection beams to be parallel. This will ensure that the foci of the two beams will coincide after being focused by the parabolic mirror. The MEMS scanner is separately mounted on a PCB, and wirebonded to the PCB bondpads that are connected to wires running through the middle of the housing. The backplane that holds the PCB is connected to a z-translation stage that is actuated by the closed-loop piezoelectric actuator. Finally, the image head is sealed with UV-curing glue to prevent leakage when imaging live specimen.
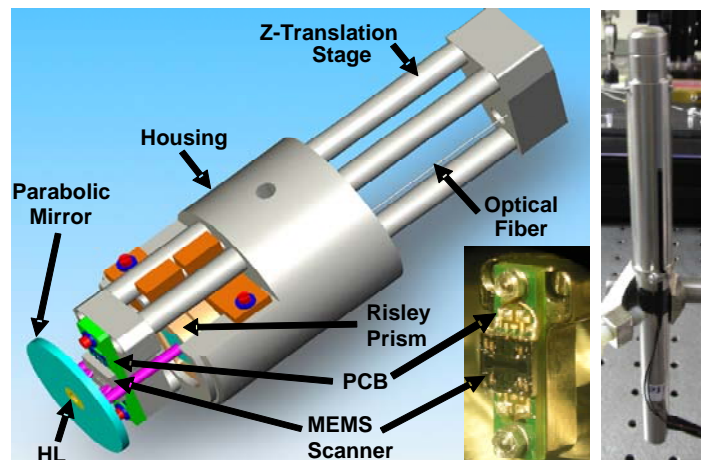
(a)   (b)

Figure 4: (a) Schematic of the 10 mm diameter handheld probe with the packaged MEMS scanner in the inset. (b) Photograph of the fully assembled dual-axes confocal handheld probe.

In vivo imaging was performed on a mouse anesthetized with Avertin with the handheld DAC microscope. Fluorescein isothiocyanate–dextran (FITC-dextran) was injected into the retro-orbital plexus prior to imaging. Imaging was performed by resting the mouse on a stage and placing its intact ear on the hemispherical lens window of the inverted microscope. Figure 5(a) shows a 3-D volume rendering of the image stack obtained by scanning from the surface to 90 μm deep into the tissue. The images were taken in 2 μm intervals in depth with the piezoelectric actuator. All frames were taken at 4 frames per second with averaging of 4 frames. The maximum intensity projected image of the stack is shown in Fig. 5(b). The vessels containing the FITC-dextran solution can be clearly delineated in the image. Since FITC-dextran slowly leaks out of the vessels over time, faint fluorescence signals outside the vessels can also be observed [4].

(a)   (b)
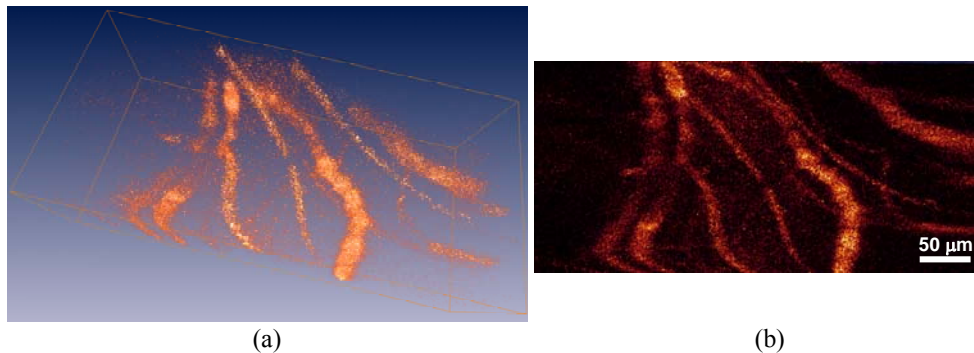
Figure 5: *In vivo* image of blood vessels in an intact mouse ear. (a) 3-D volume rendering. (b) Maximum intensity projected image of the stack.

We have demonstrated a handheld dual-axes confocal microscope operating at 488 nm wavelength for *in vivo* imaging. The microscope is fully packaged and sealed, encasing a MEMS scanner that performs real-time 2-D *en face* imaging. *In vivo* imaging results show that cellular imaging can be performed on living subjects with this microscope to track progression of disease or therapy.

References

[1] J. Pawley, ed., Handbook of Biological Confocal Microscopy, 3rd ed., Plenum, New York (1996).

[2] T. D. Wang, M. J. Mandella, C. H. Contag, and G. S. Kino, "Dual-axis confocal microscope for high-resolution in vivo imaging," *Opt. Lett.* **28**, 414-416 (2003).

[3] H. Ra, W. Piyawattanametha, Y. Taguchi, D. Lee, M. J. Mandella, and O. Solgaard, "Two-Dimensional MEMS Scanner for Dual-Axes Confocal Microscopy," *J. Microelectromech. Syst.* **16**, 969-976 (2007).

[4] H. Ra, W. Piyawattanametha, M.J. Mandella, P. Hsiung, J. Hardy, T.D. Wang, C.H. Contag, G.S. Kino, and O. Solgaard, "Three-dimensional in vivo imaging by a handheld dual-axes confocal microscope," *Opt. Express* **16**, 7224-7232 (2008).

Superresolution Imaging in Live *Caulobacter Crescentus* Cells Using Photoswitchable Enhanced Yellow Fluorescent Protein

Julie S. Biteen[1], Michael A. Thompson[1], Nicole K. Tselentis[1], Lucy Shapiro[2], W. E. Moerner[1]

Departments of Chemistry[1] and Developmental Biology[2], Stanford University

Optical fluorescence microscopy is an important tool for cell biology because light can be used to non-invasively probe a sample with relatively small perturbation of the specimen, enabling dynamical observation of the motions of internal structures in living cells, but with resolution usually limited to ~250 nm by optical diffraction. Single-molecule epifluorescence microscopy achieves nanometer-scale resolution ("superresolution") by taking advantage of the fact that the point spread function (PSF) of an isolated nanoscale emitter can be fit to a precision far greater than the standard diffraction limit, as shown by several groups[1-4]. Several groups demonstrated that photoactivation or photoswitching could be used to maintain the concentration of emitters at the single-molecule level. For example, in photoactivated localization microscopy (PALM)[1], structures labeled by an ensemble of photoactivatable fluorophores too dense to be imaged simultaneously are resolved by repeated cycles in each of which only a sparse subset of the fluorophores is activated. The single molecules are localized to high resolution, and then the final, superresolution image is reconstituted from a superposition of single-molecule positions.

Most of these studies utilized sophisticated photoactivatable fluorophores that are not commonly used in most biology laboratories. We have shown that superresolution imaging can be achieved with fusions to the extremely common Enhanced Yellow Fluorescent Protein (EYFP). In contrast to many of the other photoactivable fluorophores, EYFP matures in a fluorescent state. After apparent photobleaching, the protein can be <u>reactivated</u> with 407 nm pulses[5]. This property leads to the possibility of localizing the same molecule several times. **Figure 1** shows the first evidence of photoinduced EYFP reactivation in live cells. Each frame of this figure shows a single imaging frame where the fluorescence image is superimposed over a negative-contrast white-light transmission image of the *C. crescentus* cell.

 The technique was used to image the prokaryotic actin homologue, MreB, in live *Caulobacter Crescentus* cells. Cultures of a *C. crescentus* merodiploid containing the wild-type *mreB* gene and a single chromosomal copy of a *eyfp-mreB* fusion under the control of a xylose-inducible promoter were incubated in the presence of a xylose concentration selected to produce a high concentration of bright, labeled MreB proteins (~10-100 times greater than needed for isolated single-molecule imaging). At the higher induction
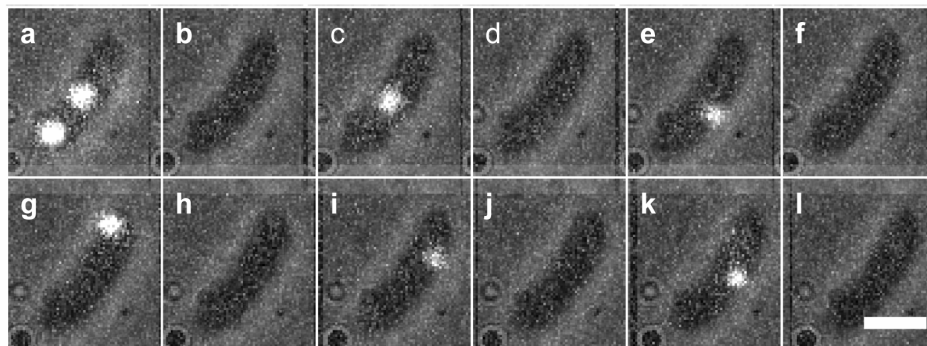
Figure 1. Reactivation of EYFP-MreB fusions in live *C. crescentus* cells. Fluorescence images show single EYFP-MreB molecules (white spots) overlaid on a reversed-contrast white-light image of the cell being examined. (**a**) Initial low-concentration image showing two isolated single molecules. (**b**) The nonemissive form was achieved when all molecules had been under 514-nm excitation for a few seconds. A short 407-nm reactivation pulse was administered after frames (**b**, **d**, **f**, **h**, and **j**), in all of which no molecules are in the emissive state. Reactivated single molecules are observed in corresponding subsequent frames (**c**, **e**, **g**, **i**, and **k**). Scale bar: 1 μm.

level, no altered phenotype of the cells was observed; however, a further 10-fold increase in the xylose concentration yielded altered morphology and non-dividing cells. The sample was illuminated with 514-nm irradiation until the density of emissive fluorophores is at a single-molecule level. This low-concentration sub-ensemble was imaged until all remaining fluorophores bleached, and the single EYFP-MreB positions in each frame were localized and recorded. The imaging was performed at 10 frames/s, a rate at which freely diffusing cytoplasmic EYFP-MreB molecules smeared out and were rendered unobservable[6]. In this fashion, we observed only those EYFP-MreB molecules that were incorporated into a polymerized MreB chain (filament) or other quasi-static structure.

The maximum labeling concentration in live-cell experiments is limited due to changes in the cell morphology at high concentrations of fusion protein; this is an important limit to the resolution of live-cell PALM experiments[7]. However, since the cells are live, the dynamics of MreB monomer treadmilling along filaments in the present experiment were exploited to acquire more positional information for the same number of fluorophores. For this purpose, time-lapse was utilized (**Fig. 2**). In the time-lapse imaging mode, a 0.9-s delay was introduced between each imaging frame, and the sample was only illuminated with 514-nm light during the short acquisition period such that the time to acquire fifty 100-ms frames was lengthened to 50 s. Over this longer time, each activated molecule traced out up to ~300 nm of path along the filaments, so that the distinct localization events elucidated more of the underlying superstructure. In **Figure 2,** results from TL- imaging of EYFP-MreB in *C. crescentus* are presented. Two distinct MreB superstructures were identified in the cells: a quasi-helical arrangement in a stalked cell (**Figs. 2a** and **2b)**

and a midplane ring in the predivisional cell (**Figs. 2c** and **2d**). These images clearly show a continuous structure that can only be resolved using time-lapse to obtain a higher effective labeling concentration.
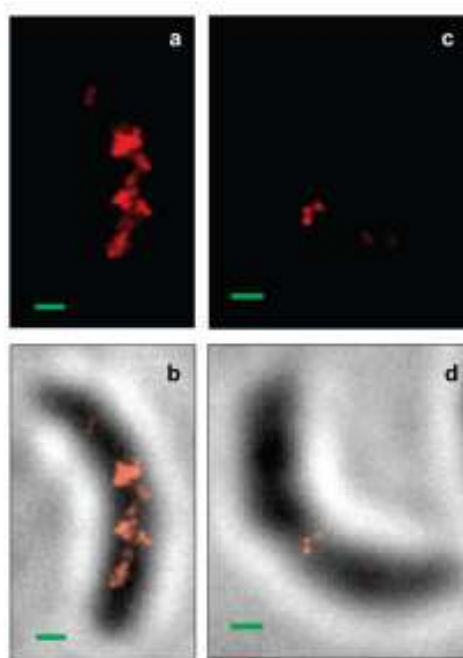

Figure 2. TL-SMACM images of EYFP-MreB in *C. crescentus* cells showing fewer punctuate spots than continuous-acquisition SMACM. (**a**, **b**) Quasi-helical structure in a stalked cell. (**c**, **d**) Midplane ring in a predivisional cell. The SMACM images in (**b** and **d**) are overlaid on a reversed-contrast white-light image of the cell. Scale bar: 300 nm.

References

1.   Betzig, E. *et al*. *Science* **313**, 1642-1645   (2006).

2.   Rust, M. J., Bates, M. & Zhuang, X. *Nature Meth.* **3**, 793-795 (2006).

3.   Hess, S. T., Girirajan, T. P. K. & Mason, M. D. *Biophys. J.* **91**, 4258-4272 (2006).

4.   Geisler, C. *et al*. *Appl. Phys. A* **88**, 223-226 (2007).

5.   Dickson, R. M., Cubitt, A. B., Tsien, R. Y. & Moerner, W. E. *Nature* **388**, 355-358 (1997).6.

6.   Kim, S. Y., Gitai, Z., Kinkhabwala, A., Shapiro, L. & Moerner, W. E. *Proc. Nat. Acad. Sci. (USA)* **103**, 10929-10934 (2006).

7.   Shroff, H., Galbraith, C. G., Galbraith, J. A. & Betzig, E. *Nature Meth.* **5**, 417-423 (2008).

One-Way Electromagnetic Waveguide Formed at the Interface between a Plasmonic Metal under a Static Magnetic Field and a Photonic Crystal

Zongfu Yu[1], Georgios Veronis[1], Zheng Wang[2] and Shanhui Fan[1]
[1]Stanford University, Stanford, California, 94305
[2]Massachusetts Institute of Technology, Cambridge, Massachusetts, 02139

One-way electromagnetic waveguide modes are theoretically demonstrated. A one-way waveguide provides a fundamental way to eliminate the effects of disorders. It also modifies the fundamentals of waveguide-cavity interaction [1].

Back reflection caused by disorders scattering is worrisome for nanophotonic devices, particularly for slow slight applications. In systems with broken time-reversal symmetry, the effect of disorders can be suppressed with the use of a *one-way* waveguide. Such a waveguide supports a single forward propagating mode in a given frequency range, while having neither radiation nor backward propagation modes in the same range. Here we present a novel design of such a one-way waveguide formed between a semi-infinite photonic crystal (PC) structure and a semi-infinite metal region with infinitesimal loss. The metal is assumed to be a free-electron plasmonic metal under a static magnetic field along the direction perpendicular to the plane of propagation (Fig. 1a).
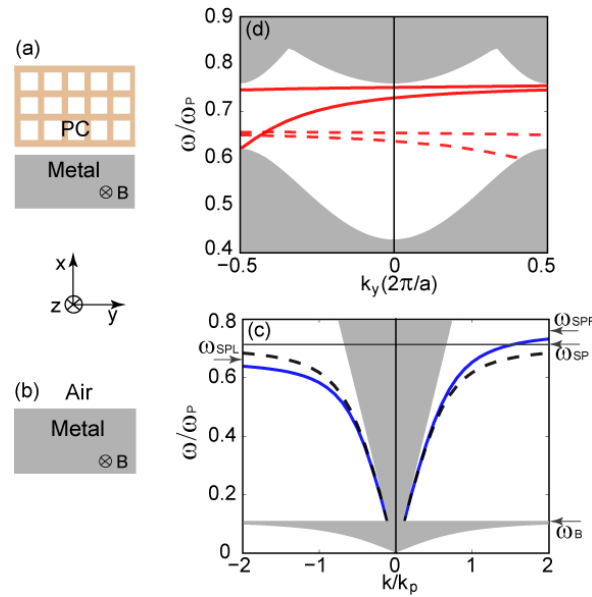
Fig. 1 Structure (a) and dispersion relation (d) of one-way waveguide. Structure (b) and dispersion relation (c) of magnetized metal-air interface. Grey regions represent radiation modes.

The design of a one-way waveguide in such structure relies upon the one-way properties of surface plasmon modes at the metal-air interface [3]. In the presence of static magnetic field B in the z direction (Fig. 1b), the cutoff frequencies ω_{SPL} and ω_{SPR} of the left and right propagating surface modes respectively are no longer degenerate, and instead split around $\omega_{SP} \equiv \dfrac{\omega_P}{\sqrt{2}}$, where ω_p is the bulk plasmon frequency.

Within the frequency range $\omega_{SPL} < \omega < \omega_{SPR}$, surface plasmon can only propagate in one direction (Fig. 1c

blue lines). An exact one-way waveguide, thus, can be created by placing the metal in close proximity to a photonic crystal such that the frequency range $\omega_{SPL} < \omega < \omega_{SPR}$ falls within the photonic band gap. The gap serves the purpose of eliminating all radiation modes in this frequency range. By choosing the truncation to ensure that the crystal does not support any surface mode at the air-crystal interface, and by placing the photonic crystal close to the metal surface, one can ensure that the overall structure forms a single mode one-way waveguide with its photonic band-structure shown in Fig. 1d. In the frequency range $[0.66\omega_P, 0.76\omega_P]$ there are propagating modes along the $+y$ direction but no modes in the opposite direction.

The transport properties of above one-way waveguide are investigated with the finite-difference frequency-domain (FDFD) method. To simulate the effect of disorders scattering suppression, we place metallic particles in the middle of the waveguide (Fig. 2 inset). In the absence of external magnetic field ($\omega_B = 0$), the waveguide is reciprocal and the metallic particle causes significant back-reflection. In contrast, in the presence of an external magnetic field ($\omega_B = 0.1\omega_P$), in the frequency range $[0.66\omega_P, 0.76\omega_P]$, no back-reflection is observed. The absence of back-reflection is independent of the specific properties of the scatterers. For example, we see no observable differences in this frequency range as we vary the number of particles placed in the waveguide.
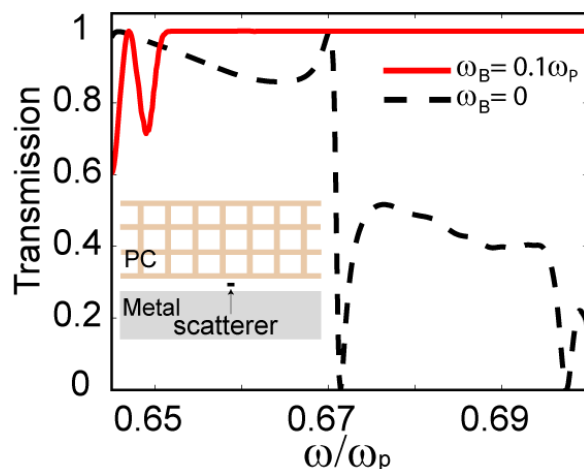
Fig.2 Transmission spectra of one-way waveguide in presence of a scatterer.

The use of a one-way waveguide also fundamentally alters the properties of waveguide-cavity interaction, which is at the heart of many integrated photonic devices. As an example, we consider the properties of side-coupled tunneling between two waveguides through a singly degenerate localized state (Fig. 3a). In these systems, an incident wave (port 1) in the waveguide excites the resonance, which then decays into both waveguides, resulting in a frequency-selective coupling between the waveguides. In the case of reciprocal waveguides, the resonator decays into both the forward and backward directions of each waveguide (Fig. 3b). Consequently at resonance there is always significant reflection. Also the transfers occur to both directions of the output waveguides (ports 3 and 4). In contrast, in the case of one-way waveguides, the resonator decays only into a single direction into each of the waveguides. Consequently, not only is the reflection fundamentally suppressed, but also at resonance complete transfer occurs to only

a single direction of the output waveguides. Hence the structure should allow complete channel add/drop tunneling using surface plasmon waves with a single-mode resonator. Since in a reciprocal system, the resonator needs to support at least two modes to allow for complete channel add/drop transfer [3], the use of one-way waveguides fundamentally alters the waveguide-cavity interaction. Fig 3b shows the complete photon tunneling from port 1 to port 3 with two one-way waveguides. Notice that when the magnetic field directions between the two metal regions are the same, the two waveguides have opposite propagation directions due to their orientations.
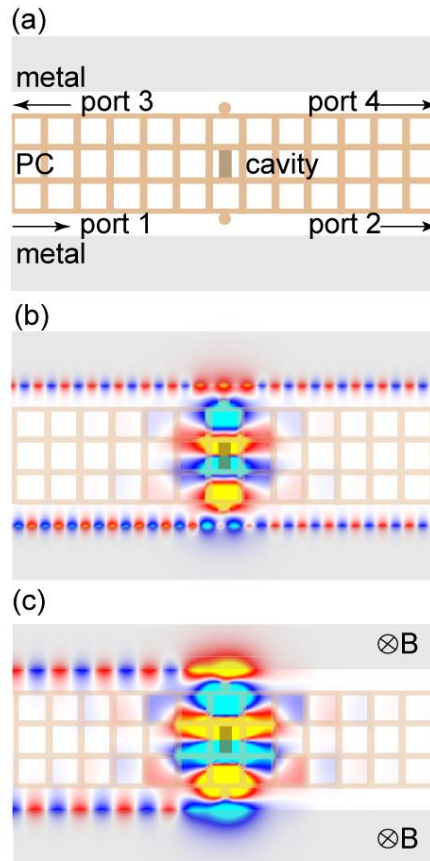
Fig.3 Channel drop tunneling of photons through a singly degenerate localized resonant state. (a) Simulated structure. (b) (c) Field profiles at resonant frequency .

Finally, the bandwidth of one-way propagation is proportional to the amplitude of the external magnetic field. Assuming a static field of 1 Tesla, the one-way frequency range is 28 GHz. Such a bandwidth is sizable in the optical wavelength range.

Reference:
[1]Z. Yu, G. Veronis, Z. Wang, and S. Fan, Phys. Rev. Lett. **100**, 023902 (2008).
[2] R. E. Camley, Surf. Sci. Rep. **7**, 103 (1987).
[3] S. Fan, P. R. Villeneuve, J. D. Joannopoulos, and H. A. Haus, Phys. Rev. Lett. **80**, 960 (1998).

JOINT COMPENSATION OF LINEAR AND NONLINEAR FIBER IMPAIRMENTS USING DIGITAL BACKPROPAGATION

Ezra Ip, Joseph M. Kahn
Ginzton Laboratory, Stanford University

Introduction

Transmission in optical fiber is impacted by linear and nonlinear impairments. Linear impairments include chromatic dispersion (CD) and polarization mode dispersion (PMD), and can be compensated with low power penalty using a two-dimensional fractionally spaced equalizer [1]. Nonlinear impairments arise from Kerr nonlinearity, with self-phase modulation (SPM), cross-phase modulation (XPM), four-wave mixing (FWM) and nonlinear phase noise (NLPN) being well-known effects. Digital backpropagation (BP) is a universal algorithm that can jointly compensate linear and nonlinear impairments [2]. In the absence of noise, it can invert SPM, XPM and FWM which are deterministic effects, while in the presence of noise, it can partially mitigate NLPN which is non-deterministic.

Receiver
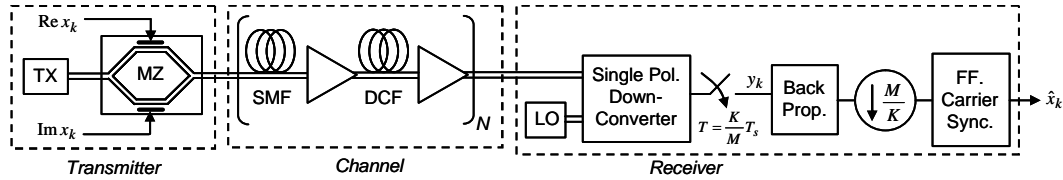
Figure 1. Transmission Model.

We assume single polarization transmission over a channel consisting of N spans of single mode fiber (SMF), with inline amplification and dispersion compensating fiber (DCF) after each span. The receiver has a single polarization downconverter whose output is sampled at a rate equal to M/K times the symbol rate, M and K being integers. A digital signal processor (DSP) performs digital BP at the oversampled rate. After downsampling, feedforward carrier recovery is performed, yielding symbol estimates $\hat{x}_k$.

Digital Backpropagation

When PMD is negligible, signal propagation can be modeled by a scalar nonlinear Schrödinger equation (NLSE) along the reference polarization of the fiber:

$$\frac{\partial E}{\partial z} = jg|E|^2 E + \left(-j\frac{b_2}{2}\frac{\partial^2}{\partial t^2} - \frac{a}{2}\right)E = \left(\hat{N} + \hat{D}\right)E \,, \tag{1}$$

where a, b_2 and g are the loss, chromatic dispersion and nonlinear parameters of a fiber section. In the absence of noise, we can estimate the transmitted waveform by computing the reverse NLSE from the digital samples of the downconverter. The reverse NLSE is the same as (1), but with parameters having opposite signs. The NLSE is typically solved by breaking a fiber into sections, and then solving (1) for each section using an iterative procedure called the symmetric Split-Step Fourier Method (SSFM). Since nonlinear effects are strongest at the beginning of a fiber span where signal power is highest, we can use a numerically simpler non-iterative asymmetric approximation (Fig. 2), where a fiber is modeled as the concatenation of a nonlinear phase rotation followed by a linear section. The parameter $0 < z < 1$ is a degree of freedom that is optimized empirically.
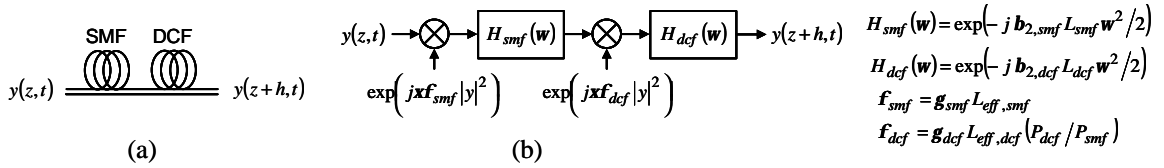
Figure 2. (a) One transmission span, (b) Mathematical model for simplified BP.

We simulated the performance of BP for 21.4 Gb/s RZ-QPSK transmitted over 25×80 km spans of SMF. The amount of CD under-compensation per span is varied by changing the length of the DCF. Fig. 3 shows our results. The best performance is obtained at 100% CD under-compensation (omitting DCF), because (i) DCF incurs loss and nonlinearity while performing an operation that can be done losslessly by a DSP, and (ii) dispersion reduces nonlinear interactions between the signal and out-of-band noise in a manner similar to XPM walkoff. Significant performance improvement is obtained at an oversampling ratio of $M/K \geq 3$ owing as the nonlinear operator being third-order in electric field. Using the design guide of no DCF and $M/K = 3$, we simulated system performance versus transmission distance in Fig. 4, comparing our non-iterative asymmetric SSFM algorithm with the iterative symmetric SSFM algorithm (10 sections per fiber span) considered in [4]. Although simplified BP performs worse by 2 dB, it requires fewer operations, while still achieving a bit-error ratio below 10^{-3} ($s_e < 0.23$ rad) at a transmission distance of 6,400 km. A receiver that compensates CD only using a two-polarization linear equalizer can only transmit 2,000 km.
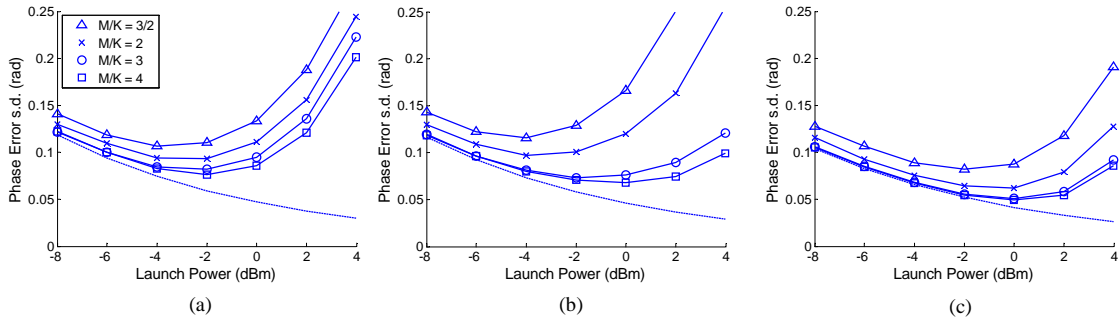
Figure 3. Simulated performance of BP for RZ-QPSK transmitted over 25×80 km of SMF, with (a) 0%, (b) 10%, and (c) 100% CD undercompensation per span.
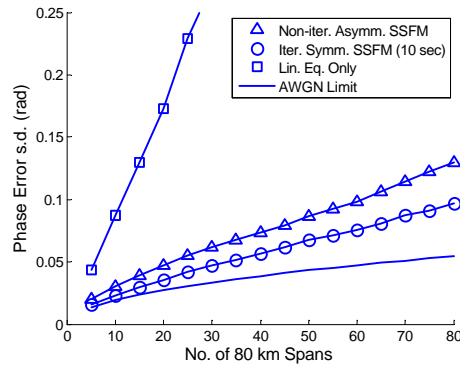

Figure 4. Performance vs transmission distance for different receiver algorithms.

Conclusion

Digital backpropagation can jointly compensate linear and nonlinear impairments in fiber, and significantly outperforms linear equalization only.

References

- E. Ip and J. M. Kahn, "Digital Equalization of Chromatic Dispersion and Polarization Mode Dispersion", *J. of Lightwave Technol.* **25**, 2033- 2043 (2007).
- X. Li, X. Chen, G. Goldfarb, I. Kim, F. Yaman and G. Li, "Electronic post-compensation of WDM transmission impairments using coherent detection and digital signal processing", *Opt. Express* **16**, 880- 888 (2008).

THERMAL LOADING OF OPTICAL RESONATORS FOR FUTURE GRAVITATIONAL-WAVE DETECTORS

Amber L. Bullington, Robert L. Byer
Ginzton Laboratory, Stanford University

Long baseline interferometric detectors such as LIGO, the Laser Interferometer Gravitational-wave Observatory, are being commissioned around the world to detect gravitational waves. The upgrade to LIGO (Advanced LIGO) calls for a 200 W laser, resulting in maximum resonant circulating power in the interferometer of 800 kW. A Fabry-Perot ring cavity, known as a modecleaner, has been designed with a calibrated absorption loss to measure the effects of high circulating power similar to what will be observed in resonant systems for Advanced LIGO. A modecleaner schematic is shown in Figure 1. Results have shown that thermal distortion of the cavity's optics leads to frequency degeneracy of higher-order spatial modes with the fundamental mode, decreased power transmission, and thermally-induced power fluctuations. Remaining below the threshold for thermal effects is important for the design of a modecleaner for Advanced LIGO whose purpose is to provide frequency and spatial filtering of the input beam to the interferometer.
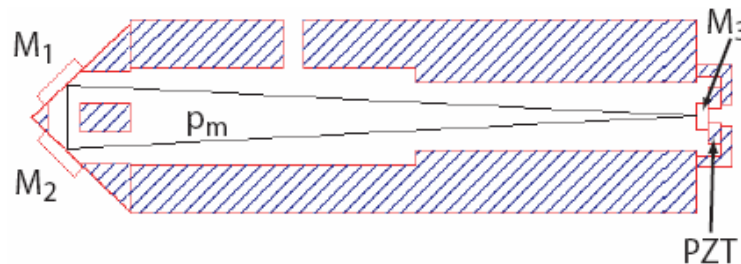

Figure 1: (a) A schematic of a Fabry-Perot ring resonator (modecleaner) is shown. M_1 and M_2 are 1 inch in diameter, and M_3, attached to a piezoelectric transducer (PZT), is 0.5 inch in diameter with a 1-m radius of curvature. Round-trip perimeter, p_m, is 42 cm.

Absorption in the optical coatings and the resulting deformation of an optic's surface is the dominant thermal effect in a modecleaner. To achieve coating absorption comparable to Advanced-LIGO thermal load with available laser power, dielectric-coated optic M_3 has a slightly transmissive coating on a highly absorbing substrate, allowing the leakage power to act as a calibrated absorption. This modecleaner under test is known as the absorbing modecleaner. A low-finesse, non-thermally loaded modecleaner filters the high-power beam to provide a spatially clean fundamental mode. Transmitted power from this modecleaner is increased incrementally, and both cavities are locked to resonance via the Pound-Drever-

Hall technique. A third modecleaner, known as the mode analyzer, filters the transmission of the thermally loaded modecleaner to analyze the beam's spatial mode content. The experimental layout is shown in Figure 2. The modecleaner's configuration allows locking to either p- or s-polarized light each with different cavity finesse since the different polarizations do not resonate simultaneously.
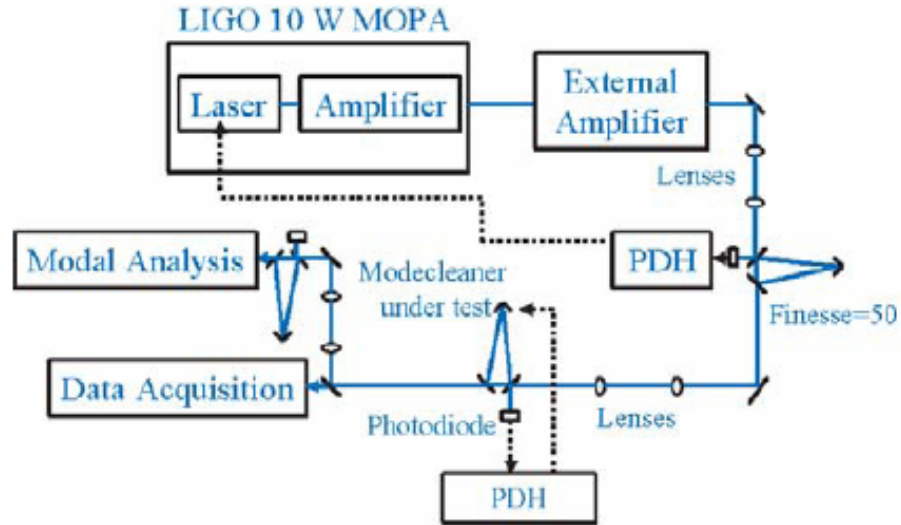

Figure 2: The experimental layout for testing a Fabry-Perot ring resonator (modecleaner) under thermal load is shown. A finesse-of-50 modecleaner filters the 30 W Master Oscillator Power Amplifier (MOPA) system via the Pound-Drever-Hall (PDH) locking technique to provide a spatially clean input beam to the cavity to be tested under thermal load. Output from the thermally loaded modecleaner is subsequently transmitted to an identical modecleaner for analyzing modal content. The distorted transmission is also analyzed for power variation via a data acquisition system.

Transmitted beam quality is degraded by coupling of power to higher-order modes that become frequency-degenerate with the fundamental mode. Higher-order mode frequencies shift from increasing thermal deformation at a greater rate than the fundamental-mode frequency. As absorbed power increases, this modal frequency degeneracy diminishes the fundamental-mode content necessary for detecting a gravitational-wave signal. Beyond a particular power absorption, linearly increasing transmission with input power is no longer achieved as higher-order modal content rapidly degrades the beam quality. With a p-polarization finesse of 330, the absorbing modecleaner shows the first higher-order modal degeneracy at 9 mW of absorbed power with significant decline in transmission beyond absorption of 40 mW. Figure 3 shows images of the thermally loaded modecleaner's transmitted beam for absorption greater than 40 mW and subsequent filtering by the mode analyzer cavity identifying the degenerate higher-order mode as LG_{12}. Steady transmission is not achieved beyond absorbed powers greater than 47 mW, when a thermally dependent periodic-power fluctuation causes the transmitted power to vary by as much as 75 % at frequencies ranging from 14 Hz to 30 Hz. When the absorbing modecleaner is locked with an s-polarization

finesse of 5500, overlap of multiple higher-order modes with the fundamental mode begins at 4 mW of absorbed power with strong fundamental-mode degradation for increasing absorption. The fundamental-mode content of the transmitted beam drops to as low as 57 % at 12 mW of absorbed power.
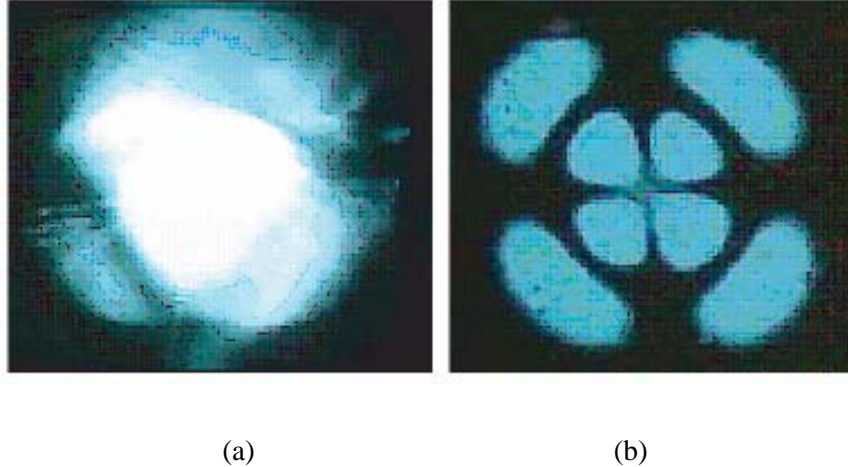

(a)   (b)

Figure 3: Images (a) and (b) show the absorbing modecleaner's transmitted beam and resultant filtering via the mode-analyzer cavity at 47 mW of absorbed power.

The 200 W Advanced-LIGO laser must be filtered without the detrimental effects of thermal loading. Scaling results of this experiment to low-loss fused silica substrates with 1 ppm absorptive coating loss suggests that the Advanced-LIGO modecleaner's finesse should not exceed 100. This ensures that the absorption remains at least a factor of three below the higher-order mode coupling threshold. Predictions of modal frequency degeneracy for Advanced LIGO show that the first degenerate higher-order modes occur for a coating absorption of only 0.34 ppm at 800 kW of circulating power. Compensation of thermal profiles on the mirrors will be necessary to elevate this low modal frequency degeneracy threshold.

References

- A. Abramovici, W. Althouse, R. Drever, Y. Gursel, S. Kawamura, F. Raab, D. Shoemaker, L. Sievers, R. Spero, K. Thorne, R. Vogt, R. Weiss, S. Whitcomb, and M. Zucker, "LIGO: The Laser Interferometer Gravitational-wave Observatory," Science, 256, 325-333 (1992).
- R. W. P. Drever, J. L. Hall, F. V. Kowalski, J. Hough, G. M. Ford, A. J. Munley, and H. Ward, "Laser Phase and Frequency Stabilization Using an Optical Resonator," Appl. Phys B 31, 97-105 (1983).

RPE PPLN Waveguides for Parametric Temporal Imaging

Derek Chang, Carsten Langrock, Martin M. Fejer

Ginzton Laboratory, Stanford University

Modern ultrafast laser systems can generate optical pulses as short as a few cycles [1]. Many measurement techniques have been developed to record these signals [2, 3], however, they require sampling of repetitive signals or have significant limitations on the total length of time and complexity of the signal that can be recorded.

Temporal imaging is a waveform manipulation technique that can expand or compress a signal while preserving the overall shape of its envelope profile. An ultrafast waveform can be slowed down (or stretched) to a time scale that can be measured by conventional equipment such as a photodiode or oscilliscope. Temporal imaging is based on the spacetime duality between paraxial diffraction and narrowband dispersion which was first described by Akhmanov [4]. The functional forms of the equations describing diffraction and dispersion are identical in that diffraction in space is analogous to dispersion in time: the transverse spatial coordinates in diffraction correspond to the time coordinate in dispersion. Spacetime duality has lead to the useful concept of temporal magnification, developed in 1971 by Caputi [5]. Just as a thin, optical lens adds a quadratic phase shift in space to an incoming field, a time lens imparts a quadratic phase shift in time onto a temporal waveform. As a result, a temporal imaging system can magnify/demagnify an input waveform like a spatial imaging system magnifies/demagnifies an image. Just as an optical imaging system has a spatial resolution limit, the temporal imaging system has a minimum resolvable temporal feature size of $\delta\tau_{min} = 1/\Delta f$, where Δf is the bandwidth of the imaging system. The time lens must impart a certain bandwidth onto the input waveform to achieve the desirable resolution. Due to limited modulation bandwidth, a temporal imaging system based on electrooptic modulation cannot achieve a very high resolution [6].

Another method to impart quadratic phase utilizes parametric interactions inside a nonlinear medium [7, 8]. A linearly chirped pump pulse (quadratic phase) is mixed with the signal waveform to be magnified. The quadratic phase of the pump is transferred to the signal via sum-frequency or difference-frequency generation (SF/DF). Using linearly chirped aperiodically poled lithium niobate (A-PPLN) waveguide devices, the bandwidth of the quasi-phasematched (QPM) interaction can be chosen independently from the length of the nonlinear medium, increasing the conversion efficiency significantly compared to bulk PPLN devices with a uniform QPM grating.
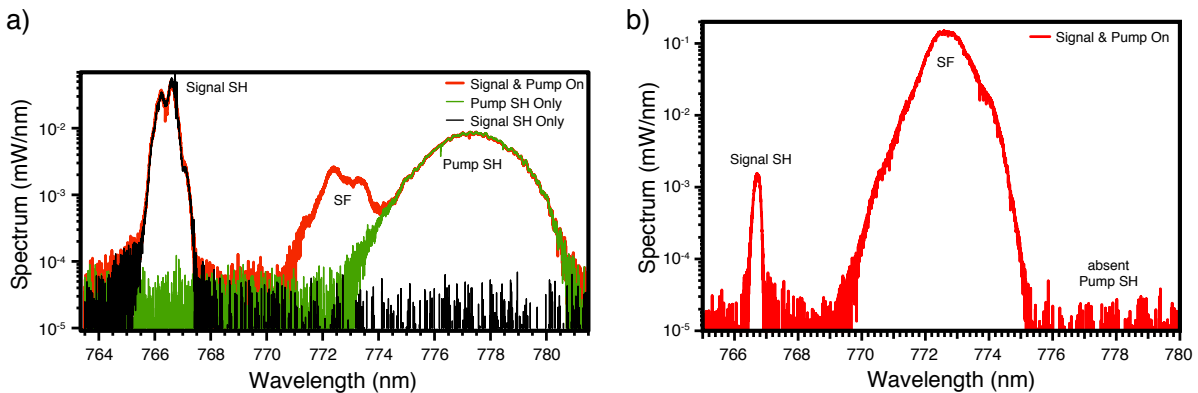

Figure 1: Comparison of spectra between a a) conventional and b) Y-junction implementation of a guided-wave parametric temporal imaging system. The absent pump SH, decreased signal SH, and increased SF can be seen in b).

In the first generation of devices for this application, we used a direct implementation of the linearly chirped A-PPLN waveguide device. These devices lead to a low signal-to-noise ratio (SNR) due to the partial overlap between the SF and SH spectra as seen in Figure 1a. The spectra are inseparable which presents a problem since only the SF component contains useful information. At the time, the required pump and signal wavelengths were too close together to utilize a transfer function solution. As a result, our second generation devices utilized asymmetric Y-junctions [9] as mode multiplexers and demultiplexers to seperate SF and SH spectra. The asymmetric Y-junction created a dramatic improvement as seen in Figure 1b. The signal SH is significantly reduced and the pump SH is absent while the SF level has greatly increased. For our current generation devices, however, the specified pump and signal wavelengths are further apart. As a result, we are able to implement a transfer function solution. We design the bandwidth of the transfer function of the linearly chirped A-PPLN waveguide to only generate the SF components and suppress the SH components thereby bypassing the need for the Y-junction completely. The signal and pump sit at 1550 nm and 1590 nm respectively. Given that the pump and signal spectra have a 12-nm-wide FWHM bandwidth, the bandwidth of the transfer function is designed to be less than 28 nm across. As shown in Figure 2, the pump and signal spectra are drawn in green and the ideal transfer function is drawn in red.
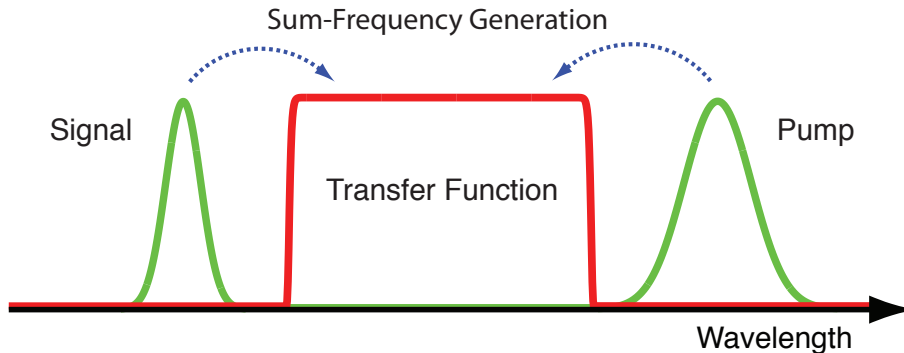

Figure 2: The transfer function (red) is designed to generate the sum-frequency components and suppress the second-harmonic components. The pump and signal spectra are drawn in green.

Due to the abrupt beginning and end of the A-PPLN QPM grating (top hat profile of the nonlinear coefficient), the passband of the transfer function exhibits large undesirable ripples. The hard edges of the top-hat function contain high spatial frequencies in the transform domain and therefore give rise to ripples in the transfer function. These ripples can be minimized by controlling the magnitude of the local nonlinearity. A slow increase/decrease of the nonlinear coefficient at the beginning/end of the device, called apodization, eliminates the high spatial frequencies of the grating edges and therefore greatly reduces the passband ripples. While duty cycle of the QPM grating can be varied along the waveguide length to modulate the nonlinear coefficient, implementing this method is difficult due to the required precise control of the domain lengths during fabrication. The local nonlinearity can also be adjusted by using deleted domain reversal whereby domain reversals are deliberately removed [10]. Domains tend to be sparse at the ends of the waveguide (weak nonlinearity) and gradually become denser towards the center (strong nonlinearity). The third method is nonlinear chirp apodization where a nonlinear chirp is applied at the beginning and end of the device [11]. The wavelengths found in the nonlinear chirp region are far from phase-matched resulting in greatly reduced effective nonlinear coefficient. Wavelengths closer to the linearly chirped region (center of the device) become increasingly phase-matched

2

resulting in an effective nonlinear coefficient that gradually becomes stronger.

Numerically, both the deleted domain reversal and nonlinear chirp apodization methods produce promising results. The ideal transfer function requires minimal ripple size and a steep roll-off as drawn in Figure 2 (red) while maintaining high conversion efficiency. Smaller ripple sizes minimize signal distortions and a steep roll-off prevents SH generation of the pump and signal. The two methods share a trade off between ripple size, roll-off, and conversion efficiency. In Figure 3b, the the transfer function obtained using the deleted domain reversal method exhibits a minimum relative ripple size of about 2% and has a steep roll-off, where the relative ripple size is defined as the ripple magnitude normalized to the magnitude of the transfer function passband. In Figure 3c, the nonlinear chirp apodization exhibits a much improved relative ripple size of about 1.5% but the roll-off is quite gradual. Both apodization techniques, however, are greatly improved over devices having no apodization as shown in Figure 3a. The transfer function's magnitude must be close to zero at the 3 dB point (dotted blue lines) of the pump and signal spectra so that the SH components are suppressed. While the deleted domain reversal method looses some conversion efficiency, the conversion efficiencies for both apodization methods are high enough for practical purposes.
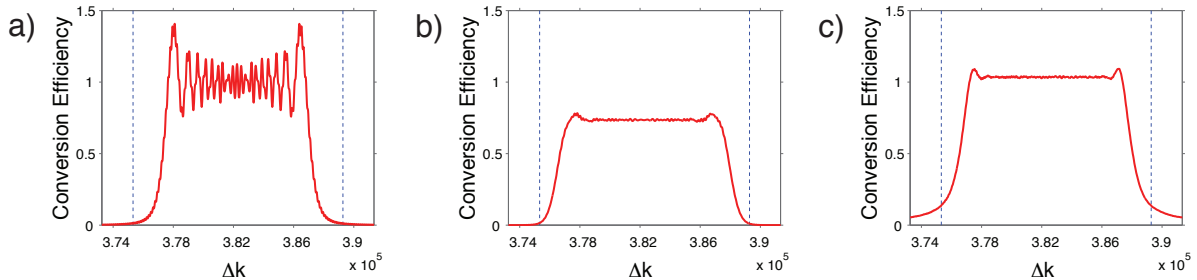

Figure 3: Simulated transfer functions with a) no b) deleted domain reversal c) nonlinear chirp apodization. The dotted blue lines represent the 3 dB points of the signal and pump. The conversion efficiency has been normalized to the mean height of the unapodized transfer function passband.

In the near future, we plan to use a numerical method called simulated annealing (SA) to determine the deleted domain reversal configuration that minimizes the passband ripple while maximizing the conversion efficiency. Similarly, SA will be used to determine the parameters of the nonlinear chirp apodization that maintains sufficiently small ripples but increases the steepness of the transfer function roll-off. Since device robustness to fabrication errors is of great importance, future generation devices will contain deliberate domain width, deleted domain reversal, and waveguide errors to facilitate the study of device tolerances.

In conclusion, a time lens can be used to measure ultrashort temporal optical pulses. We use nonlinear parametric interactions in RPE PPLN waveguides to act as the nonlinear element in such a system. The design of the transfer function of our current generation devices generate the SF components while suppressing the generation of the pump and signal SH components. Ultimately, the transfer function must have minimal passband ripple and steep roll-off. We achieve these requirements by using deleted domain reversal and nonlinear chirp apodization techniques. Both apodization methods show promise for fabricating practical devices.

References

[1] R. L. Fork, C. H. Brito Cruz, P. C. Becker, and C. V. Shank, Compression of optical pulses to six femtoseconds by using cubic phase compensation, Opt. Lett., vol. 12, pp. 483485, 1987.

[2] A. Baltuska, Z.Wei, M. S. Pshenichnikov, and D. A.Wiersma, Optical pulse compression to 5 fs at a 1-MHz repetition rate, Opt. Lett., vol. 22, pp. 102104, 1997.

[3] J.-C. Diels and W. Rudolph, *Ultrashort Laser Pulse Phenomena.* New York, NY: Academic, 1996.

[4] S. A. Akhmanov, A. P. Sukhorukov, and A. S. Chirkin, "Nonstationary phenomena and space-time analogy in nonlinear optics," Zhurnal Eksperimental'noi i Teoreticheskoi Fiziki 55(4), 1430 - 48 (1968).

[5] W. J. Caputi, "Stretch: a time-transformation technique," IEEE Transactions on Aerospace and Electronic Systems AES/7(2), 269 - 78 (1971).

[6] B. H. Kolner, "Space-time duality and the theory of temporal imaging," IEEE Journal of Quantum Electronics 30(8), 1951 - 63 (1994).

[7] C. V. Bennett and B. H. Kolner, "Upconversion time microscope demonstrating 103x magnification of femtosecond waveforms," Optics Letters 24(11), 783 - 5(1999).

[8] C. V. Bennett and B. H. Kolner, "Principles of parametric temporal imaging. I. System configurations," IEEE Journal of Quantum Electronics 36(4), 430 - 7 (2000).

[9] J. R. Kurz, J. Huang, X. Xie, T. Saida, and M. M. Fejer, "Mode Multiplexing in Optical Frequency Mixers," Optics Letters 29(6), 551 - 553 (2004).

[10] J. Huang, X. P. Xie, C. Langrock, R. V. Roussev, D. S. Hum, and M. M. Fejer, "Amplitude modulation and apodization of quasi-phase-matched interactions", Optics Letters, No. 5, Vol. 31, pp. 604 - 606 (March 2006).

[11] M. Charbonneau-Lefort, Ph.D. thesis, Stanford University (2007).

Fluorescence excitation transfer studies of initial stage of phase transition.

Alexei A. Goun, David B. Spry, Michael D. Fayer;

Stanford Univ , 382 Via Pueblo Mal, Stanford, CA 94305., USA.

agoun@stanford.edu

Abstract: We have demonstrated the application of the FRET technique for studies of the phase transition kinetics. Using the combination of the temperature jump and FRET techniques we have measured the time scale of the phase separation.

In spite the progress in the steady state studies, the dynamic behavior of the phase transition are much more demanding from the experimental point of view and challenging to understand theoretically [1,2]. Among experimental difficulties are the triggered initiation of the phase transition and the detection of the spatial structure formed afterwards. In order to overcome those difficulties we have chosen to study the dynamics of the binary fluid demixing, which serves as the model of the three dimensional Ising model with conserved order parameter. By choosing water/2,6-lutidine mixture with a lower critical point at 34ºC, we can triggered the phase separation with a temperature jump. The schematic phase diagram of such a mixture is shown on Figure 1a [3,4].

Composition

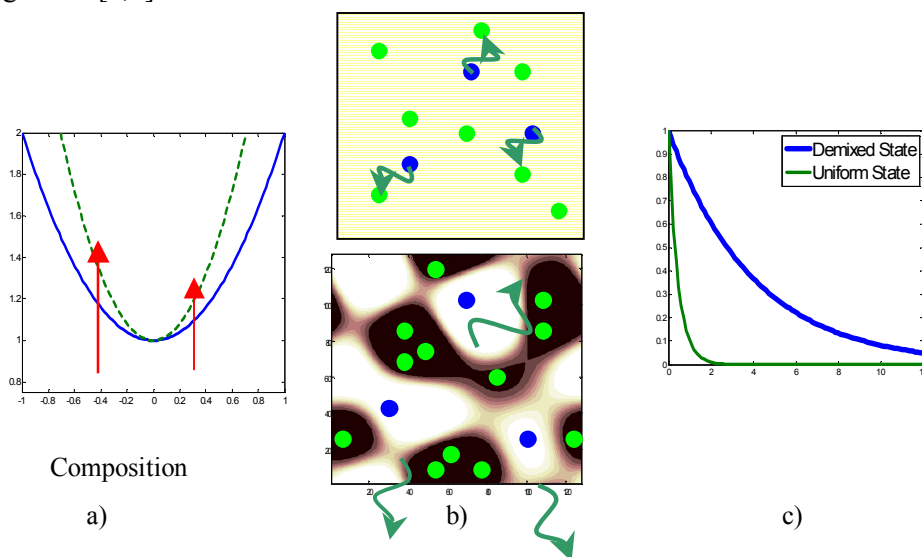a)   b)   c)

Figure 1. a) Phase diagram of the mixture. b)Excitation transport in uniform state (top), its absence in the phase separated state (bottom) c)Fluorescence decay in the uniform and phase separated states.

To address another challenge, the detection of the phase separated state, we applied the technique of the fluorescent excitation transfer. A pair of fluorescence molecules with different solubility in components of the mixture was found. Laser dye Coumarine 480 has a preference for the non-polar component of the mixture – 2,6-lutidine, it serves as a donor of excitation. Hydroxyperene (HPTS) has a preference for a polar component – water, it serves as the acceptor

of the excitation. Both, the donor and acceptor are soluble in the uniform phase of the mixture. The donor fluorescence is strongly quenched in the uniform phase of the mixture. After temperature jump the binary mixture undergoes phase separation. Due to different solubility of donor and acceptor in components of the binary mixture there is spatial separation of the donor and acceptor molecules that results result in the reduction of the efficiency of the excitation transport. The increase in the efficiency of the donor fluorescence will characterize the extent of the phase separation. The phase separation of the mixture and induced drift of donor and acceptor molecules are shown on the Figure 1b. Figure 1c shows the fluorescence decay of the donor in the uniform and non-uniform states (below and above the phase separation temperature).

Temperature jump – excitation transfer approach would allows us to investigate the initial step of the phase separation. The dependence of the rate of phase separation on the magnitude of the temperature jump is shown on Figure 2.
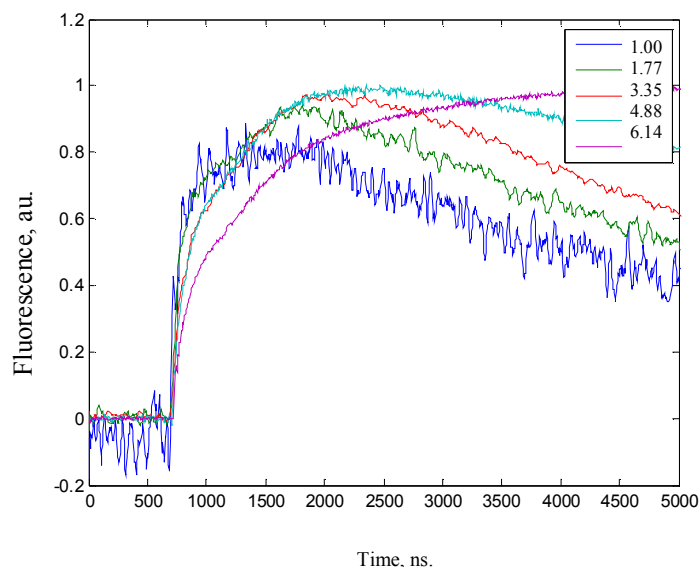

Time, ns.

Figure 2. Kinetics of the phase separation for different magnitudes of the temperature jump pulse energies (in microjoules).

Previously employed techniques relied on the detection of the non-uniform state by light scattering or direct imaging; consequently the spatial resolution was limited by the wavelength of light.

Techniques based on excitation energy transfer can also be used in the situation where direct imaging techniques do not posses sufficient sensitivity such as phase transitions in a confined systems, or in the presence of disorder.[5,6]

References:

[1] D.W. Oxtoby, "Nucleation of First-Order Phase Transitions," Acc. Chem. Res., **31**, 91-97 (1998)
[2] J.D.Gunton, M. San Miguel, Paramdeep S. Sahni, "The Dynamics of First-order Phase Transitions," Phase Transitions, **8**, 266-475
[3] Y.C. Chou, Walter I. Goldburg, "Phase separation and coalescence in critically quenched isobutyric-acid—water and 2,6-lutidine—water mixtures", Phys. Rev. A., **20**, 2105-2113 (1979)
[4] Erdogan Gulari, et. al. "Light Scattering and Shear Viscosity Studies of the Binary System 2,6-Lutidine-Water in the Critical Region", J. Chem. Phys. **56**, 6169 (1972)

[5]S.B. Dierker, P. Wiltzius, "Random-Field Transition of a Binary Liquid in a Porous Medium," Phys. Rev. Lett. **58**, 1865-1868, (1987)

[6] M.Y. Lin, et. al. "Study of Phase Separation of a Binary Fluid Mixture in Confined Geometry," Phys. Rev. Lett., **72**, 2207-2210, (1994)

FABRICATION OF TRANSPARENT CERAMICS FOR OPTICAL APPLICATIONS

G. Deschamps, R. Gaume, Y. He, R.L. Byer

Ginzton Laboratory, Stanford University & GLAM, Stanford University

Transparent ceramics offer interesting potentials for high power laser and highly efficient scintillator applications. In addition to their superior mechanical strength over single-crystals, ceramics present several advantages regarding their fabrication such as reduced fabrication temperatures and processing times as well as the possibility to fabricate larger parts. Although the fabrication and engineering of transparent ceramics have been investigated for more than two decades, the achievement of high optical quality remains a challenging task. In this presentation, we focus on our current progress in optimizing the fabrication process of rare-earth (Nd,Gd,Tm) doped YAG ($Y_3Al_5O_{12}$) transparent ceramics (Fig 1).
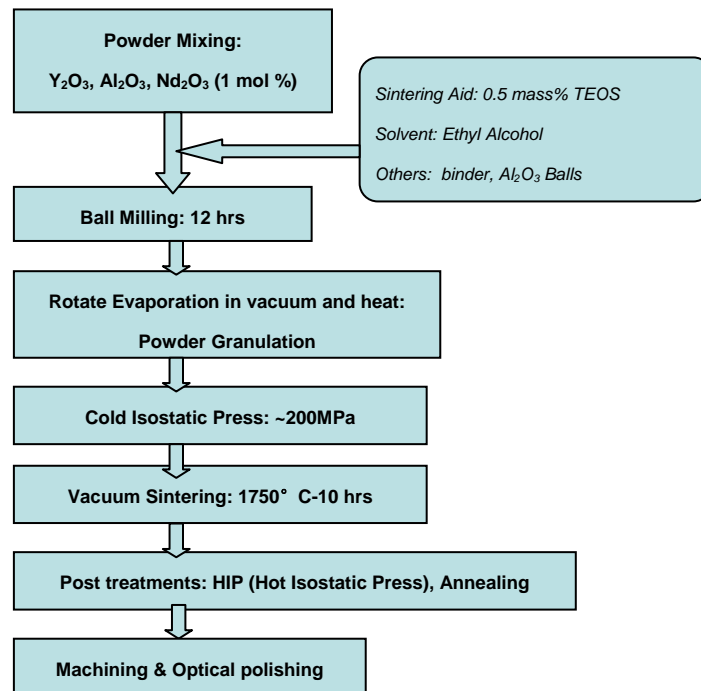

Fig.1. Fabrication process of transparent polycrystalline Nd:YAG.

We have identified several key steps in the fabrication of transparent polycrystalline garnets. One of them is the adjustment of the starting composition to the exact stoichiometric ratio. Any departure from the stoichiometric composition results in the presence of secondary phases and porosity which act as scattering centers and strongly impact the optical transmittance of the final ceramics. The starting nanopowders have large surface areas and therefore absorb moisture while exposed to air. Therefore, it is difficult to precisely determine the exact amount of oxides in the starting powders. To solve this problem, samples with various

relative compositions of yttria and alumina, near stoichiometry, have been prepared and densified under the same sintering conditions. Optical characterizations, including absorption and fluorescence spectroscopies as well as gain measurements, have been performed on the produced samples. The evolution of the attenuation coefficient at 633 nm and the variation of grain size due to stoichiometry shift are presented in Fig.2.
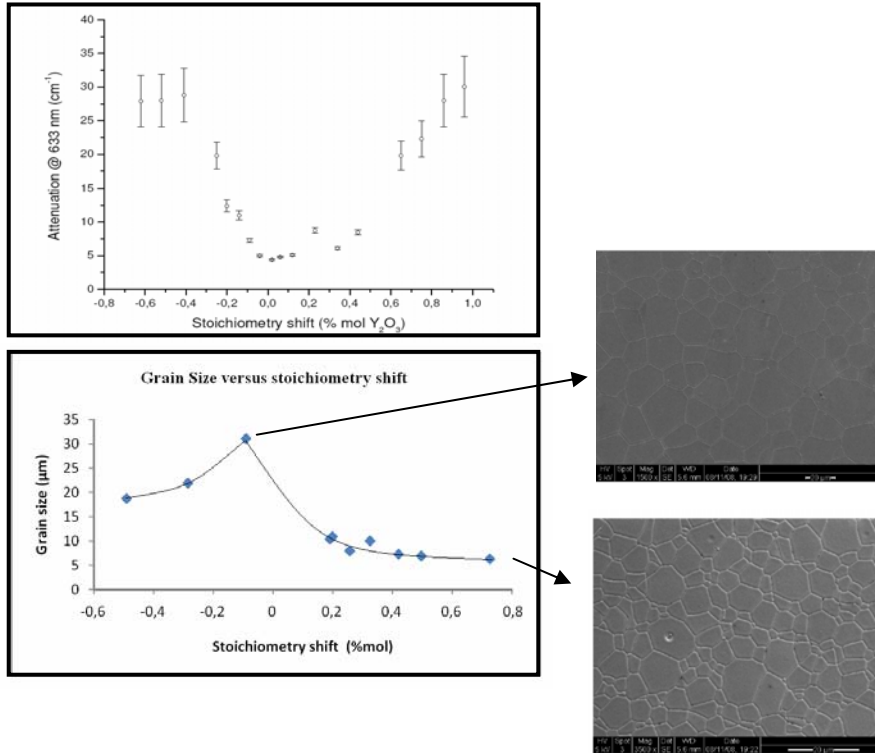

Fig.2. (Top) In-line optical attenuation at 633 nm in pure YAG ceramic samples as a function of composition near stoichiometry; (Bottom) Grain size of Nd:YAG as a function of departure from stoichiometry (positive value correspond to an excess of alumina).

Fig.4 Pellets of Nd:YAG (left pink samples) and Gd:YAG(right yellow samples) on the sunlight.

We succeeded in improving the optical quality of Nd:YAG and Gd:YAG ceramics (Fig.4) by fine tuning the composition and the sintering conditions. More work is however required to further reduce the optical loss in our materials. We are currently investigating various ways to improve the quality of the starting powders, to increase the green body densities through the use of binders and to optimize both sintering and post-heat treatment conditions.

References:

- A. Ikesue and K. Yoshida, ''Influence of Pore Volume on Laser Performance of Nd:YAG Ceramics'', *Journal of material sciences*, 1999, **34**, 1189.

- DE With G, Van Dijk H J A. "Translucent Y3Al5O12 Ceramics", *Material Research Bulletin*, , **19,** 1669-1674 (1984)

- A Ikesue, T Kinoshita, K Kamata, K Yoshida, *Journal of the American Ceramic Society*, "Fabrication and optical properties of high-performance polycrystalline Nd:YAG ceramics for solid-state lasers", **78**[4], 1033-40 (1995)

- A. Ikesue and Y. L. Aung, *Journal of American Ceramic Society*, ''Synthesis and Performance of Advanced Ceramic Lasers,'' **89**[6], 1936–1944 (2006)

- Jeffrey Alan Wisdom's thesis, « Design, characterization and fabrication of neodymium doping profiles in transparent YAG ceramics ", Stanford University, March 2008.

LARGE-AREA HIGH-REFLECTIVITY BROADBAND MONOLITHIC SILICON PHOTONIC CRYSTAL MIRROR MEMS SCANNER

Il Woong Jung, Shrestha Basu-Mallick and Olav Solgaard
Dept. of Electrical Engineering, Stanford University

We have previously reported on a MEMS scanner with a broad-band high reflectivity photonic crystal mirror [1]. These mirrors achieve high reflectivity without the need for multi-layer dielectric stacks which complicated processing and are tolerant to higher temperatures compared to metals. These PC mirrors were fabricated using poly-silicon and low-index oxide on a SOI (silicon-on-insulator) device layer. Recently, S. Hadzialic *et al* have demonstrated a method of fabricating photonic crystal mirrors in monolithic silicon [2]. The monolithic photonic crystals have minimal stressed induced curvature which makes them ideal as large mirrors in scanners or other free-space beam applications. The process is resistant to high temperature and wet chemical etching, making it highly compatible with MEMS processing. In this report, we demonstrate this by introducing a fabrication process in which we integrate the monolithic photonic crystal with a MEMS scanner (Fig 1(a)). The device cross-section is illustrated in Fig 1(b).
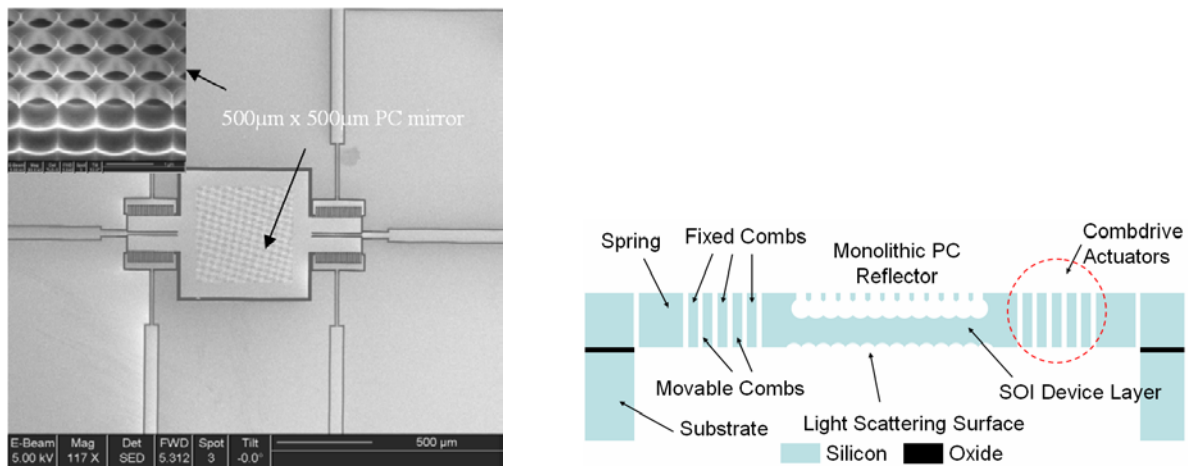

Figure 1: (a) SEM image of the photonic crystal MEMS scanner (insert: SEM image with a 52 degree off-normal angled view of the monolithic photonic crystal) (b) Cross-sectional diagram of the photonic crystal MEMS scanner

The fabrication of the device starts with a 460nm thermal oxidation of a SOI wafer as a hard etch mask with a 25μm silicon device layer and 1.0μm of BOX (buried oxide). The photonic crystals are patterned using a 5x reduction ASM-L i-line stepper at the Stanford Nanofabrication Facility. The pattern is transferred to the oxide and silicon using anisotropic RIE (Reactive Ion Etching) processes (Fig. 2a). A second thin oxidation

is done to protect the sidewalls from Si etchants (Fig. 2b) and the oxide layer on the bottom of the holes is removed by RIE (Fig. 2c). A second Si RIE is done to make a deeper hole used later for isotropic etching of Si to undercut the PC slab (Fig. 2d). Next, the scanner structure is patterned using a contact aligner. The misalignment between the PC patterns (stepper) and scanner patterns (contact aligner) is less than 10μm which results in, at most, 4% reduction in center mirror area. The oxide is etched using RIE and the SOI device layer is etched using the Bosch process (Fig. 2e-2). A third thin oxidation step is done to protect the combdrives and other device structures (Fig. 2f-2). Again, oxide on the bottom of the holes is removed by RIE. The wafer is bonded with resist to a handle wafer and the backside is patterned with 7.0μm resist. The substrate trench is etched using the Bosch process and the BOX thinned down by RIE (Fig. 2g-2). After dicing, the PCs are undercut to create a low-index layer by etching in an isotropic SF$_6$ plasma etch (Fig. 2h-1). Then the PCs are released by vapor HF etching which also removes the oxide on the MEMS structures (Fig. 2i). Finally, the backside of the mirror is patterned by a FIB (focused-ion-beam) to remove reflections at the interface.
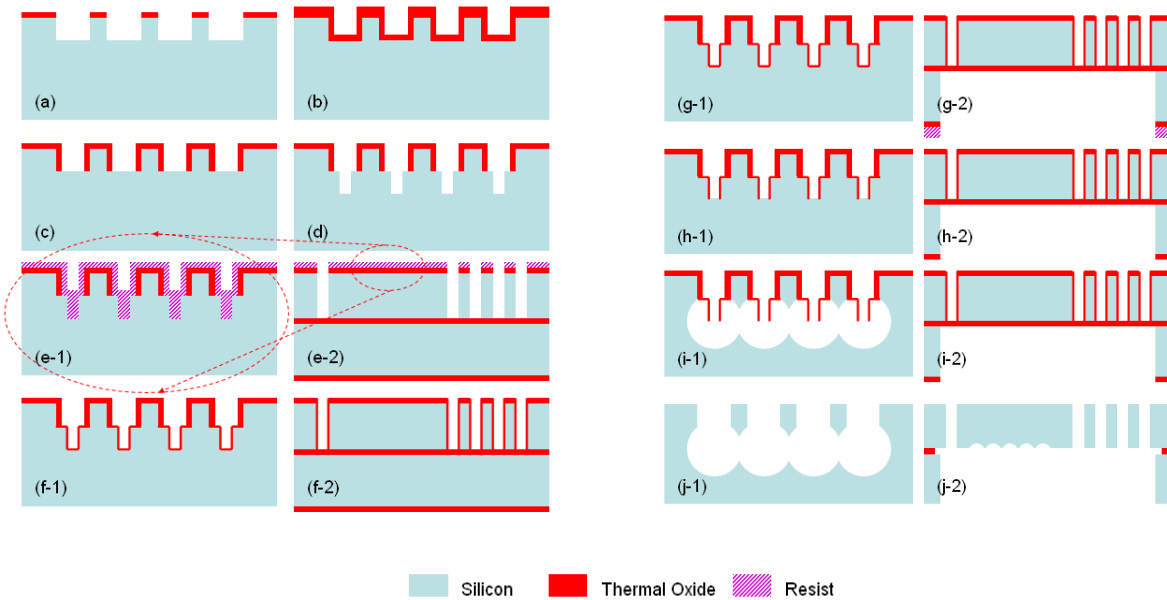
(a)   (b)   (g-1)   (g-2)
(c)   (d)   (h-1)   (h-2)
(e-1)   (e-2)   (i-1)   (i-2)
(f-1)   (f-2)   (j-1)   (j-2)

Silicon   Thermal Oxide   Resist

Figure 2: Fabrication process of the photonic crystal MEMS scanner

The measured surface profile of the monolithic silicon photonic crystal mirror shows the average peak-to-valley roughness to be ~14nm, a flatness of λ/100 in the 1550nm band. This is a significant improvement in flatness compared to the scanner with a poly-Si/oxide photonic crystal mirror which had a peak-to-valley of ~460nm over the same area. Fig. 3 shows the reflection spectrum of the photonic crystal mirror. A broad-band reflectance of >90% is shown in the telecommunications band region of 1520nm to 1620nm. The measurement data show close correlation with simulation results for the given parameters. The scanner

actuation measurements show a scan range of 22 degrees with an input square wave of 67V and resonance frequency of 2.13kHz. Angular dependence measurements of the mirror show that they have low angular dependence with respect to the azimuthal and polarization, showing less than 10% reduction in reflectivity over a 10 degree range. This corresponds well with theoretical studies that show slab photonic crystal mirrors have low angular dependence [3].
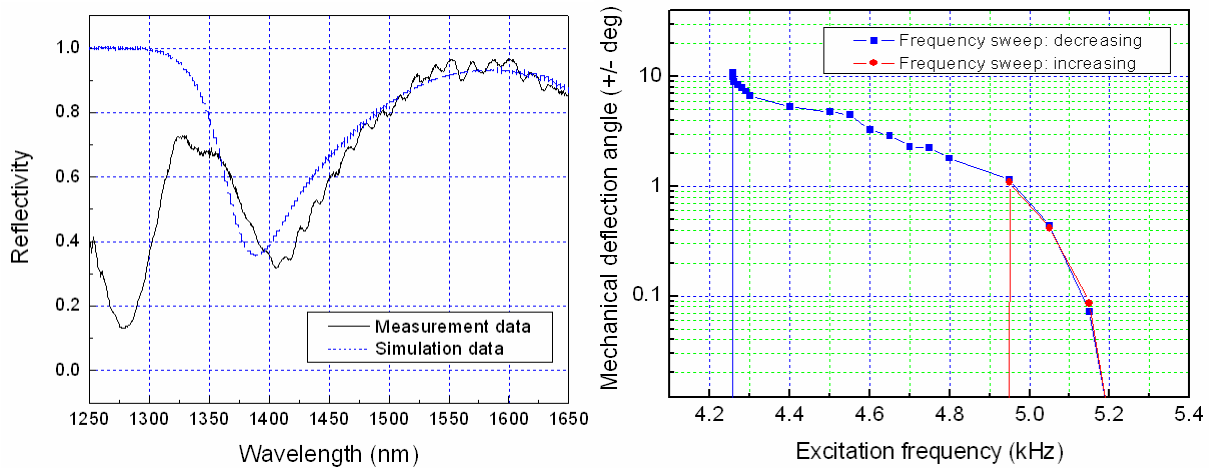

Figure 3: (a) Reflection spectrum of the monolithic silicon photonic crystal mirror (b) Dynamic deflection measurement of the mirror shows a resonance frequency of ~2.1kHz and scan range of 22 degrees

In conlcusion, we have introduced a high reflectivity broadband photonic crystal mirror MEMS scanner with improved mirror quality and performance. These PC mirrors have many adavantages over metals and dielectric stacks in terms of material properties and process compatibility with CMOS and MEMS fabrication. The MEMS scanner has a resonance frequency of 2.1kHz and a scan range of 22 degrees at resonance.

References

[1] I. W. Jung et al, "High Reflectivity Broadband Photonic Crystal Mirror MEMS Scanner," Transducers '07, Lyon, France, June 2007, pp.1513-1516
[2] S. Hadzialic et al, "Monolithic Photonic Crystals," IEEE/ LEOS Conference, Orlando, Florida, Oct 2007, pp. 341-342.
[3] V. Lousse et al, "Angular and Polarization Properties of a Photonic Crystal Slab Mirror," Optics Express, Vol. 12, Issue 8, April 2007, pp. 1575-1582.

DYNAMICS OF SYNCHRONOUSLY PUMPED OPTICAL PARAMETRIC OSCILLATORS INDUCED BY SELF-PHASE MODULATION

Jason Pelc[*], Joseph Schaar[*], and Martin Fejer
E. L. Ginzton Laboratory, Stanford University

Synchronously pumped optical parametric oscillators (SPOPOs) have become widely used sources of tunable coherent visible and infrared radiation. Due to the large peak intensities of the mode-locked pump pulse trains, the oscillation threshold for SPOPOs can be reached for lower pump average powers than in cw or nanosecond OPOs. However, the intense fields can increase the effects of higher-order nonlinearities such as self- and cross-phase modulation. In this work, we investigate the effects of self- and cross-phase modulation on the temporal behavior of a SPOPO, finding that the generated signal power can fluctuate with a characteristic frequency dependent on the pump power, cavity-length detuning, and cavity losses. Numerical simulations show that these oscillations are due to a self-phase modulation- (SPM-) induced nonuniform phase profile across the pulse that builds up over many round trips of the resonant pulse through the optical cavity. There is a periodic pulse reshaping by the interaction of the parametric gain with this phase profile, as well as with the cavity-length detuning and group-velocity mismatch of the interacting waves. The oscillations are studied experimentally and numerically and a heuristic model is proposed to explain the effect.

The interaction of $\chi^{(3)}$ effects with parametric gain has been studied theoretically due to interest in the possibility of stable soliton propagation in which the intrinsic losses of the propagation medium are counteracted by parametric gain. In one study, a variational formulation of the pulse propagation allows a detailed analysis of the pulse properties and stability as a function of the parametric gain and loss [1]. The authors find that under suitable initial conditions, the signal pulse amplitude will experience small amplitude oscillations due to a nonuniform SPM-induced phase profile across the pulse. Such oscillations have been
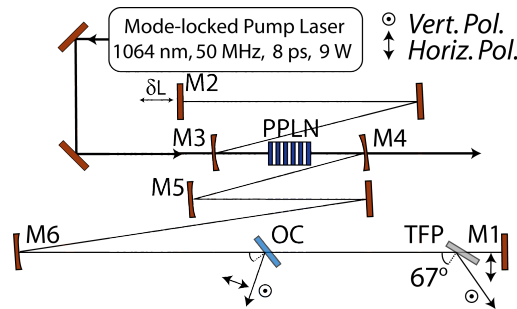

Fig. 1: SPOPO layout. OC = output coupler, TFP = thin film polarizer, PPLN = periodically poled lithium niobate.

---

observed numerically in femtosecond SPOPOs but were not investigated in detail [2]. In one study, it was shown that the interplay of dispersion, parametric gain, and the nonlinear phase modulation caused asymmetric spectral broadening of the signal wave, but again instabilities or oscillatory behavior in SPOPOs were not studied [3].

The oscillatory behavior was originally observed in a low-loss doubly resonant SPOPO designed for the intracavity generation of THz radiation. However, we chose to analyze the behavior using a simpler singly resonant SPOPO, a schematic of which is shown in Fig. 1, to be pumped at 1064 nm and designed to resonate a signal wave tunable within a few THz of the degeneracy wavelength 2128 nm. A *pico*TRAIN mode locked Nd:YVO₄ laser was used as the pump laser, and emitted Gaussian pulses of 8-ps $1/e^2$ intensity width with a repetition rate of 50 MHz. The optical resonator was designed with no deliberate outcoupling, and had residual round trip losses of 3.4% due to imperfect mirror and crystal coatings and an intracavity polarizer. A CaF₂ window near Brewster's angle was used as a variable outcoupler. Threshold was reached for a pump average power of 1.5 W, which agrees well with numerical simulations that predict a threshold of 0.95 W. For several pump powers and outcoupling values, the intracavity signal power was measured as a function of time and cavity-length, and the frequency domain behavior was observed using an rf spectrum analyzer.

In addition to the experimental studies, we employed a numerical technique based on the split-step pseudospectral method to simulate the SPOPO behavior, similar to the technique used in [3]. The simulations treat the interacting fields as spatial plane waves and simulate only the temporal dynamics of the SPOPO. However, an important improvement over previous simulations is the correction of the nonlinear coupling coefficients to account for the different beam sizes using a near-field Gaussian approximation [4].

A plot of the intracavity resonating power versus cavity-length detuning, δL, is shown in Fig. 2a. As the pump power is increased further above threshold, the SPOPO supports operation over a wider range of detunings, but the instability regimes in which oscillatory behavior is observed are denoted with brackets. In Fig. 2b we see a simulated plot of the oscillations in intracavity signal power for a case in which $\delta L > 0$. These oscillations can be understood by looking at the parametric plot in Fig. 2c. As the stored power increases, the pulse centroid position (relative to the pump arrival time, illustrated in the inset) decreases towards 0. This occurs because the pump pulse, and therefore the parametric gain, is localized near $t = 0$. A large intensity then builds up and the pulse develops a nonuniform phase profile due to SPM. Because the parametric gain is phase sensitive, the phase distortion of the signal prevents the further buildup of signal intensity. The cavity detuning then delays the pulse relative to the pump, causing a shift in the centroid. Once enough of the phase-distorted pulse has been removed from the interaction region near $t = 0$, the pulse wings decay due to cavity losses and the signal regrows near $t = 0$, completing a cycle.
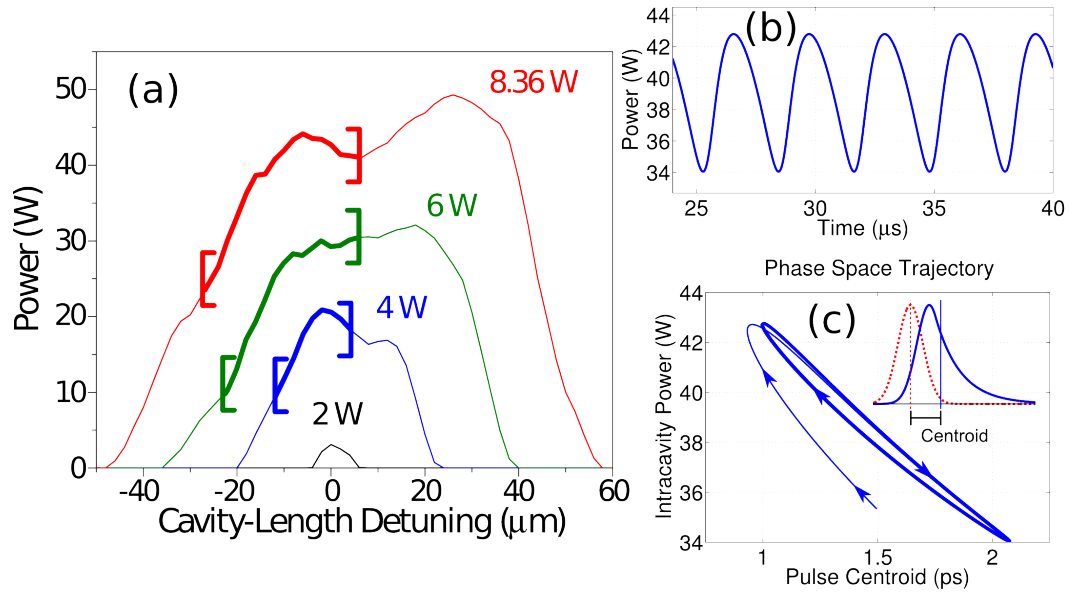
Fig 2: (a) Intracavity signal power versus δL for several pump powers. The brackets mark the boundaries of the oscillatory behavior, (b) oscillations in signal power versus time calculated using the split-step pseudospectral method for a case in which $\delta L > 0$, and (c) a parametric plot of intracavity signal power and signal pulse centroid position (relative to pump).

We are also exploring the dependence of the oscillation frequency on several experimental parameters including pump power, δL, and cavity loss. We have developed a model based on periodic pulse reshaping and are currently studying its regimes of applicability to allow us to better predict when the undesirable oscillatory behavior occurs, and therefore how to design SPOPO systems that avoid these dynamics. However, we anticipate that these oscillations will be observed in low-loss SPOPO systems with an intracavity Kerr medium, particularly those designed for the storage and utilization of intense intracavity pulses, such as for THz generation by difference-frequency mixing.

References

1. S. Longhi, G. Steinmeyer, and W. S. Wong, "Variational approach to pulse propagation in parametrically amplified optical systems," *J. Opt. Soc. Am. B* **14**, 2167 (1997).

2. J. Seres and J. Hebling, "Nonstationary theory of synchronously pumped optical parametric oscillators," *J. Opt. Soc. Am. B* **17**, 741 (2000).

3. E. Gaizauskas, R. Grigonis, and V. Sirutkaitis, "Self- and cross-modulation effects in a synchronously pumped optical parametric oscillator," *J. Opt. Soc. Am. B* **19**, 2957 (2002).

4. R. L. Byer, "Optical Parametric Oscillators," in *Quantum Electronics, A Treatise* **1**, ed. H. Rabin and C. L. Tang (Academic Press, 1975).

Self-phase-locked degenerate synchronously pumped optical parametric oscillator

Samuel Wong, Tomas Plettner, Konstantin Vodopyanov, and Robert Byer
Ginzton Laboratory, Stanford University

Phase-stable frequency combs have been instrumental in advancing state-of-the-art metrology and high-precision measurements. Extending the combs toward shorter wavelengths in the UV and X-ray regime has pushed ultrafast science to the attosecond level and revolutionized atomic physics. While there has not been much development on comb extension toward longer wavelengths, it is important for applications that require critical optical phase control in the mid to far-IR regime, such as vacuum-based laser-driven particle acceleration. Furthermore, the synthesis of phase-locked longer-wavelength combs would establish absolute optical frequency standards in the IR and enable high-resolution spectroscopy at wavelengths unavailable to solid-state lasers.

To realize frequency combs in the mid-IR, we decided to exploit second-order nonlinear processes for down-conversion to longer wavelengths. Additionally, we could take advantage of the fixed phase relationship between pump, signal, and idler in optical parametric oscillation (OPO), i.e., $\phi_p = \phi_s + \phi_i - \pi/2$. We predicted that a mode-locked OPO operating at frequency degeneracy would exhibit phase-locking because the signal and idler combs experience mutual or self-injection locking.

Phase coherence between the pump and output waves in a CW OPO is automatically accomplished at frequency degeneracy because the signal and idler are indistinguishable since their phase difference is trivially zero [1]. The locking analysis for a synchronously-pumped OPO (SPOPO), however, needs to account for the multi-axial-mode structure of frequency combs, represented as $f_n = nf_{rep} + \delta$, where n is the mode number, f_{rep} is the mode spacing, and δ is the carrier-envelope offset (CEO) frequency. The synchronous-pumping condition stipulates that f_{rep} is equivalent for the pump, signal, and idler combs. Hence, both $n_p = n_s + n_i$ and $\delta_p = \delta_s + \delta_i$ need to be satisfied. The SPOPO is considered phase-locked when the difference between the signal and idler CEO frequencies is a multiple of the mode spacing because the corresponding temporal carrier-envelope phase slips are identical provided that the carrier frequencies remain equal. The locking condition for the CEO frequencies is

$$2\delta_{s,i} - \delta_p = mf_{rep} \ \rightarrow \ 2\delta_{s,i} - \delta_p = 0. \tag{1}$$

When the SPOPO is degenerate, the signal/idler CEO frequency is one-half that of the pump. If the degenerate signal and idler combs are shifted by half a mode spacing in opposite directions, the SPOPO remains in the phase-locked (degenerate) regime; hence, there are two distinct offset eigenstates separated by $0.5f_{rep}$. According to Eq. (1), however, this distinction disappears after doubling the SPOPO comb to compare with the pump comb for confirming phase coherence.

The nonlinear gain element used for the SPOPO was a 1-mm-long MgO-doped periodically-poled lithium niobate (PPMgO:LN) crystal, which was non-critically phase-matched for 1550 nm at 140 °C. The nonlinear crystal was placed inside a near-symmetrically folded confocal cavity. A titanium-sapphire mode-locked laser (180-fs pulses at 80 MHz) was employed as the pump at 775 nm. A 50% output coupler was used and a 6-mm long AR-coated plate of fused silica was inserted inside the SPOPO cavity to compensate group velocity dispersion (GVD) at 1550 nm. The SPOPO cavity length was controlled coarsely with a motorized translation stage and finely with a piezoelectric transducer (PZT).

The degenerate SPOPO pump threshold was measured to be 140 mW. A maximum output power of 250 mW when pumped at 900 mW was observed. The spatially averaged pump depletion reached 60%. The slope efficiency with respect to incident pump power was 32%. The FWHM spectral bandwidth at degeneracy was 200 cm^{-1} or 50 nm centered around 1550 nm. Because the initial pump bandwidth was 75 cm^{-1}, there was output comb broadening factor of about three. The duration of the degenerate output pulses was 70 fs and thus transform-limited for Gaussian profiles.
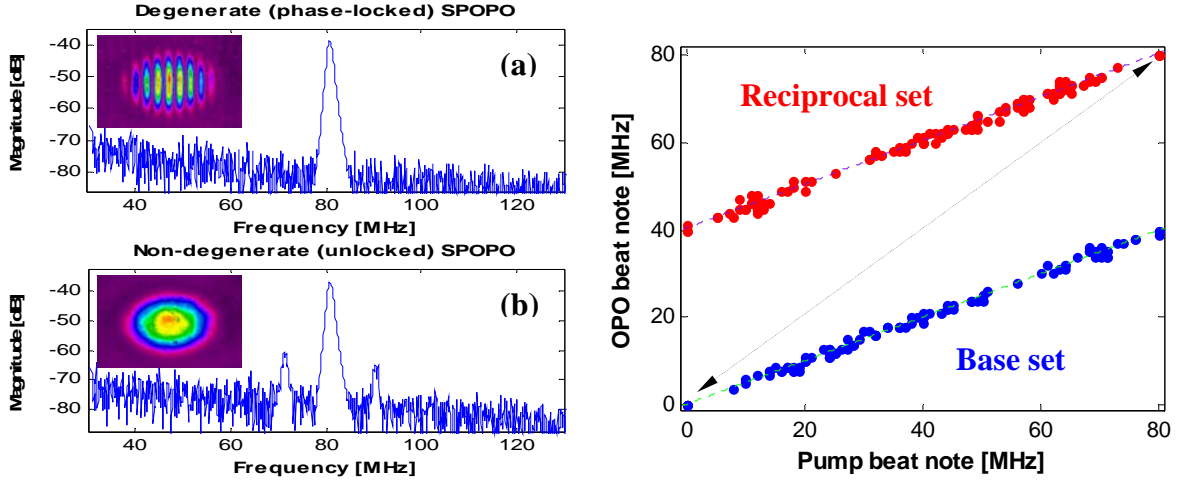
Fig. 1. Measurements obtained from frequency-doubling the SPOPO output and interfering with the pump for (a) degenerate and (b) non-degenerate operation. The scatter plot on the right shows that the slope of the degenerate SPOPO vs. pump beat notes is one-half, as required for phase-locking. The base and reciprocal sets are redundant data points symmetrical around half the repetition rate.

While the pump wavelength and crystal temperature were kept fixed, a change in the SPOPO cavity length was applied to alter the operating state. Within the degenerate regime, adjusting the roundtrip cavity length by $\lambda_c/2$ (where λ_c is the 1550-nm oscillating wavelength) switched between the offset eigenstates. A substantial length change caused the SPOPO to become non-degenerate (to preserve cavity synchronism) such that distinct signal and idler peaks appeared in the spectrum. The optical spectrum is the primary metric for distinguishing between degenerate and non-degenerate operation.

Phase-coherence of the degenerate SPOPO was confirmed using three techniques. In the first method, the frequency-doubled output was interfered with the pump beam at a low angle to generate a spatial fringe pattern. Observation of stable fringes with high visibility implied phase coherence while blurring denoted random phases. In the second technique, the same interference setup was measured collinearly to analyze the RF spectrum. Observation of only harmonics of the repetition rate indicated phase coherence whereas emergence of satellite beat notes represented unlocked SPOPO operation due to mismatch of CEO frequencies. The third method employed an independent 1550-nm CW laser serving as an external phase reference. The beat notes between the degenerate SPOPO and CW laser and between the pump and frequency-doubled CW laser were compared. The pump laser was allowed to drift across the 80-MHz repetition rate to observe how the CEO frequency of the SPOPO would behave in response. Phase-locking required the SPOPO beat note to be half the pump beat note, in accordance with Eq. (1). Fig. (1) shows the measurements from the three techniques distinguishing between degenerate and non-degenerate operation and confirming phase-locking in the degenerate SPOPO.

No feedback servo loop was needed for the SPOPO to maintain self-injection-locked oscillation. Despite the lack of active stabilization, the phase-locked SPOPO would routinely regain self-phase-locking after application of deliberate small perturbations had stopped. The degenerate SPOPO operated stably for up to an hour when there were minimal environmental noise stimuli.

The frequency locking range can be interpreted as how much cavity length detuning is tolerated while maintaining self-phase-locked operation in the SPOPO. Around each degenerate signal/idler axial mode within the output comb, there exists some feedback mechanism from intrinsic parametric nonlinearity at gain saturation that pulls the signal and idler together, thus rendering this frequency excursion range as an effective potential well. Solving the phase evolution equation from the degenerate nonlinear coupled wave equations, we discover a phase correction effect within the nonlinear crystal that counters perturbations of the cavity length, thus enabling the OPO to continue operating at maximum
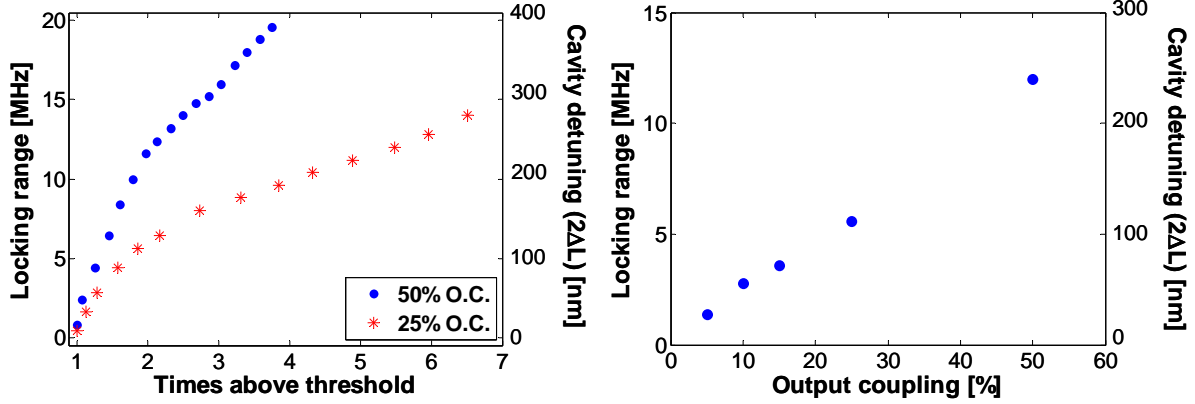
Fig. 2. Measurements of locking range as a function of number of times above pump threshold for different output couplers (left) and as a function of output coupling (right).

gain, which occurs at degeneracy in our case. Making appropriate assumptions, we can derive an approximate analytic expression for the frequency locking range based on operating parameters, given as

$$\Delta f \approx \pi^{-1} \kappa_s E_p L_c f_{rep} \;\; \rightarrow \;\; \Delta f \sim \beta \gamma \sqrt{G} \tag{2}$$

where κ_s is the nonlinear coefficient of the signal, E_p is the electric field of the pump, and L_c is the crystal length. Note that the locking range defined in Eq. (2) can exceed the mode spacing with the proper parameters. This expression can be rewritten where the locking range is proportional to the nonlinear coupling strength β and cavity decay rate γ (cavity loss or inverse cavity Q) and varies with the square root of the parametric gain. Recall that pump electric field is proportional to the square root of the pump intensity and the threshold of the degenerate SPOPO (which determines gain at a given pump power) is proportional to the square of the signal resonating losses. The modified locking range relation follows the functional form of the Adler equation for steady-state injection locking.

The length of the oscillation window versus cavity length detuning for each SPOPO degenerate state (in either offset eigenstate) is effectively a measure of the frequency locking range because the SPOPO ceases to oscillate when the signal and idler modes deviate outside the locking range around degeneracy owing to lack of sufficient gain. Fig. (2) shows the locking range measured as a function of number of times above threshold (i.e., parametric gain) and output coupling (i.e., cavity Q). Both sets of data are consistent with Eq. (2) where the frequency excursion has a square root relation with the gain and a linear relation with the loss.

To our knowledge, this is the first demonstration of a self-stabilizing phase-locked divide-by-2 type I SPOPO operating in the degenerate regime as a novel frequency comb generator [2]. We show that it is well-behaved despite past misperceptions that such OPOs are unstable and impractical. In fact, the frequency locking range can be expanded to exceed a free spectral range such that the SPOPO becomes impervious to any cavity length perturbations. Upgrading the cavity optics and employing better dispersion control could achieve a full octave of output spectrum for the generation of few-cycle pulses. Cascading these broadband degenerate SPOPOs and implementing phase-preserving optical parametric amplification (OPA) stages could synthesize stable high-peak-power frequency combs at mid-IR wavelengths useful for high-precision metrology and spectroscopy.

[1] C. D. Nabors, S. T. Yang, T. Day, and R. L. Byer, "*Coherence properties of a doubly-resonant monolithic optical parametric oscillator,*" J. Opt. Soc. Am. B, **7**, 815-820 (1990)
[2] S. T. Wong, T. Plettner, K. L. Vodopyanov, K. Urbanek, M. Digonnet, and R. L. Byer, "*Self-phase-locked degenerate femtosecond optical parametric oscillator,*" Opt. Lett., **33**, 1896-1898 (2008)